Distribution Agreement

In presenting this thesis or dissertation as a partial fulfillment of the requirements for an advanced degree from Emory University, I hereby grant to Emory University and its agents the non-exclusive license to archive, make accessible, and display my thesis or dissertation in whole or in part in all forms of media, now or hereafter known, including display on the world wide web. I understand that I may select some access restrictions as part of the online submission of this thesis or dissertation. I retain all ownership rights to the copyright of the thesis or dissertation. I also retain the right to use in future works (such as articles or books) all or part of this thesis or dissertation.

Signature:

_____   _____

Gary Lavelle Hunter   Date

Dynamics in Confined Brownian Systems

By

Gary Lavelle Hunter
Doctor of Philosophy

Physics

———————————————————
Eric R. Weeks
Advisor

———————————————————
Sven Behrens
Committee Member

———————————————————
Alberto Fernandez-Nieves
Committee Member

———————————————————
Connie Roth
Committee Member

———————————————————
Kurt Warncke
Committee Member

Accepted:

———————————————————
Lisa A. Tedesco, Ph. D.
Dean of the James T. Laney School of Graduate Studies

————————————
Date

Dynamics in Confined Brownian Systems

By

Gary Lavelle Hunter

B. S., University of West Georgia, 2006

Advisor: Eric Richard Weeks, Ph. D.

An abstract of

A dissertation submitted to the Faculty of the

James T. Laney School of Graduate Studies of Emory University

in partial fulfillment of the requirements for the degree of

Doctor of Philosophy

in Physics

Spring, 2012

Abstract

Dynamics in Confined Brownian Systems

By Gary Lavelle Hunter

We use experiments and simulations to study two phenomena related to the glass transition: the effects of confinement and the phenomenon of cage breaking. Hard sphere colloidal suspensions are used as model glass formers and are visualized using confocal microscopy. Brownian dynamics simulations are used to study a minimalist system of cage breaking hard disks. We also present computational techniques that accurately track the rotational motion of rigid clusters of colloidal particles.

In experiments, we confine colloidal suspensions within emulsion droplets to probe how properties of the external surrounding medium affect internal dynamics. We find dynamics are sensitive to the viscosity of the confining medium and observe a gradient in dynamics as a function of distance from the confining interface. These results are analogous to previous observations in confined polymers and small molecule glass formers, where dynamical properties strongly depend on the interactions present at the confining interface.

Via simulations, we investigate cage breaking in dense hard disk systems using a model of three Brownian disks confined within a circular corral. The exact free energy landscape for this system can be calculated as a function of system size. We find the average time between cage breaking events follows an Arrhenius scaling when the energy barrier is large. We also discuss some of the consequences of using a one-dimensional representation to understand dynamics in a multi-dimensional space, such as diffusion acquiring spatial dependencies and discontinuities in spatial derivatives of free energy.

Finally, we describe a method of tracking the rotational motion of clusters of colloidal particles. Using rigid body transformations to determine the rotations of a cluster, we extend conventional proven particle tracking techniques in a simple way, thus facilitating the study of rotational dynamics in systems containing or composed of colloidal clusters. We test our method by measuring dynamical properties of simulated Brownian clusters under conditions relevant to microscopy experiments. We then use the technique to track and describe the motions of a real colloidal cluster imaged with confocal microscopy.

Dynamics in Confined Brownian Systems

By

Gary Lavelle Hunter

B. S., University of West Georgia, 2006

Advisor: Eric Richard Weeks, Ph. D.

A dissertation submitted to the Faculty of the
James T. Laney School of Graduate Studies of Emory University
in partial fulfillment of the requirements for the degree of
Doctor of Philosophy
in Physics

Spring, 2012

Acknowledgements

me by **my family** when I was young and during my stint as an undergraduate and graduate student. Thanks to you all for telling me to make something of myself and for showing me how to do it. I love you all and I'm *finally out of school!* Last but not least, I thank my many furry roommates, **Abby, Benny, Bonsai, Jojo, Max, Molly,** and **Po**, for being constant sources of cuteness, entertainment, and affection.

For Zoey and the kids.

Citations to previously published work

Portions of chapter 2 appear in:

"The physics of the colloidal glass transition", Gary L. Hunter and Eric R. Weeks, to appear in *Rep. Prog. Phys.*, arXiv:1106.3581

Large portions of chapter 3 appear in:

"Boundaries matter for confined colloidal suspensions", Gary L. Hunter, Kazem V. Edmond, Eric R. Weeks, to be submitted to *Nature Physics*

Large portions of chapter 4 appear in:

"Free-energy landscape for cage breaking of three hard disks", Gary L. Hunter and Eric R. Weeks, *Phys. Rev. E*, **85**, 031504 (2012)

Large portions of chapter 5 appear in:

"Tracking the rotational diffusion of colloidal clusters", Gary L. Hunter, Kazem V. Edmond, Mark T. Elsesser, and Eric R. Weeks, *Optics Express*, **19**, (2011)

Contents

List of figures

List of tables

Chapter 1

Introduction

My graduate studies have focused on answering two questions related to the behavior of systems approaching the glass transition: 1) Do dynamics in confined colloidal suspensions depend on properties at the confining interface? 2) Can one understand dynamics in dense hard-disk systems in terms of free energy landscapes? What follows in this dissertation are my efforts to show that the answer to both of the above questions is "yes". Though seemingly unrelated, these projects illuminate the similarities between different types of glass forming systems – small molecules, polymers, and colloids – and will hopefully further efforts to understand the glass transition as a "universal" phenomenon. The main body of the dissertation will discuss the methods, observations, and conclusions related to each of these projects. Also covered are computational algorithms I developed to accurately track the rotational motion of colloidal clusters, which have since been used to study the decoupling of translational and rotational diffusion in colloidal glasses. Here, I begin with a brief introduction to general topics discussed throughout this dissertation, providing the context for my work along the way. This is followed by a summary of my experimental and simulational results, and an overview to the structure of the dissertation.

1.1 The Glass Transition

Upon cooling or compression, many liquids freeze – that is, the molecules constituting the liquid rearrange to form some type of ordered crystalline structure. However, some liquids can be cooled below their freezing point without crystallizing – in these cases, the liquid is termed *super-cooled.* In general, creating a super-cooled liquid (SCL) requires cooling to be sufficiently rapid that crystals do not have time to nucleate. If rapid cooling of an SCL continues, the material can become a *glass*: the amorphous liquid-like structure is retained, but the microscopic dynamics all but cease. This sudden arrest is the *glass transition*, and the temperature at which it occurs is the glass transition temperature, T_g. As the liquid is cooled toward T_g, its viscosity rises smoothly and rapidly [1, 2], and below T_g the sample's viscosity becomes very high – the material can bear some degree of stress and over most practical experimental time scales can be considered solid [3–9]. Thus, a working definition of a glass might be a material which structurally resembles a dense liquid, but over short time scales behaves mechanically as a solid.

The illustration given in Fig. 1.1 shows the cooling of a system initially in a disordered liquid-like state. Along the top branch of the figure, cooling is slow and allows the components of the liquid sufficient time to nucleate crystals, eventually resulting in crystallization of the entire system. Along the bottom branch however, the rate of cooling is much higher, i.e. the system is thermally quenched. In this scenario, the density of the system increases more quickly than the individual components can order into the thermodynamically preferred crystalline structure, resulting in a dense amorphous or disordered state.

Calling a glassy material a "solid" depends on the time scale one considers [10]. Window glass, a vitreous form of silicon dioxide, is of course the quintessential example
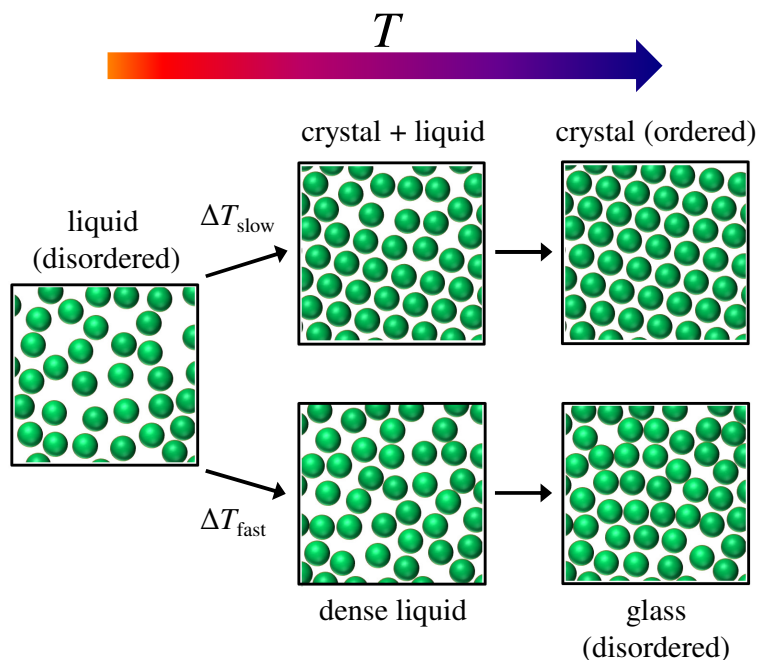
Figure 1.1: Cooling of a glass forming liquid. Top: The rate of cooling is slow and permits the nucleation of crystals. Continued cooling results in crystallization of the system. Bottom: High cooling rate. Here, insufficient time is given for the system to nucleate crystals and upon continued cooling, the system forms a disordered glassy phase.

of a glass. It is sometimes claimed that very old windows are thicker at the bottom due to flow of glass. However, the thickness variations in antique windows are the result of a particular manufacturing method rather than the result of the glass flowing over long times [11, 12]. A more instructive example of glassy behavior and time scales can be seen in pitch, a bituminous tar. Like window glass, pitch is unmistakably solid to the touch – if struck with a hammer, it will shatter. However, for over 80 years a funnel filled with pitch has been dripping at a rate of roughly one drop every 100 months, yielding a very approximate viscosity of 10^{11} times that of water. The so-called "Pitch Drop Experiment" has been housed at the University of Queensland in Brisbane, Australia since 1927 [13].

Glass transitions occur in systems with a variety of compositions: small molecules such as water and SiO_2; short- and long-chain polymers; metal alloys; and suspensions of

colloidal particles. While the details of these systems may be very different, there are qualitative similarities in the behavior of these materials as the glass transition is approached. Independent of composition, a glass former retains an amorphous, liquid-like structure upon cooling into the glassy phase. Relative to its liquid state, the viscosity of a glass former increases dramatically, > 13 orders of magnitude for some materials [14–16].

For this dissertation, the glass forming materials are suspensions of rigid colloidal microspheres. Important differences between these particles and other glass forming systems will be highlighted in Sec. 1.2, and other relevant similarities between colloids and other glass formers will be discussed in Sec. 1.3.

1.2 Hard Sphere Colloids as Model Glass Formers

Perhaps the simplest interaction between two particles is that of *hard spheres* [17]. If r defines the distance between two sphere centers, and σ is the sum of the two sphere radii, the hard sphere potential is given by

$$U(r) = \begin{cases} \infty, & \text{if } r \leq \sigma \\ 0, & \text{otherwise,} \end{cases} \tag{1.1}$$

which is to say that the only restriction placed upon the system is that particles cannot interpenetrate (sometimes described as excluded volume interactions). Hence, all allowable configurations have identically zero potential energy. From a viewpoint of statistical mechanics, this implies that the free energy, $F = -TS$, is governed entirely by entropy to within an additive constant [18, 19], which for monodisperse systems (systems of a single particle size) means that the only control parameter is volume fraction [20–23]. Volume fraction, $\phi = NV_p/V$, is a dimensionless analogue of particle number density, where N is the number of particles in the system, V_p is the single particle volume, and V is the total system volume.
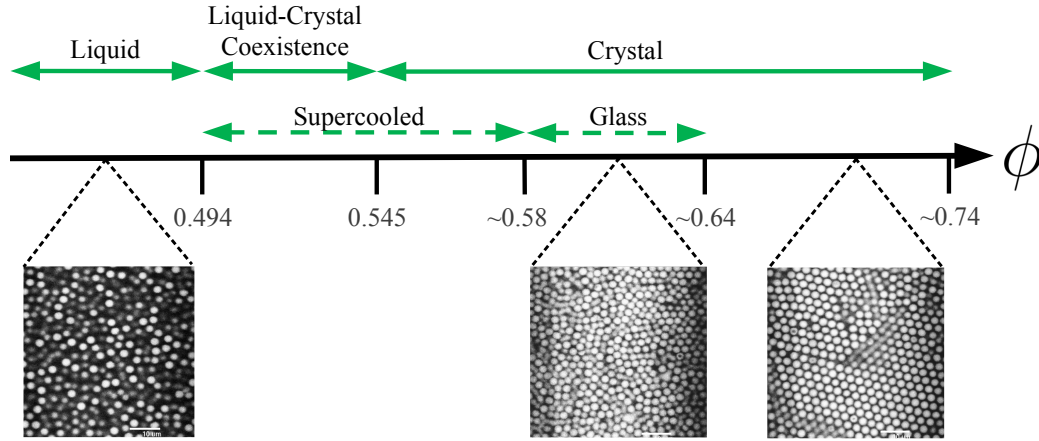
Figure 1.2: Top: phase diagram as a function of volume fraction for monodisperse hard spheres. Solid and dashed arrows indicate equilibrium and non-equilibrium phases, respectively. Bottom: analogous phases in nearly monodisperse (diameter $\approx 2~\mu$m) colloidal systems.

The phase diagram for hard spheres is shown in Fig. 1.2, as a function of ϕ. Below $\phi = 0.494$, the suspension is a liquid. To force the system into a supercooled or glassy state, one must increase ϕ fast enough to avoid crystallization. The supercooled region persists between $0.494 \leq \phi < \phi_g \approx 0.58$, whereas the glassy region lies between $\phi_g < \phi < \phi_{rcp} \approx 0.64$. The existence of the glass for hard spheres requires that the sample be somewhat polydisperse, that is, the spheres must have a distribution of sizes [24–28]. The upper bound of the glassy region is the volume fraction at random close packing, ϕ_{rcp}, the maximum density of a completely random sphere packing [29–31]; the precise value of ϕ_{rcp} depends on the polydispersity [32]. Above ϕ_{rcp}, samples must have domains of crystalline structure, or, preferably from the thermodynamic point of view, the sample may be entirely crystallized. Density can be further increased up to the limit of hexagonal close packing,

$\phi_{hcp} = \dfrac{\pi}{3\sqrt{2}} \approx 0.74$.

In many cases, colloidal particles can be considered to be simple hard spheres [33–36]. By the late 1960's and early 1970's, experimental evidence was demonstrating that

the structures in colloidal suspensions can be analogous to those in atomic systems [37–39], leading to the extensive use of colloids over the next decade as model liquids and crystals [1, 33, 40–46]. In 1982, Lindsay and Chaikin mixed together two different sizes of charged colloidal particles, and observed a glassy phase (amorphous structure, finite rigidity) [10] in agreement with subsequent simulations [47]. Later in 1986-87, experiments performed by Pusey and van Megen demonstrated a hard sphere colloidal glass transition in a concentrated sample of uncharged colloids [33, 34, 48].

It is important to note that colloidal systems differ from their atomic counterparts in several ways [49, 50]. First, while motions on the shortest time scales are ballistic in both cases, viscous drag very quickly dissipates momentum in colloids, and motions are best thought of as diffusive rather than ballistic. Second, hydrodynamic effects couple particle motions in complex ways [51]. Simulations suggest that these two differences are unimportant for studying the glass transition [52–57]. A third difference is that colloidal particles are most typically spherically symmetric, and so the geometry of a molecule is usually not replicated in the colloid (see Chap. 4 for recent exceptions). Again, for many cases of interest, this difference is immaterial when studying long-time dynamics; certainly many glass transition simulations study particles with spherically symmetric potentials. A fourth difference is that colloidal suspensions are always slightly polydisperse. This shifts the phase transitions shown in Fig. 1.2 to higher values of ϕ [24, 58, 59], and also in general frustrates crystallization [25, 27, 28, 60, 61]. While this is a distinction in comparison to simple molecular glass-formers, it is less of a distinction with simulations, which often purposefully add polydispersity to frustrate crystallization [62, 63]. Indeed, as noted in the caption of Fig. 1.2, polydispersity appears necessary for a hard sphere glass transition; monodisperse samples always eventually crystallize [27, 28].

1.3   Confinement Effects

Phase transitions are usually investigated in the context of macroscopically large systems. However, confining samples so that one or more dimensions are microscopic leads to new physics, including confinement-driven phases [64]. As relevant to industrial applications, confinement has been shown to modify the mechanical properites of materials; examples include nanolubrication by liquids [65, 66] , and weakening of thin polymer films [67–70], both of which have strong implications for controlling the behavior of miniaturized components. In the context of this dissertation, "confinement" is meant to describe systems which are of limited spatial extent in one, two, or three dimensions while "confinement effect" is meant to highlight generally the difference in a property measured in a confined system relative to the same property measured in bulk.

For amorphous phases, the glass transition temperature T_g is often changed by confinement [69, 71–79]. In some experiments, the glass transition temperature is decreased upon confinement (as compared with the transition temperature in bulk) [69, 74, 75, 80, 81], whereas in others, the glass transition temperature increases [72, 81]. The glass transition temperature has also been seen to increase or decrease for the same material, depending on the experiment [69, 75, 79, 81]; this is likely due to differing boundary conditions [69, 71, 82, 83]. In polymer glass experiments, important differences are found when studying confined samples supported by substrates, as compared with free-standing films [69, 77–79], although recent work demonstrates that multiple mechanisms may be at work for high molecular weight polymers [84]. In other experiments, results depend on whether the confining surface is hydrophobic or hydrophilic, or whether the boundary can be classified as "hard" or "soft" [74, 85]. Computer simulations indicate that confinement influences the arrangement of atoms [80, 81, 86, 87], which might in turn relate to the change of the

glass transition temperature. However, it is difficult to probe the structure and dynamics of nano-confined materials.

Colloids thus can serve as an excellent model system for studying confinement effects. To date, experiments have been performed by two groups who confined colloidal samples between parallel glass plates [88, 89]. Nugent *et al.* used a binary sample to prevent crystallization [88], while Sarangapani and Zhu studied a monodisperse sample [89]. Both experiments used confocal microscopy to observe a dramatic slowing down of particle motion in samples that were very confined. This suggests that the glass plates act analogously to "sticky" boundaries in the molecular glass experiments conducted on substrates, which also find a slowing down of particle motion [69]. Follow-up work by one of these groups observed that rough confining surfaces induced a weak secondary decrease in dynamics [90]. The experiments show a clear connection between layering of particles against the walls and their mobility [88], which has also been studied by simulation [80, 91, 92]. To date, the effect of different boundary conditions on confined colloidal samples has been studied experimentally only as a function of the roughness of the confining surface [90]. Beyond this experimental study, how a confined suspension responds to variation in boundary conditions or properties of the confining medium has not been previously explored.

Presented in Chap. 3 is a series of experiments designed to study how dynamics in a confined colloidal suspension depend on material properties of the confining medium. Results of these experiments demonstrate that, like molecular and polymeric glass formers, observed dynamics can vary significantly depending on the medium in which the suspension is confined. As an example, particle motions decrease more strongly when the viscosity of the external medium is larger.

1.4   Summary of Results and Overview of Dissertation

While each project I worked on during my graduate work relates to understanding some aspect of the glass transition in colloidal systems, each is sufficiently independent enough to warrant its own chapter. Chapter 2 covers relevant background material for the experimental portion of the dissertation. Background material for the two remaining portions of the dissertation are covered in the introductions of their respective chapters.

Chapter 3 covers experimental work relating to the behavior of colloidal suspensions confined within different media. In that chapter, I present the results of these experiments and the methods I used/developed to study such systems. The goal of this project was to demonstrate that the confinement effects observed for polymeric and molecular glass formers discussed in Sec. 1.3 are also present in confined colloidal suspensions, provided that the boundary conditions are modified in appropriate ways. A large advantage of using confocal microscopy coupled with particle tracking techniques is having the ability to directly observe individual particle motions within a sample. Given this ability, I was able to directly observe a dynamical gradient (i.e. particle motions depend on distance from a confining interface), as well as show that the strength of the gradient depends on material properties of the interface and confining medium.

The concepts of potential and free energy landscapes have been widely used in attempts to understand properties of the glass transition in condensed matter systems. The conventional picture of such a landscape is one with hills (energy maxima) and valleys (energy minima), where a system's evolution is related to how it traverses topographical features on the landscape. However, for systems with hard core potentials, such as hard disks or spheres, this picture is incorrect – the landscape is completely flat and the system is governed entirely by entropy. In chapter 4, we introduce a model system, confined

2D Brownian disks, and demonstrate that one can (exactly) obtain an undulating energy landscape by projecting the phase space to a lower dimension. From this point, we relate dynamical properties found in simulations, such as cage breaking, to features on the energy landscape. For example in highly confined systems, the mean time the system spends in a caged state scales Arrheniusly with the height of the free energy barrier.

During my experimental work with confinement, the need very quickly arose for an accurate method of removing collective solid-body-like rotational motions of particles within droplets. With some effort, I was able to refashion an existing numerical technique for this purpose. During this time, Kazem Edmond began experimental work on understanding rotational diffusion of clusters of colloidal particles and was in need of an accurate method for tracking their rotational motions over time. Fortuitously, the method I used to remove the bulk rotations of my droplets is immediately applicable to measuring the rotations of Kazem's clusters. This collaboration, combined with the writing of some supporting algorithms, led to a methods paper and is covered in chapter 5. The method is computationally very fast and applicable to any 2D or 3D system of ≥ 3 non-colinear particles. The technique is able to resolve rotations to $\leq 1.6°$ with moderately noisy confocal data, and to the best of my knowledge is the most accurate of its type found in the literature.

Chapter 2

Experimental Background

This chapter describes information relevant to the experimental portion of this dissertation concerning confinement of colloidal suspensions, as described in Chap. 3. Included are brief overviews of the types of particles used, the techniques of confocal microscopy and particle tracking, and a description of how dynamics are analyzed using mean-square displacements, as related to dilute and dense colloidal suspensions. While these topics are essential for the experimental work, they are somewhat general and best presented here so as to avoid distracting and unnecessary digression in what follows.

2.1   Fluorescent Microspheres

Colloidal particles used here are composed of poly(methyl methacryalate) (PMMA) and are sterically stabilized by a thin surface layer (≈ 20 nm) of poly-(12 hydroxystearic acid) (PHSA), which prevents aggregation due to van der Waals forces. It is this steric stabilization layer that allows particles to be considered as hard spheres [93]. Particles are dispersed in a mixture [85/15 (w/w)] of cyclohexyl bromide (CXB) and decahydronaphthalene (decalin, DCL), which closely matches both the density and refractive index of the

particles. This minimizes gravitational effects and van der Waals attractions, and allows for visualization via confocal microscopy.

Particles are made fluorescent by the addition of Nile Red dye during synthesis. The excitation and emission spectra of Nile Red in general depends on solvent, but for the particles used here excitation and emission are maximum at 532nm and 582nm, respectively.

2.2 Confocal Microscopy

Conventional optical microscopes are not well-suited for three-dimensional microscopy. In order to see deep within a sample, it is necessary to minimize the scattering of light by closely matching the refractive indices of the particles and solvent. However, this means that distinguishing between particles and solvent becomes more difficult; conventional optical microscopy relies on differences in index of refraction between parts of the sample to produce an image. Fluorescence microscopy overcomes this by using the contrast between dyed and undyed portions of the sample to produce an image. This works well for dilute samples, but is poorly suited for dense systems such as colloidal glasses. Because the sample is nearly transparent, objects outside of the focal plane are fluoresced, and this stray background light passes readily through the optics and can severely muddle an image: it is hard to distinguish bright particles on a bright background. Confocal microscopes use fluorescence as well, but overcome this limitation with special optics (described below) and are much better suited for studying dense colloidal systems.

The functioning of a confocal microscope hinges on two principles: illumination of a small sample volume ($\leq 10^{-15}L$) and rejection of out-of-focus light [94]. A schematic of a confocal microscope is shown in Fig. 2.1. Laser light, shown in black (blue in color), passes through a dichroic (dichromatic) mirror and onto rotating mirrors that scan the light
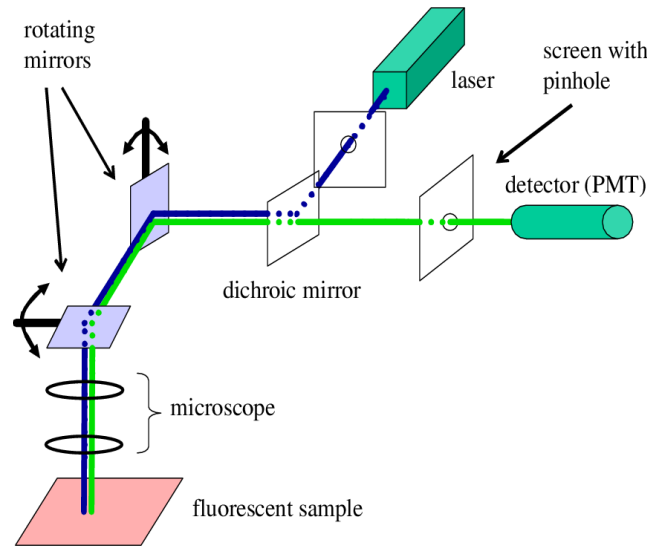
Figure 2.1: Schematic of a confocal microscope. Rotating mirrors scan the incoming laser light over the region of interest in the sample. The emitted light follows the reverse optical path until arriving at the dichroic mirror, where it passes through the pinhole and into the detector. A dichroic mirror reflects light below a certain wavelength and transmits light above it. Reprinted with permission from [94].

in the horizontal planes. The light then passes through the microscope optics and excites the fluorescent sample. The emitted light, shown in dark gray (green in color), follows the reverse optical path back to the dichroic mirror, where it is reflected onto a screen with a pinhole. The pinhole is placed in the *conjugate focal* plane of the sample (hence the term *confocal*), rejecting the vast majority of out-of-focus light and limiting the depth of field [95]. The remaining in-focus light is finally collected by a detector, such as a photomultiplier tube.

Confocal microscopy allows for direct imaging of a sample in two or three dimensions. In 2D, the pixels of an image are constructed by scanning individual points (point scanning microscopes) or lines of points (line scanning microscopes) over a sample. The highest rates of scanning are achieved with use of an acousto-optical device (AOD), in which one of the mirrors in Fig. 2.1 is replaced with a crystal that acts as a diffraction grating
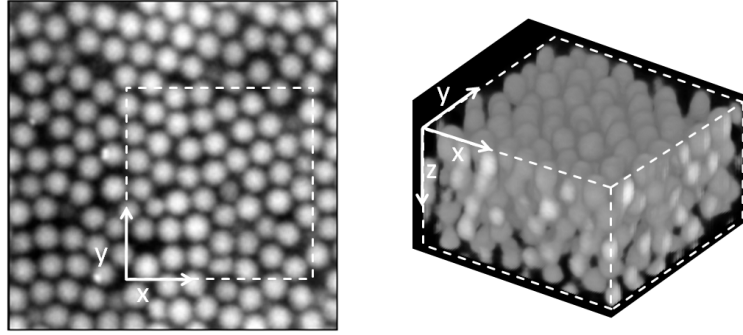
Figure 2.2: Left: Confocal micrograph of a monodisperse colloidal system at volume fraction $\phi \approx 0.63$. The particles have diameter $2a = 2.1$ μm and the image is taken at the coverslip, where the particles layer against the wall. Right: 3d reconstruction of boxed region on the left. Here, the image dimensions are $15 \times 15 \times 10$ μm^3.

whose grating spacing can be tuned with high frequency mechanical vibrations [96, 97].

To obtain 3D images, such as shown in Fig. 2.2, the 2D scanning procedure is quickly repeated while the focal plane is advanced through different depths in the sample. In the fastest modern confocals, 2D images can be collected at rates ≈ 100 frames/s, and depending on the scanning depth 3D images can be collected in around 1 s.

2.3 Particle Tracking

Particle tracking incorporates various image processing and computational techniques to identify the centroid positions of particles in a given image [95, 98, 99]. The image shown in Fig. 2.3(a) is a raw 2D image of a binary (two particle sizes) suspension confined within an emulsion droplet. Here, both large and small particles are visible. By applying a spatial bandpass filter, one can enhance contrast for the large particles while almost completely filtering out the small, as shown in Fig. 2.3(b). From this point, one uses computational algorithms to locate local maxima within in image, which correspond to the centers of individual large particles. Fig. 2.3(c) shows the locations of the local maxima plotted on top of the original image in Fig. 2.3(a). If desired, the small particles can
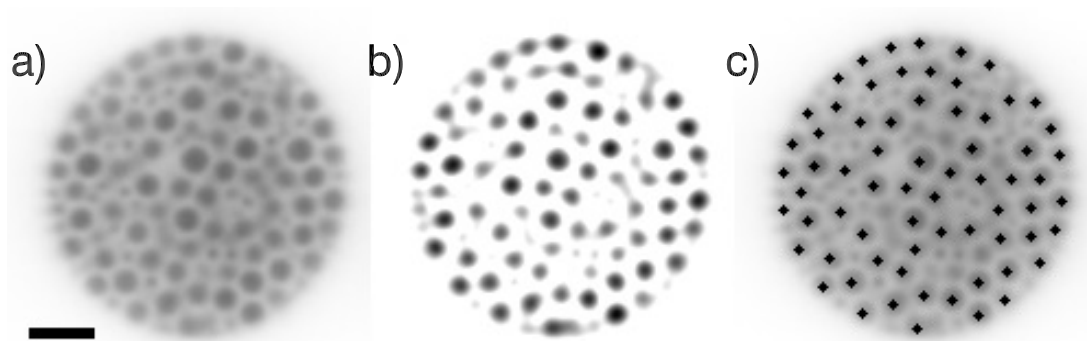
Figure 2.3: (a) Raw confocal image of a binary colloid-filled emulsion droplet. Scale bar is 5 μm. (b) The confocal image after a spatial bandpass filter is applied. (c) Centers of the large particles identified from tracking algorithms overplotted with the original image.

be located in a similar way by using a different spatial filter and repeating the search for local maxima. The image in Fig. 2.3 is a two-dimensional example, but images can also be three-dimensional. Repeating the centroiding procedures for consecutive images yields a list of coordinates at subsequent times. The coordinates can be used immediately to obtain structural information about a sample, or if dynamic information is desired, the coordinates can be linked together in time to form individual particle trajectories.

In general, the larger a particle is in an image, and the more it contrasts with the background, the more accurate the particle tracking. For many experiments, particle centers can be located with a resolution of $\approx$ 20 nm in the focal plane, while the out-of-plane resolution is typically no better than 50 nm.

In dilute samples, accurately identifying particles is relatively easy because bright and well-separated particles contrast well with the dark background. In dense samples like colloidal glasses, there are many bright particles in an image and so contrast is usually poorer. Additionally, optical effects such as diffraction can make it difficult to distinguish individual particles when they are very close together. These effects are important to understand and correct, especially when particle motions are very small [100, 101]. To

illustrate, in a sample of 2.4 μm PMMA spheres at $\phi = 0.52$, Weeks and Weitz observed the majority of particles to move less than 0.2 μm over 600 s [102]. The influence of diffraction can be weakened by increasing the optical resolution by using fancier lenses [103], by using confocal microscopy, or with computational techniques [100, 104]. Hence, with some care as far as optics are concerned, and some fine tuning of particle tracking parameters, it is often straightforward to study dilute and dense systems with the same techniques.

Combined with video microscopy, particle tracking offers a powerful method to probe the local properties of a sample, which is especially important for understanding structurally or dynamically heterogeneous systems like colloidal glasses. With this technique, one can discuss behaviors of individual particles up to a collection of several thousand.

2.4 Brownian Motion and Diffusion

The size of colloidal particles is such that they execute Brownian motion due to frequent, random collisions with solvent molecules. These collisions are random in magnitude and orientation and so the average particle displacement in a particular direction $\langle \Delta x \rangle$ is zero. Instead, motion is often quantified by the mean square displacement (MSD), which in one dimension is given by

$$\langle \Delta x^2 \rangle = \langle [x(t + \Delta t) - x(t)]^2 \rangle = 2D\Delta t. \tag{2.1}$$

The angle brackets $\langle \rangle$ indicate an average over all particles and all initial times t for a particular lag time Δt, and D is the diffusion coefficient. In three dimensions, Eqn. (2.1) becomes

$$\langle \Delta r^2 \rangle = 6D\Delta t. \tag{2.2}$$

The diffusion coefficient is a function of temperature T, solvent viscosity η, and particle size a. In the limit of infinite dilution ($\phi \to 0$), D is given by the Stokes-Einstein-
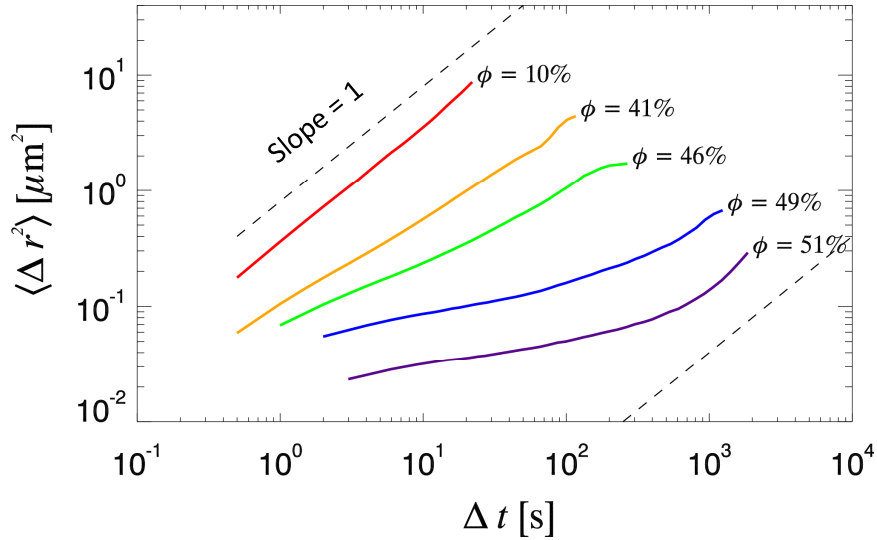
Figure 2.4: Mean square displacements for large particles in binary colloidal suspensions at various volume fractions. The data here is from 2D particle tracking of a 3D sample. Small and large particles have radii 0.532 μm and 1.08 μm, respectively, and are at a number ratio (small/large) of ≈ 0.9. Dashed lines indicate a slope of one.

Sutherland relation,

$$D = \frac{k_B T}{6\pi\eta a},\tag{2.3}$$

where k_B is Boltzmann's constant [105, 106]. This equation implies that T, η, and a do not play a direct role in the colloidal glass transition; they only influence D, which sets the time scale for particle motion.

For purely diffusive motion, such as in a dilute suspension, the MSD scales with Δt. Thus, on a log-log plot of $\langle \Delta r^2 \rangle$ vs. Δt, one expects a straight line with a slope of unity. Shown in Fig. 2.4 are MSDs for a colloidal samples from $\phi = 0.10$ to $\phi = 0.51$. For these data, $\phi = 0.10$ exhibits purely diffusive behavior over the duration of the experiment (indicated by a slope of one), whereas the data for larger ϕ show quantitatively and qualitatively much different behavior. While in general an increase in ϕ corresponds to a slowing of dynamics, the mechanism behind the slowing at larger ϕ is fundamentally different than for lower volume fractions.

The difference arises because of the presence of neighboring particles. At the smallest Δt, particles are effectively unaware of their neighbors and so MSDs show diffusive behavior (see for example $\phi = 0.41$ in Fig. 2.4). Note that for $\phi > 0$ that the diffusion constant obtained from short time-scale motion, D_S, differs from that of Eqn. (2.3) due to hydrodynamic interactions between the particles [107–111]. By around $\phi \approx 0.3$, D_S drops to approximately 50% of the value from Eqn. (2.3) [2].

For larger ϕ at moderate lag times, a plateau develops in the data of Fig. 2.4 which is indicative of particles being trapped in cages formed by their neighbors. At these time scales, particles are localized and large cumulative motions are suppressed [3, 112–117]. At sufficiently long Δt, particle rearrangements do occur, and so the MSD again increases, eventually recovering diffusive behavior. As ϕ increases from left to right, one observes a lengthening of the plateau and thus increasingly slowed dynamics, indicating that longer and longer time scales are needed for significant particle rearrangements to occur. The overall shapes of the MSDs in Fig. 2.4 are typical of dense suspensions.

Chapter 3

Boundary Effects in Confined Colloidal Suspensions

3.1 Introduction

The behavior of confined materials has attracted considerable scientific interest due to the relevance for technological and industrial applications. As discussed in Sec. 1.3, materials confined to sufficiently small length scales can exhibit changes in mechanical properties, such as moduli or stiffness, relative to the same properties measured in a bulk sample [65–70]. Such changes in characteristic behaviors of materials have strong implication for the miniaturization of mechanical and electronic components. While significant progress has been made to understand confinement effects in many different systems, much of the underlying physics remains obscure.

As noted in Sec. 1.3, how a material responds to confinement is not only dependent on length scale but also depends quite strongly on the interactions between the material and the confining interface. Indeed, the measured properties of a confined material, such as the

change in T_g, may shift from one extreme to the other by varying the boundary conditions

of confinement [82, 83].
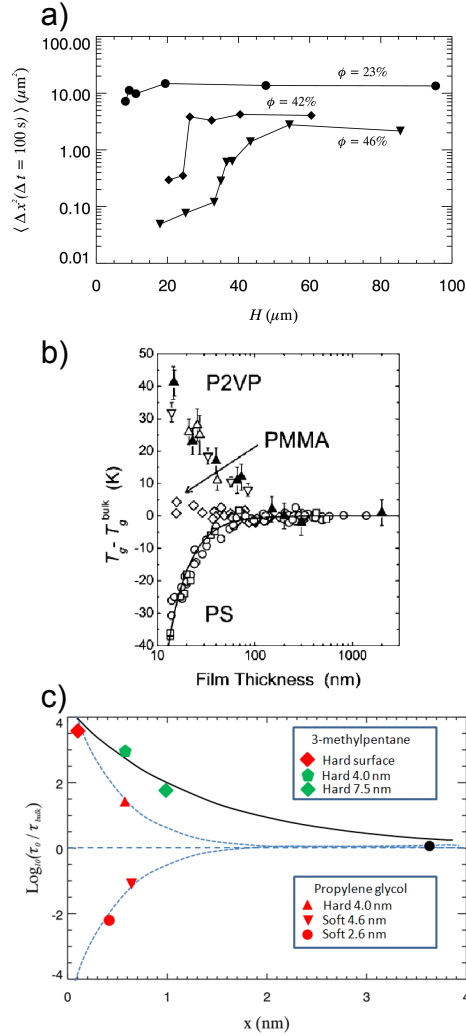
Figure 3.1: Confinement effects in various systems. (a) Binary colloidal suspension confined between hard glass walls. Here, the MSD (see Sec. 2.4) at $t = 100$ s is plotted as a function of the confinement height. (b) Supported ultra-thin film polymers with one free surface. The change in glass transition temperature ΔT_g is plotted as a function of film thickness. (c) Molecular liquids in hard (top) and soft (bottom) 3D confinement. The relaxation time τ relative to the bulk is plotted as a function of distance to the nearest confining boundary. Data for figures (a,c) are taken respectively from [88], [83]. Panel (b) is reprinted with permission from [79]. Copyright 2007 American Chemical Society.

To illustrate the variety of confinement effects in different systems, we show in

Fig. 3.1 data from confined glassy colloidal, polymeric, and molecular systems. The results

from a system of confined binary colloids are given in Fig. 3.1(a). Here, the value $\langle \Delta r^2(t =$

$100\text{s})\rangle$ (see Sec. 2.4) was chosen as a measure of dynamics [88]. The system is confined

in 1D within hard glass walls separated by a distance H on the order of microns, while

the other dimensions extend to macroscopic distances. At large H, these systems have

dynamics similar to an unconfined bulk sample. However, as the size of the confined system

shrinks, one finds an abrupt decrease in MSD for $\phi = 0.42$ and $\phi = 0.46$ within the

supercooled regime. Data for $\phi = 0.23$ is unaffected by confinement except at the smallest

values of H, which is likely the result of hydrodynamic interactions with the wall. The

decrease in dynamics for larger ϕ shows that confinement effects are important for colloidal

systems, and the values of H where dynamics begin to slow indicate important length scales

associated with confinement; above these H, the systems are essentially unaware of the

confining boundaries and behave as bulk samples. One sees in Fig. 3.1(a) that an increase

in ϕ corresponds to dynamical slowing at larger values of H, and one may conclude that

important length scales associated with confinement are also a function of ϕ. For confined

colloids then, the effect of confinement seems consistently to be a reduction in dynamics.

For polymeric and molecular systems shown in Fig. 3.1(b) and (c), the effect

of confinement is richer. The systems in Fig. 3.1(b) are ultra-thin supported polymer

films with one free surface. Here, one finds that, depending on the polymer in question,

confinement may lead to an increase or decrease in T_g [Poly(2-vinylpyridine) (P2VP) and

Polystyrene (PS)], respectively, or confinement may have little effect [Poly(methyl methacry-

late) (PMMA)]. In polymer systems, it has been observed that mobility is enhanced at free

surfaces relative to bulk measurements [79, 118]. It is believed that a thin liquid-like layer

exists at the free surface and that a dynamical gradient exists between the free surface

and the bulk [71, 119–121]. Indeed, very strong evidence exists for a gradient in dynam-

ics [77, 78, 121, 122]. How strongly the free surface affects dynamics depends on the chemical structure of the polymer [79, 123, 124]. However, the key difference between the systems in Fig. 3.1(b) are the interactions with the polymers at the substrate. For P2VP and PMMA, hydrogen bonding occurs at the polymer-substrate interface, whereas this is not the case for PS. These attractive interactions lead to a decrease in mobility near the interface, and as with the free surface, it is believed that this effect propagates into the rest of the sample. Hence, strong interactions with the substrate can oppose the enhancement of dynamics due to a free surface [79]. Overall, this demonstrates that confining a system to small spatial scales does not specifically lead to enhancement or suppression of dynamics, but is strongly dependent on how the confined material interacts with the external confining medium. As well, if boundary conditions are neutral, confinement can have no appreciable effect [118].

For molecular glassformers, results are analogous to those from polymer measurements. Shown in Fig. 3.1(c) are relaxation times (relative to bulk measurements) plotted as a function of size of the confined sample. This graph distinguishes "hard" and "soft" confinement: here, hard refers to the sample being confined within a hard glass (SiO$_2$) pore with solid immobile walls; soft confinement refers to samples being confined within microemulsion droplets with a liquid-like mobile boundary. For the case of hard confinement, relaxation times are observed to increase as system size is decreased. Presumably, the molecules near the boundary are less mobile near an immobile boundary than in a bulk material due to dynamical restrictions associated with being near a hard wall. In smaller confinement, a greater proportion of the sample is exposed to the interface, leading to an increase in the average relaxation time. In contrast for soft confinement, average relaxation times decrease relative to the bulk because the mobile liquid-like boundary poses less of a dynamical constraint than in bulk or near an immobile boundary [74, 82, 83, 85]. As with polymers, it is believed that in confined molecular liquids, a dynamical gradient exists as

a function of distance to the confining boundary [82, 83]. Recent experiments with polymers have explored similar notions of hard and soft confinement and have found similar results [125, 126].

The effect of different boundary conditions on confined colloidal samples has been studied experimentally only as a function of the roughness of the confining surface [90]. Beyond this experimental study, the response of a confined colloidal suspension to varying material properties of the confining media has not been explored. Thus, one cannot immediately compare the behaviors of confined molecular and polymeric systems to that of colloids. Here, we present a series of experiments that probe how dynamics in confined suspensions are influenced by material properties of the external confining medium. We will show that confined colloids behave analogously to confined polymers and molecular liquids, with similar dependence on boundary conditions under confinement. Further, we will show that a dynamical gradient exists as a function of distance to the confining boundary, and that the strength of this gradient is a function of the material properties of the confining medium.

3.2   Methods

3.2.1   Sample Preparation

We use a binary colloidal suspension of small and large PMMA microspheres with radii $a_S = 0.532$ μm and $a_L = 1.08$ μm, respectively. A binary, rather than monodisperse, system is chosen to frustrate crystallization. The microspheres are dispersed in a solvent mixture of CXB and DCL oils, as described in Sec. 2.1. The density of the colloidal suspension is approximately 1.19 g/mL and the index of refraction is 1.492. The solvent is saturated with tetrabutylammonium bromide salt (TBAB) to minimize electrical repulsion

between particles and produce near hard sphere behavior [127, 128].

Two separate mixtures of glycerol and deionized water, 50/50 (w/w) and 65/35 (w/w), are used as external phases to vary the boundary conditions of confinement. The 50/50 and 65/35 external phases have viscosities η_x of 5.7 mPa·s and 15.2 mPa·s, respectively. Though the viscosities of the external phases only differ by a factor of 2.7, this amount is sufficient to produce a significant difference in the motions of particles within the oil droplets. These particular mixtures lie near the extremes of what can be successfully used to encapsulate *and* still observe the colloidal suspension using confocal microscopy. The density of the external phase must be smaller than the density of the suspension so that the droplets sediment to the coverslip, enabling visualization with an inverted confocal microscope. This places an upper limit on amount of glycerol in the mixture at $\approx 74\%$. However, the viscosity of a 74/26 mixture is ≈ 34 mPa·s, and creating the droplets by gentle shaking is unreliable for $\eta_x \gtrsim 20$ mPa·s. Additionally, the index of refraction of the external phase must be relatively close to that of the suspension. The index of the 50/50 mixture (1.398) is approximately the smallest that can be used while allowing reliable particle tracking. Material properties of the 50/50 and 65/35 mixtures are summarized in Tab. 3.1.

A small amount (3mM) of sodium dodecyl sulfate (SDS) surfactant is added to the glycerol+water mixture to prevent coalescence of the emulsion droplets with each other and the walls of sample chamber. The SDS has the added effect of minimizing protrusion of colloidal particles into the glycerol+water phase [129]. Once the individual components are correctly weighed, they are mixed and stirred thoroughly over a period of ≈ 24 hrs.

Droplets are prepared by first adding $\approx 200\mu$L of the external phase into a vial, then gently pipetting $\approx 40\mu$L of colloid on top. A gentle shaking by hand shears the two fluids and creates colloid-filled droplets in a glycerol+water phase. Prior research on similar polar+non-polar mixtures has demonstrated that dissolved ions may migrate from the non-

polar to polar phases [128]. The migration takes place over a period of $\approx$ 24 hrs., after which the electrical properties of the mixtures stop evolving. For this reason, droplets are allowed to quiesce in the external phase for a period of 24 hrs. before taking data.

This procedure produces droplets with a wide range of radii R, internal volume fraction ϕ, and number ratio n_S/n_L. For the data presented here, the number ratio within droplets ranges from 0.78 to 1.83, but we stress that over this range, we observe no dependence of results on number ratio. We do, however, observe a strong dependence on droplet size and volume fraction, hence R and ϕ will be used as control parameters.

Table 3.1: Properties of External Glycerol/Water Phases

Composition (w/w)	ρ [g/mL]	η_x [mPa·s]	n
50/50	1.124	5.7	1.398
65/35	1.165	15.2	1.420

3.2.2 Sample Chambers

Simple sample chambers, illustrated in Fig. 3.2(a), are fabricated using standard glass microscope slides, coverslips, and UV epoxy. Sample chambers are filled with the glycerol+water+droplet mixture, sealed with UV epoxy, inverted and placed on a confocal microscope. A 100× oil objective is coupled to the sample chamber via a small amount of immersion oil.

3.2.3 Visualization of Droplets and Data Collection

After sample chambers have been filled and sealed, they are placed inverted on the confocal microscope, as indicated in Fig. 3.2(b). At this point, droplets are dispersed throughout the sample chamber. The working distance of the 100× objective lens is 100 μm, which is to say that only objects within this distance of the coverslip can be viewed.
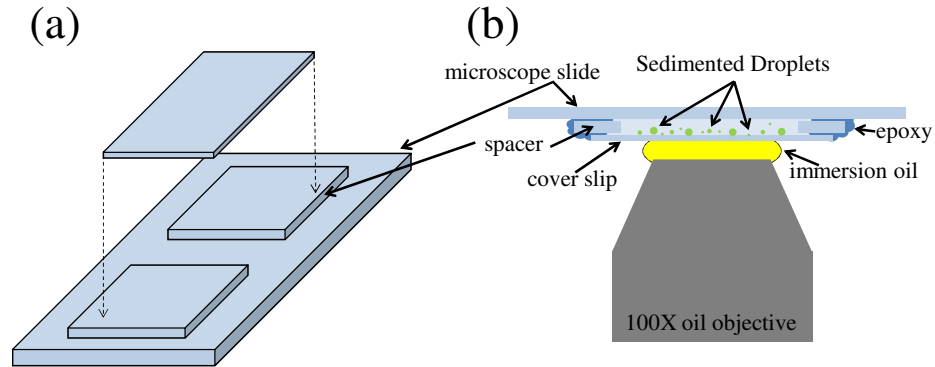
Figure 3.2: (a) Fabrication of sample chamber. Spacers ≈ 200 μm thick are sandwiched between a microscope slide and coverslip and fixed in place with UV epoxy. (b) Colloid-filled emulsion droplets sediment to the bottom of the sample chamber and are visualized with a confocal microscope.

In practice, the difference between the indices of refraction for the suspension and external phases further limit this distance to $\lesssim 25$ μm, which places an upper bound on the size of droplet which can be studied.
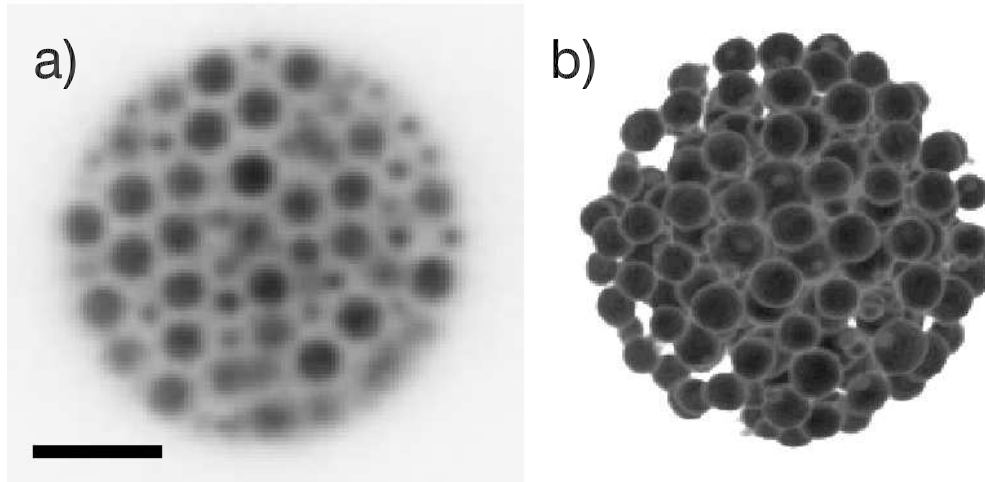
Figure 3.3: (a) Slice through the center of a 16.4 μm diameter emulsion droplet filled with a binary colloidal suspension. Here, $\phi = 0.465$. The scale bar indicates 5 μm. (b) 3D volumetric rendering of the droplet in (a). Shading has been performed to enhance visualization.

Shown in Fig. 3.3(a) is a 2D slice through the center of a colloid-filled emulsion droplet. Both large and small particles are visible, however we only use the motions of

the large particles when discussing dynamics. This is done for three reasons. First, small particles are included in the suspension in small quantities only to frustrate crystallization. As can be seen in Fig. 3.3(b), large particles occupy the majority of the volume. Second, larger particles move slower and are easier to identify, which results in more precise particle tracking. Finally, to track the small particles, one needs to image the sample more frequently which increases the rate of photobleaching and limits the duration of experiments.

Data sets used in the following analyses are primarily 2D, but 3D sets are also included. While the droplets are of course 3D objects, observations through the central cross section of a droplet are considered 2D data. For each 2D data set, 3D images are also taken of the droplet so that volume fraction can be measured, as discussed in Sec. 3.2.7.

In the present studies, 2D data is preferable because it allows for motions to be tracked over longer periods of time before photobleaching the sample and yields slightly better particle tracking resolution. As will be shown in Sec. 3.3, observed behaviors are independent of the dimensionality of the data set.

3.2.4 Removing Bulk Translational Motion

Over the course of an experiment, droplets are sometimes observed to translate in the x- and y-directions. This drift can be due to weak fluid flows present in the sample chamber or, for long experiments, Brownian motion of the droplets themselves. Shown in Fig. 3.4(a) are trajectories of particles within a droplet over 300 s. During this period, the entire drop translates toward the upper left of the figure. The trajectory of the droplet center is shown in the inset of Fig. 3.4(a).

It is necessary to remove this bulk drift from the particle trajectories to determine particle motions within the droplet. After some small time interval Δt, the x-coordinate of a particle i can be described by
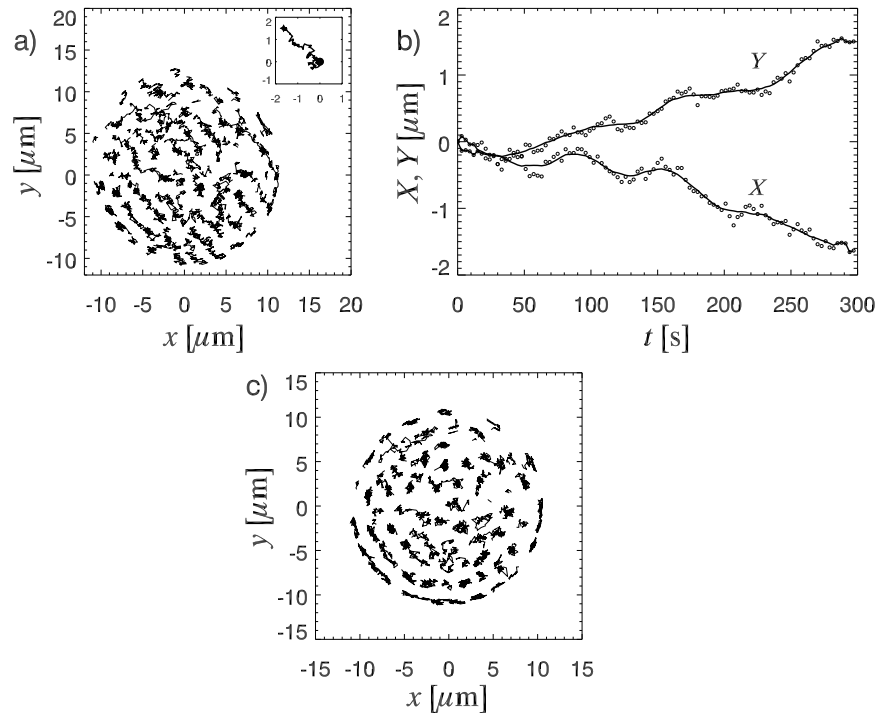
Figure 3.4: (a) Raw trajectories of particles within a 23.4 μm diameter droplet showing drift over time. Here, $\phi = 0.457$. Inset: Trajectory of the droplet center of mass, beginning at the filled circle and ending at the star. (b) Droplet center trajectories in each direction over 300 s. Open circles are the calculated center positions $X(t)$ and $Y(t)$ and solid lines are the average motions subtracted from the particle trajectories. (c) Particle trajectories in (a) after drift is subtracted.

$$x_i(\Delta t) \;=\; x_i(0) + \Delta x_i,$$

$$x_i(\Delta t) \;=\; x_i(0) + \delta_i + \Delta \bar{x}, \tag{3.1}$$

$$\Delta \bar{x} \;=\; \frac{1}{N}\sum_{j=0}^{N} \Delta x_i, \tag{3.2}$$

where Δx_i is the total displacement of i during the time interval. The total displacement can be separated into the sum of δ_i, which represents a Brownian displacement of an individual particle, and $\Delta \bar{x}$, which is the average displacement of all particles within a droplet, given by Eqn. (3.2). Analogous expressions can be used to describe motions in the y-direction. For a stationary droplet, $\Delta \bar{x}$ is zero, and all motion is due to diffusion. In a system with drift, the x-coordinate of the droplet center is given by

$$X(t) = \sum_{t'=0}^{t} \Delta \bar{x}(t'). \tag{3.3}$$

The x- and y- trajectories of the droplet center are shown in Fig. 3.4(b) as open points. As can be seen, there can be significant fluctuations in position from one time to the next. These fluctuations are due to a combination of true motions and particle tracking noise. Rather than immediately subtract these raw trajectories and possibly remove interesting motions, the trajectories at each t are "smoothed" by averaging over a small window, $[t - \delta t, t + \delta t]$. This produces the solid curves shown in Fig. 3.4(b). The smoothed droplet center trajectories are finally subtracted from the individual particle trajectories, yielding motions such as shown in Fig. 3.4(c).

3.2.5 Removing Bulk Droplet Rotational Motion

The emulsion droplets used here are in some cases small enough to show significant amounts of rotational diffusion over the duration of an experiment. Shown in Figs. 3.5(a)

and (c) are particle trajectories within two droplets of different sizes after bulk translational motions have been subtracted. As with translational drift, in these cases it is necessary to subtract bulk rotational motions in order to accurately determine the relative motions of particles within a droplet. Shown in Figs. 3.5(b) and (d) are particle trajectories after removing bulk rotational diffusion for the two droplets. As can be seen, subtracting bulk rotational motions is much more important for smaller droplets, but these diffusive motions can be significant for even the largest droplets studied here. The method for subtracting bulk rotational diffusion is identical to the matrix methods described in detail in Chap. 5 and in [130]. Using this technique, we estimate the uncertainty in resolving an angular displacement as $\approx 0.1°$.
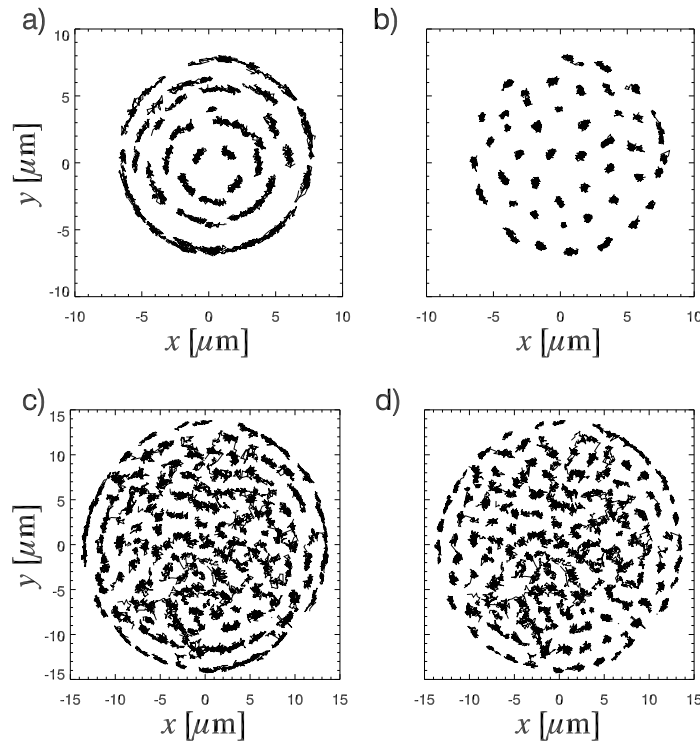
Figure 3.5: (a),(b) Trajectories of particles within a 16.4 μm diameter droplet before (a) and after (b) removing rotational diffusion. Here, $\phi = 0.466$. (c), (d) Trajectories of particles within a 28.8 μm diameter droplet, with $\phi = 0.458$, before (c) and after (d) removing rotational motions. Trajectories in all panels cover a period of 600 s.

3.2.6 Measuring Droplet Size

Due to diffraction, images such as the one shown in Fig. 3.3(a) cannot be used to accurately determine the radius R of a droplet. Instead, after bulk translational and rotational diffusive motions have been subtracted, the size of the droplet can be measured using the positions of the tracked particles. Specifically, this is done by creating radial histograms of the particle positions. For a d-dimensional data set, the number of observed particles n at a distance r from the center of the droplet grows as

$$n(r) \propto r^{d-1} \rho(r). \tag{3.4}$$

In Eqn. (3.4) , $\rho(r)$ is a density with units $[\mu\mathrm{m}^{-d}]$. Shown in Figs. 3.6(b) and (d) are radial histograms from 2D data sets, plotted as $r\rho(r)$, for two different droplets. Both histograms exhibit oscillations related to the layering of particles within the droplet, which has also been seen in 1D confinement experiments with hard walls [90, 131, 132], simulations [92, 133–135] and seems to be a generic feature of confined particle systems. Both histograms are also strongly peaked around particular values of r. Ideally, no large particles should exist closer than a distance a_L from the physical boundary of the droplet, and therefore histograms should peak at $r = R - a_L$ and then decrease sharply to zero. However, due to small levels of tracking noise, the peaks of the histograms are slightly broadened, as can be seen in Figs. 3.6(b),(d).

To determine the size of a droplet, we perform a local Gaussian fit of the form

$$A \exp\left[\frac{(r - r_p)^2}{2\sigma_R^2} \right] \tag{3.5}$$

to data in the vicinity of the maximum in $\rho(r)$, which yields the location of the peak r_p. The true size of the droplet is then taken to be $R = r_p + a_L$. The quantity σ_R provides a convenient estimate of the experimental uncertainty in droplet radius. For the data
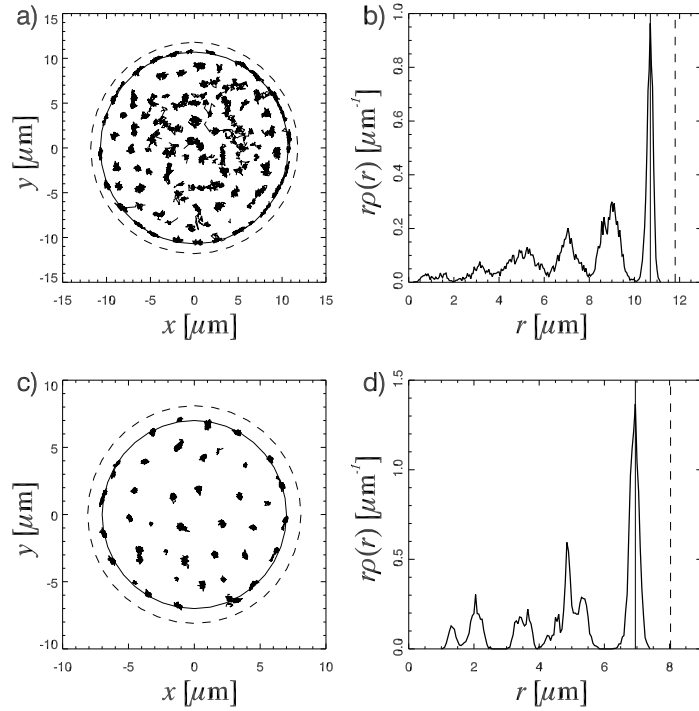
Figure 3.6: Measurements of droplet size: $R = 11.76$ μm for (a),(b) and $R = 8.18$ μm for (c),(d). Panels (a),(c) show trajectories of particles overplotted with droplet size measurements. The solid line represents r_p, the calculated position of the peak in the radial histogram, and the dashed line represents the physical boundary of the droplet R. Panels (b),(d) show the radial histograms used to calculate the droplet sizes. The solid and dashed vertical lines have the same meaning as in (a) and (c).

presented here, $\sigma_R \approx 0.1$ μm for 2D data sets and $\sigma_R \approx 0.15$ μm for 3D data sets.

3.2.7 Measuring Volume Fraction

The volume fraction for a suspension of small and large spheres within a spherical droplet is given by

$$\phi = \frac{n_S a_S^3 + n_L a_L^3}{R^3}. \tag{3.6}$$
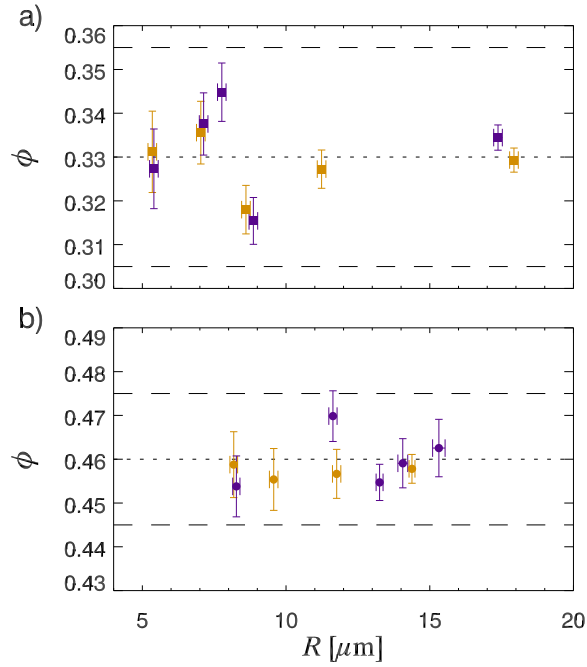
Figure 3.7: (a) Volume fractions for droplets of radius R for $\phi = 0.330 \pm 0.025$. (b) $\phi = 0.460 \pm 0.015$. Color indicates the viscosity of the external phase: $\eta_x =$5.7 mPa·s (gold), $\eta_x = 15.2$ mPa·s (navy). Dotted lines indicate the center of the ϕ range and dashed lines indicate the edges of the range.

Therefore, once R is known, one only needs an accurate count of particles within the droplet. Particles within a droplet are counted using a combination of spatial filters and centroiding, as described in Sec. 2.3 and illustrated in Fig. 2.3. Each image is *highly* scrutinized (by hand and by eye) to ensure an accurate count. The uncertainty σ_R in droplet radius leads

to an uncertainty in volume fraction

$$\sigma_\phi \approx \phi \frac{\sigma_R}{R}, \tag{3.7}$$

for each droplet. Shown in Fig. 3.7 are the measured volume fractions and droplet radii for data sets with moderate volume fractions, $\phi \approx 0.330$, and high volume fractions, $\phi \approx 0.460$. As described in Sec. 3.2.1, ϕ within a droplet is not precisely controllable, hence for this work we will compare droplets over two ranges of volume fraction: $\phi = 0.330 \pm 0.025$; $\phi = 0.460 \pm 0.015$. For the data presented here, slight variations in ϕ between data sets seem to be unimportant. Likewise, any systematic uncertainty due to polydispersity in particle size, $\sigma_a/a \approx 0.05$, appears unimportant for the results that follow.

3.3 Results

3.3.1 Slowing of Dynamics in Confinement

The effect of varying η_x is immediately apparent from inspecting particle trajectories, such as those shown in Fig. 3.8. The droplets in both panels have similar radii, volume fractions, and the shown trajectories are over an equal 600 s duration. The most significant difference between these systems is the viscosity of the external phase: 5.7 mPa·s in (a); 15.2 mPa·s in (b).

As shown, particles within a droplet exposed to a lower viscosity external phase are much more mobile than when the external viscosity is larger. To quantify these differences in dynamics, we compare the MSDs (see Sec. 2.4) of particles within different sized droplets exposed to different external phase viscosities. Panels (a),(b) of Fig. 3.9 are from 3D data sets and show the MSDs of systems at $\phi = 0.330 \pm 0.025$ and different η_x [5.7 mPa·s in (a),(c) and 15.2 mPa·s in (b),(d)]. The curves in each panel are particle MSDs within
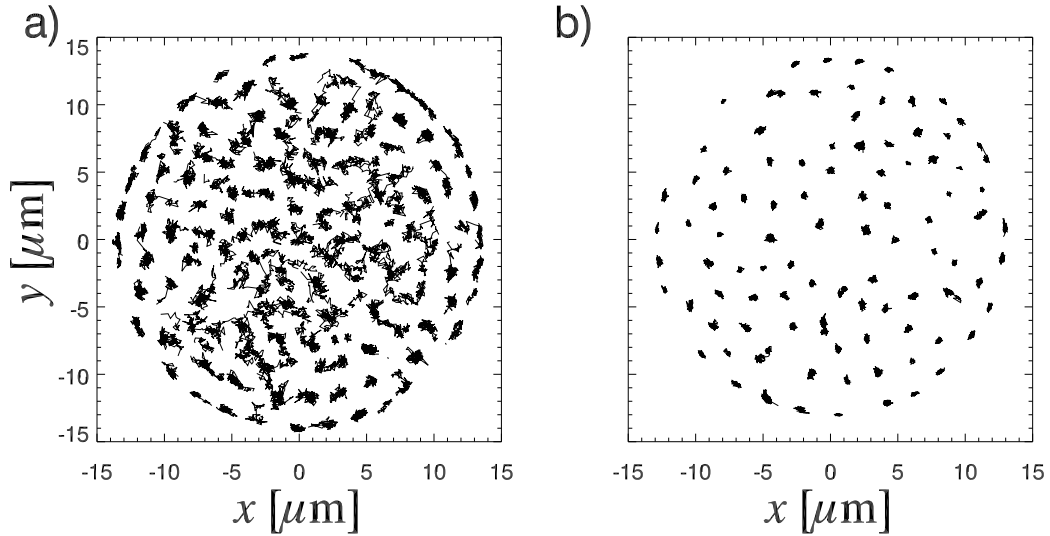
Figure 3.8: (a) Trajectories of particles within a 14.4 μm radius droplet with $\eta_x = 5.7$ mPa·s and $\phi = 0.458$. (b) Trajectories within a 14 μm droplet with $\eta_x = 15.2$ mPa·s and $\phi = 0.459$. The elapsed time in both panels is 600 s.

droplets of different radii, with size decreasing from blue to red. In Fig. 3.9(a), the MSDs are very similar, but do indeed exhibit a slight slowing of dynamics when droplet size is decreased. When η_x is larger, as in Fig. 3.9(b), a decrease in dynamics with smaller R is much more apparent. At this volume fraction, $\phi = 0.330 \pm 0.025$, the samples are colloidal fluids [14]. From the linearity of the MSDs in Fig. 3.9(a,b), these samples do indeed appear nominally diffusive (see Sec. 2.4), with no obvious indications of the dynamical plateaux seen in supercooled liquids or glasses. However, it is apparent from these data that in addition to a change in droplet size, a variation in the external confining medium also causes changes of particle dynamics within the droplets.

The slowing of dynamics is more pronounced in droplets with larger internal volume fractions, as can be seen in Figs. 3.9(c),(d) with $\phi = 0.460 \pm 0.015$. Here, the MSDs for both η_x are well-separated and again, as droplet size decreases so does the MSD. Directly comparing panels (c) and (d), one sees that decreasing droplet size does not cause an equal decrease in motion between droplets in different external phases. Examining the top curves
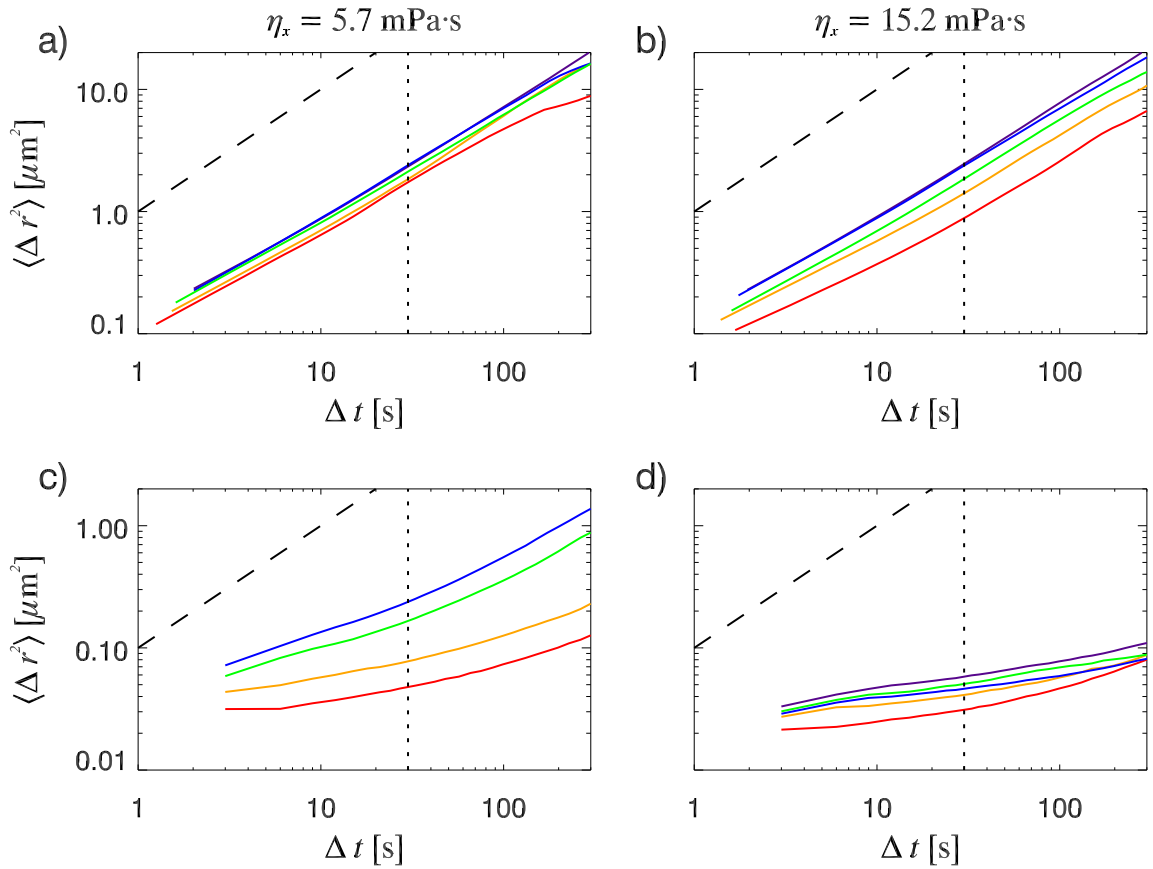
Figure 3.9: Particle mean square displacements in droplets of different sizes with different boundary conditions: (a),(c) $\eta_x = 5.7$ mPa·s, (b),(d) $\eta_x = 15.2$ mPa·s. For (a),(b) $\phi = 0.330 \pm 0.025$ and for (c),(d) $\phi = 0.460 \pm 0.015$. (a) Here, the effect of droplet size R can be seen but is difficult to distinguish. See Tab. 3.2 for values of R. For (b-c), droplet radii from top to bottom (b) 8.86, 17.37, 7.76, 7.13, 5.4 μm. (c) 14.40, 11.76, 9.57, 8.18 μm. (d) 15.32, 13.26, 14.06, 11.63, 8.20 μm. Dashed lines indicate a slope of one. Dotted lines are placed at $\Delta t = 30$ s.

in these panels [$R = 14.40$ μm in (a) and 15.32 μm in (d)], systems exposed to a higher η_x are initially offset toward smaller $\langle \Delta r^2 \rangle$.

Colloidal systems at these ϕ are near the phase boundary of the liquid and super-cooled regimes shown in Fig. 1.2 for monodisperse systems. However, MSDs in Fig. 3.9(c),(d) show subdiffusive behavior typical of supercooled liquids. These types colloids are typically found to possess a slight electrical charge, which shifts the supercooled regime to lower ϕ. As can be seen in Fig. 2.4, unconfined data at $\phi = 0.46$ exhibit slightly subdiffusive behavior in-line with data in Fig. 3.9(c),(d). While the data in Fig. 3.9(c) appear to be in the process of recovering diffusive behavior at large Δt, data in (d) remain strongly subdiffusive at similar times, implying that the time scales necessary to recover diffusive behavior increase with η_x.
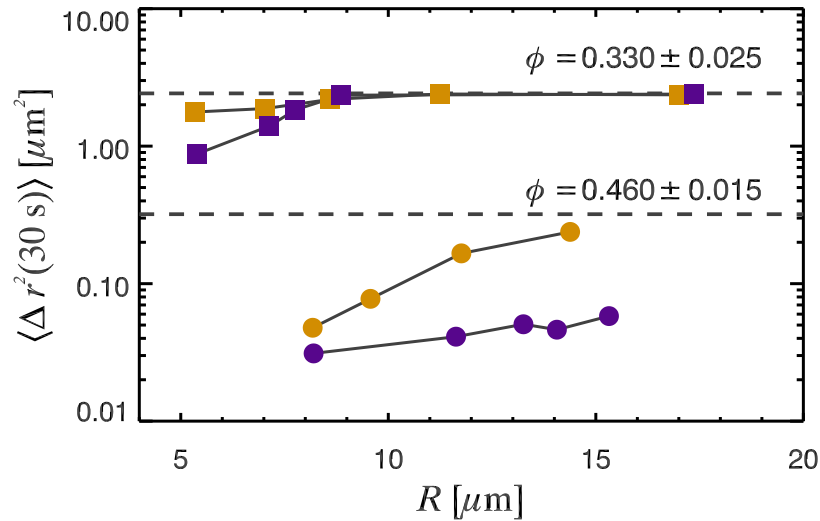
Figure 3.10: Mobility [measured as $\langle \Delta r^2(t = 30\text{s}) \rangle$] versus droplet size for $\phi = 0.330 \pm 0.025$ (squares) and $\phi = 0.460 \pm 0.015$ (circles). Here, color indicates the viscosity of the external phase with $\eta_x = 5.7$ mPa·s (gold) and $\eta_x = 15.2$ mPa·s (navy), and the dashed line shows $\langle \Delta r^2(30\text{ s}) \rangle$ measured in a bulk, unconfined sample.

To see more clearly how confinement effects vary with droplet size R and boundary conditions, we show in Fig. 3.10 values of $\langle \Delta r^2(t = 30\text{s}) \rangle$ from Fig. 3.9 as a function of

droplet radius. In Fig. 3.10 for $\phi = 0.330 \pm 0.025$, we find no difference in $\langle \Delta r^2(30\text{s}) \rangle$ between the two external phases for systems confined $R \gtrsim 9$ μm, indicating that dynamics are independent of both R and η_x at these length scales. The onset of confinement effects occurs at $R \approx 9$ μm for systems in both external phases. However for larger η_x, the decrease in dynamics is more significant as R decreases, dropping by more than half of its value over a change from $R \approx 9$ μm to $R \approx 5$ μm.

For the cases $\phi = 0.460 \pm 0.015$ in Fig. 3.10, one again sees that dynamics decrease with decreasing R. While this trend is qualitatively the same for both η_x, we find a significant quantitative difference between the two. In the largest droplets here, the difference between $\langle \Delta r^2(30\text{s}) \rangle$ is more than a factor of 4 between the two external phases. Due to experimental limitations, larger droplets could not be successfully studied in this case, hence we cannot say at what value of R dynamics between droplets in the two external phases become indistinguishable. Presumably for large enough R, the two curves will merge, as in does data at lower ϕ, with dynamics becoming unaffected by confinement. Previous work in a 1D confined system implies that confinement effects begin at a length scale of ≈ 50 μm for similar ϕ, which would correspond in our systems to droplets with $R \approx 25$ μm [131]. In the smallest droplets, the ratio of $\langle \Delta r^2(30\text{s}) \rangle$ between systems exposed to the two external phases drops to a factor of ≈ 1.5. Again, due to experimental limitations, smaller droplets could not be successfully studied, so we cannot determine how dynamics differ between external phases for these length scales. The data used in Fig. 3.10, including ϕ and n_S/n_L for the different droplets, are listed in Tabs. 3.2 and 3.3.

3.3.2 Structure within Droplets

We turn our attention to examining particle-structure within the droplets, which would arguably be the most intuitive cause of differences in dynamics seen in Fig 3.10. The

Table 3.2: Results of Confinement Experiments: $\eta_x = 5.7$ mPas

R [μm]	n_S/n_L	ϕ	$\langle \Delta r^2 (30\text{s}) \rangle$ [μm^2]
5.35	0.97	0.331	3.47
7.03	0.98	0.336	3.39
8.60	0.78	0.318	3.61
11.24	1.00	0.327	3.83
17.00	0.81	0.327	3.65
8.18	1.21	0.459	0.048
9.57	0.90	0.455	0.078
11.76	1.31	0.457	0.166
14.40	1.08	0.458	0.238

Table 3.3: Results of Confinement Experiments: $\eta_x = 15.2$ mPas

R [μm]	n_S/n_L	ϕ	$\langle \Delta r^2 (30\text{s}) \rangle$ [μm^2]
5.40	0.89	0.327	1.80
7.13	0.76	0.338	2.43
7.76	0.87	0.345	3.13
8.86	0.75	0.315	3.88
17.37	0.97	0.334	3.78
8.20	1.00	0.466	0.031
11.63	1.11	0.470	0.041
13.26	1.54	0.455	0.051
14.06	1.04	0.459	0.046
15.32	1.25	0.463	0.058

structure of fluids is often described with the pair correlation function (or radial distribution funtion), $g(r)$. Essentially, $g(r)$ expresses the likelihood of finding a particle at a distance r from some test particle, relative to the average density of the sample. Shown in Figs. 3.11 and 3.12 are calculated $g(r)$ curves comparing the internal particle-structures for droplets of similar volume fraction and radii in the two different external phases.

In Fig. 3.11, $g(r)$ is shown for data sets with both external viscosities where $\phi = 0.330 \pm 0.025$. The location of the peak, r_p, in the pair correlation function expresses the average nearest-neighbor distance between particles. For these data, the peak occurs at $r_p \approx 2.43$ μm. This is larger than the average particle diameter $2a = 2.16$ μm and indicates that the particles within the droplets are slightly charged. However, as shown in the inset, r_p fluctuates only slightly (by ≈ 25 nm) between droplets of different sizes and droplets with different external phases. Furthermore, the fluctuations exhibit no obvious trend with R or η_x. Thus, we conclude that the variations in $\langle \Delta r^2(30\text{s}) \rangle$ for these data are not due to differences in particle electrostatic interactions inside the droplets.

The shapes of the curves in Fig. 3.11 are also very similar. In addition to the primary peaks at r_p, there are small secondary peaks at ≈ 4.5 μm, which correspond to second-nearest neighbor shells. Beyond these points, $g(r)$ flattens for all curves, indicating that there are no significant long range structural correlations. These $g(r)$ demonstrate for these data that internal particle-structures within these droplets at $\phi = 0.330 \pm 0.025$ are very similar and likely not the cause for the differences seen in Fig. 3.10.

Fig. 3.12 shows $g(r)$ for data with $\phi = 0.460 \pm 0.015$, again for both external phases. Here, $r_p \approx 2.36$ μm, which is smaller than seen for $\phi = 0.330 \pm 0.025$, but is consistent with an overall in ϕ. Between droplets of different radii and in different external phases, there is no significant variation in r_p. As was the case for the lower ϕ data, electrostatic interactions are most likely not the cause of the differences in $\langle \Delta r^2(30\text{s}) \rangle$.
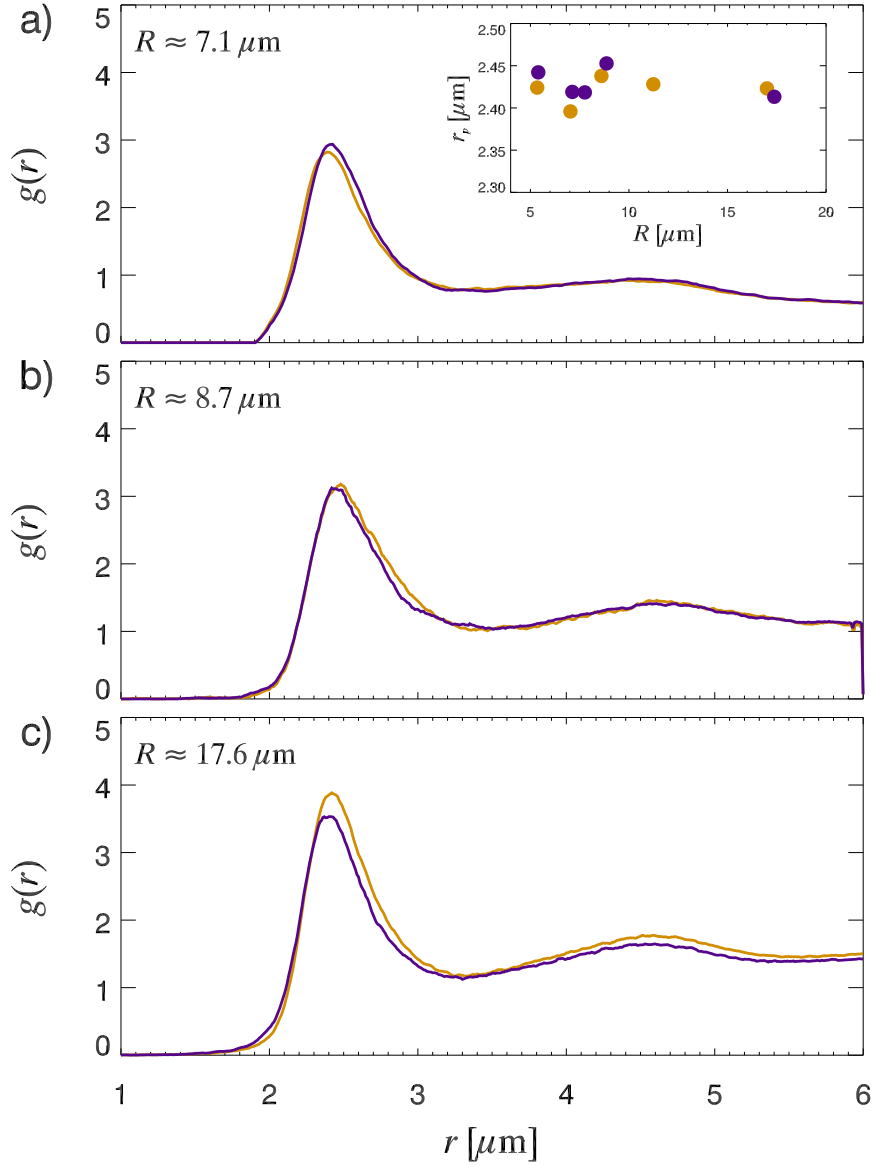
Figure 3.11: Pair correlation functions for droplets with $\phi = 0.330 \pm 0.025$, with $\eta_x = 5.7$ mPa·s (gold) and $\eta_x = 15.2$ mPa·s (navy). Approximate droplet radii are given in the upper left of each panel. The inset to (a) shows the location of the peak, r_p, in $g(r)$ for droplets of different radii.

These $g(r)$ show secondary peaks at ≈ 4 μm, but are here broader and more pronounced than for data with lower ϕ. This is consistent with an increase in ϕ for a binary sample. While these curves do exhibit slight differences between the different external
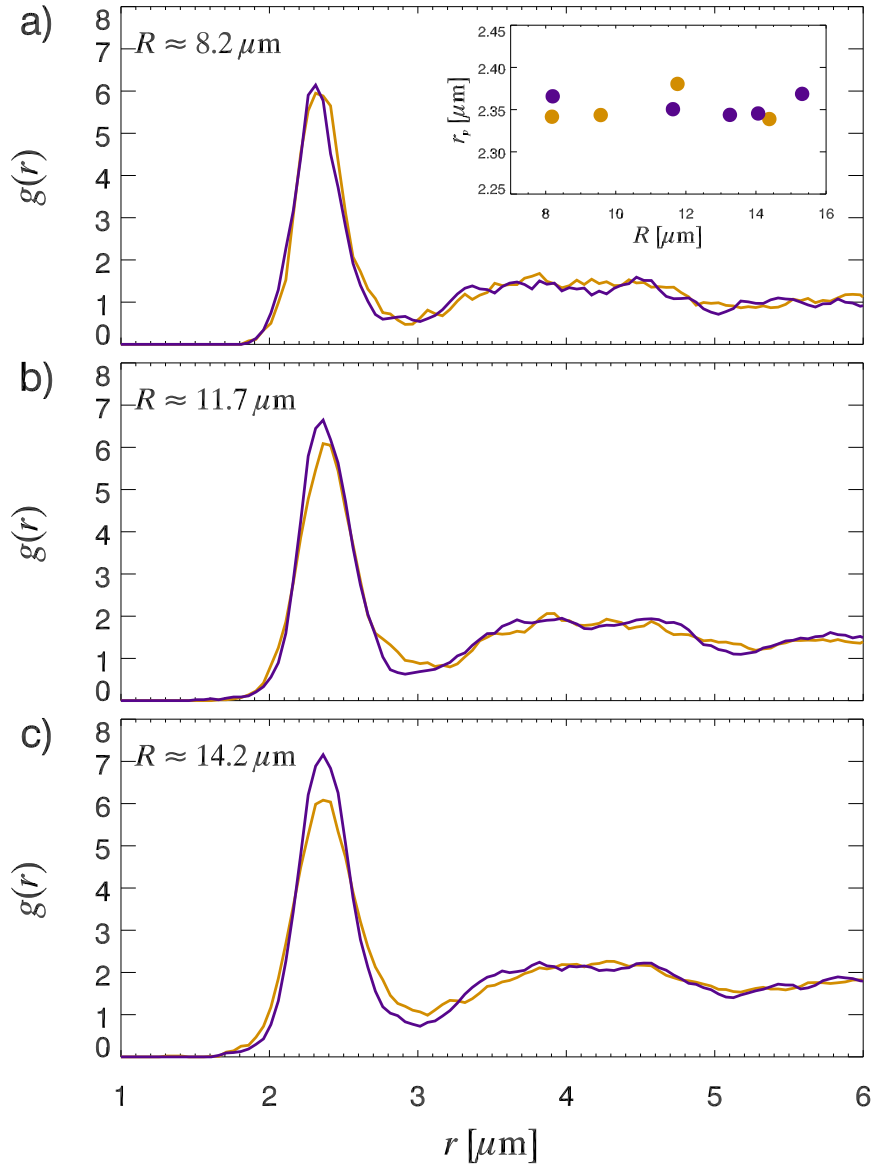
Figure 3.12: Pair correlation functions for droplets with $\phi = 0.460 \pm 0.015$, with $\eta_x = 5.7$ mPa·s (gold) and $\eta_x = 15.2$ mPa·s (navy). Approximate droplet radii are given in the upper left of each panel. The inset to (a) shows the location of the peak, r_p, in $g(r)$ for droplets of different radii.

phases, these variations are attributable to small differences in ϕ and number ratio. Overall, $g(r)$ for these data show that particle-structure in droplets at the higher ϕ studied are extremely similar and likely not the source of differences in dynamics.

3.3.3 Particle Mobility and Distance from Interface

To investigate how a particle's motion is affected by its distance s from the boundary, we calculate a local average particle mobility $\langle\Delta r(s)\rangle$, defined by

$$\langle\Delta r(s)\rangle = \frac{\int\limits_{s-\delta s}^{s+\delta s} |\Delta\vec{r}(s)|\, n(s)ds}{\int\limits_{s-\delta s}^{s+\delta s} n(s)ds}, \tag{3.8}$$

where $n(s)$ is the particle number density and $|\Delta\vec{r}|$ is the magnitude of a particle's vector displacement. For consistency with previous results, we calculate $\langle\Delta r(s)\rangle$ at a lag time of $\Delta t = 30$ s. As with data in Fig. 3.10, no qualitative difference is found using different Δt. A value of $\delta s = 0.5$ μm is used for all data sets and is sufficiently small to reveal significant qualitative and quantitative trends, as will be discussed shortly. Thus, $\langle\Delta r\rangle$ is a number-weighted average of the size of particle displacements over a radial bin with a width of ≈ 1 large particle radius.

In Fig. 3.13, we show $\langle\Delta r(s)\rangle$ for droplets with $\phi = 0.330 \pm 0.025$ for the lower (a) and higher (b) external viscosities. These two graphs are strikingly different. Curves in Fig. 3.13(a) show similar trends with s: particle motions are slightly slowed nearer to the boundary than farther away, i.e. there exists a dynamical gradient as a function of s. There are slight offsets for these curves which decrease with decreasing R. Here, we note two things. First, the oscillations seen in these curves are out of phase with particle layers, such as those shown in Fig. 3.6. The increase in mobility between layers arises from packing constraints and layering described in Sec. 3.2.6. Second, large deviations at
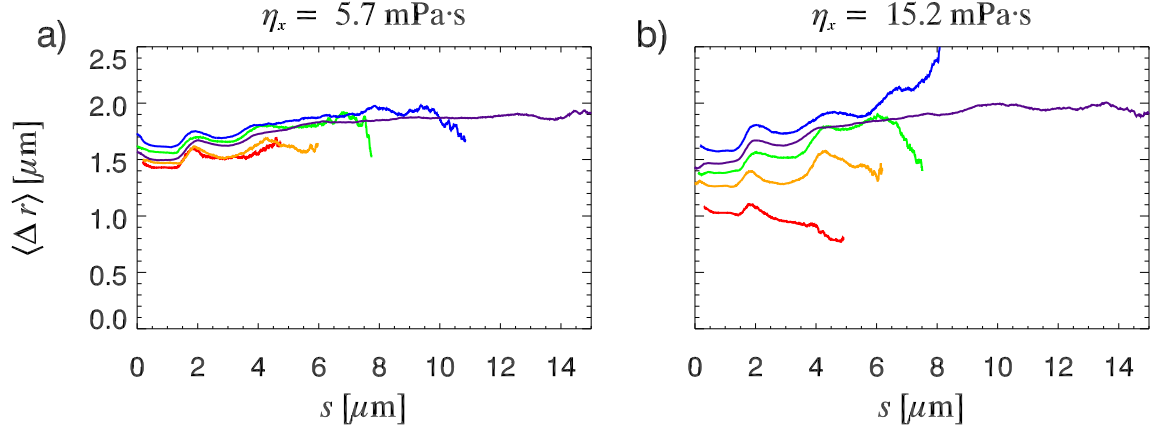
Figure 3.13: Particle mobility as a function of distance from the interface. (a) $\eta_x = 5.7$ mPa·s. (b) $\eta_x = 15.2$ mPa·s. For all droplets, $\phi = 0.330 \pm 0.025$. In general, droplet size increases from red to blue.

larger s are due to low statistics in the centers of the droplets. Mobilities in Fig. 3.13(b) are again self-similar, but show much stronger offsets as R decreases. The differences in dynamical gradients appear to be the cause of the decrease in $\langle \Delta r^2 \rangle$ shown in Fig. 3.10 for $\phi = 0.330 \pm 0.025$.

Shown in Fig. 3.14 are $\langle \Delta r(s) \rangle$ for droplets with $\phi = 0.460 \pm 0.015$. Here, we find for both η_x that decreasing droplet size offsets the mobility toward lower values, though the offsets are much more pronounced when η_x is smaller. Also, data for smaller η_x show well-defined dynamical gradients, whereas when η_x is larger, the mobilities appear approximately constant throughout the droplet. As with data at lower ϕ, the differences in $\langle \Delta r(s) \rangle$ are at the source of the decrease in dynamics with decreasing droplet size, shown in Fig. 3.10.

We are also able to observe how directional motions within the droplets vary with s. To do so, we decompose $\langle \Delta r \rangle$ into components perpendicular and parallel to the interface. Radial (perpendicular) and tangential (parallel) mobilities, $\langle \Delta r_{\perp}(s) \rangle$ and $\langle \Delta r_{||}(s) \rangle$, respectively are defined according to
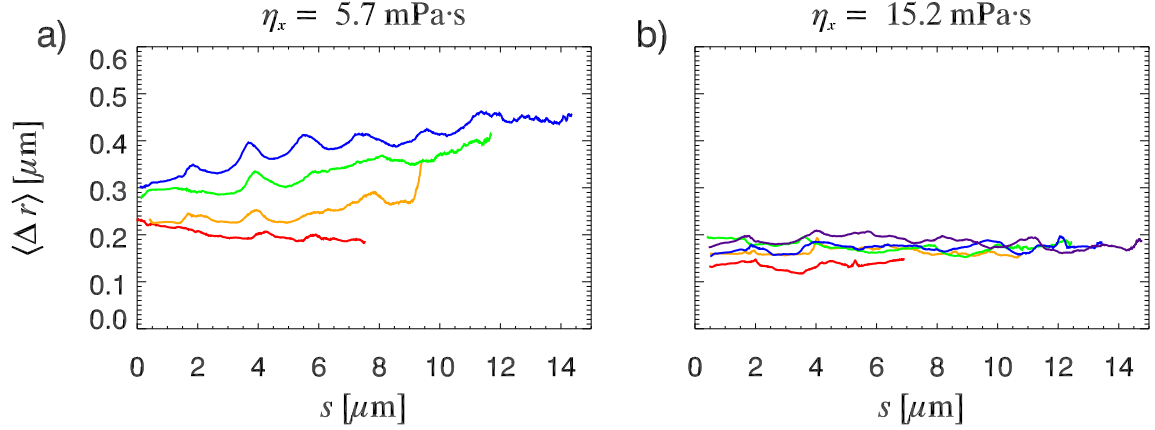
Figure 3.14: Particle mobility as a function of distance from the interface. (a) $\eta_x = 5.7$ mPa·s. (b) $\eta_x = 15.2$ mPa·s. For all droplets, $\phi = 0.460 \pm 0.015$. In general, droplet size increases from red to blue.

$$\langle \Delta r_\perp(s) \rangle = \frac{\int\limits_{s-\delta s}^{s+\delta s} |\Delta \vec{r}(s) \cdot \hat{r}| \, n(s) ds}{\int\limits_{s-\delta s}^{s+\delta s} n(s) ds}, \tag{3.9}$$

$$\langle \Delta r_{||}(s) \rangle = \frac{\int\limits_{s-\delta s}^{s+\delta s} |\Delta \vec{r}(s) \cdot \hat{\theta}| \, n(s) ds}{\int\limits_{s-\delta s}^{s+\delta s} n(s) ds}. \tag{3.10}$$

Shown in Fig. 3.15 are components of mobility for droplets with $\phi = 0.330 \pm 0.025$ in both external phases. We find that radial components behave similarly between the phases, with both exhibiting out-of-phase oscillations related to layering, but with offsets strongly affected by R occurring with larger η_x. Parallel components for these ϕ are more distinct between phases, but also show similarities. In both η_x, parallel mobility appears fastest for $s \lesssim 2$ μm. Mobility decreases sharply at $s \approx 2$ μm and essentially plateaus for larger s. For decreasing R in both η_x, we observe decreases in the plateau values as well as the mobilities near the boundary, though for larger η_x the decrease is again stronger.

Mobility components for droplets with $\phi = 0.460 \pm 0.015$ are shown in Fig. 3.16. In
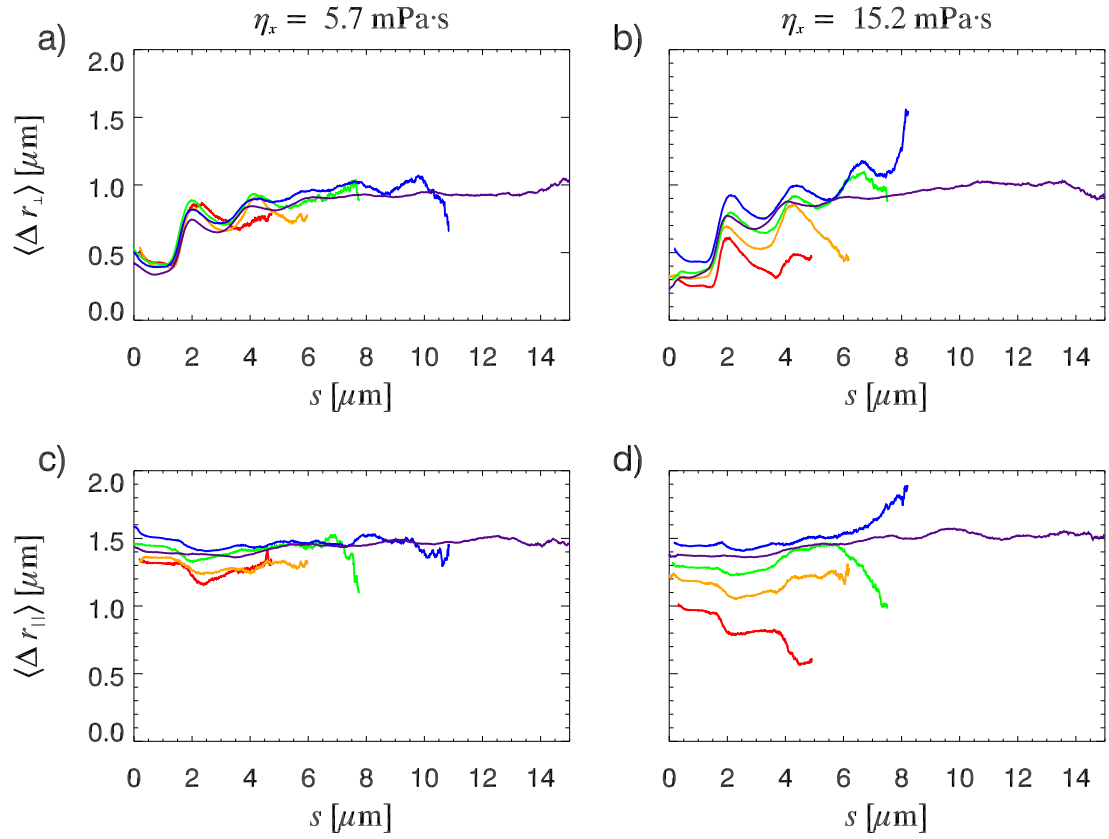
Figure 3.15: Radial (a),(b) and tangential (c),(d) components of particle mobility as a function of distance from the droplet interface for $\phi = 0.330 \pm 0.025$. Panels (a),(c) are for droplets with $\eta_x = 5.7$ mPa·s and (b),(d) for $\eta_x = 15.2$ mPa·s. In general for each panel, droplet size increases from red to blue.
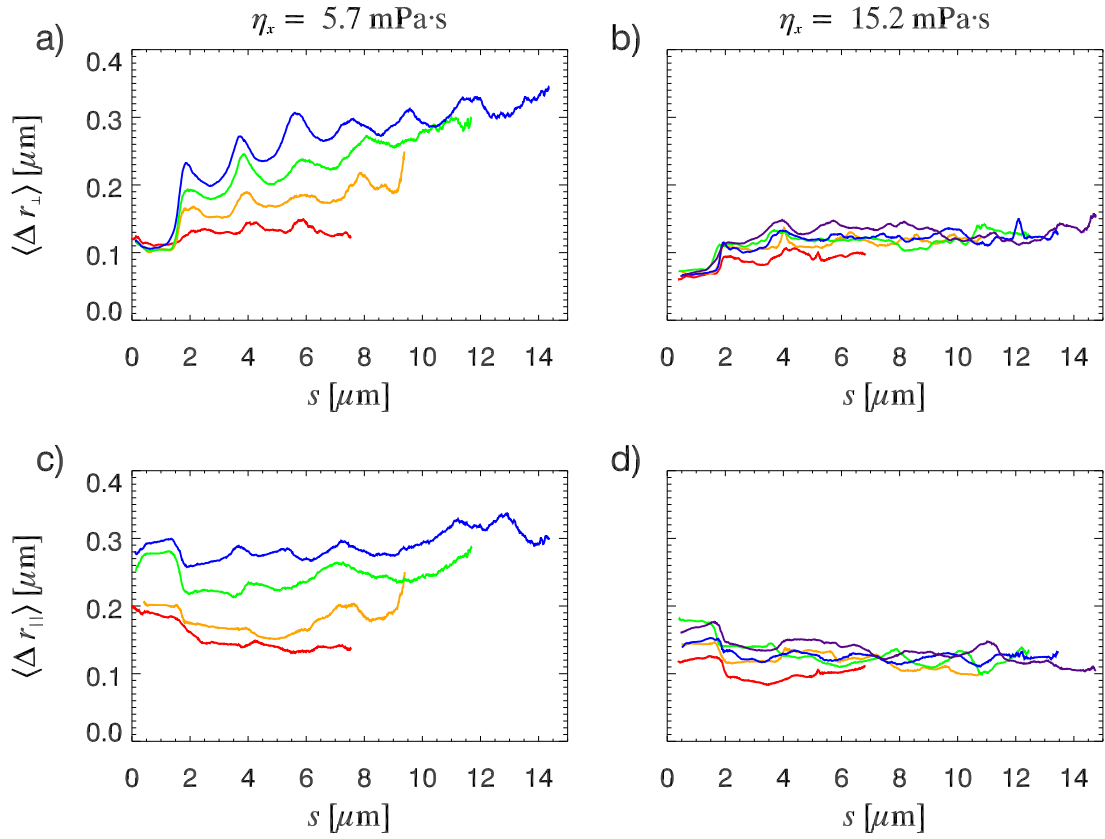
Figure 3.16: Radial (a),(b) and tangential (c),(d) components of particle mobility as a function of distance from ther droplet interface for $\phi = 0.460 \pm 0.015$. Panels (a),(c) are for droplets with $\eta_x = 5.7$ mPa·s and (b),(d) for $\eta_x = 15.2$ mPa·s. In general for each panel, droplet size increases from red to blue.

panel (a), we find that $\langle \Delta r_\perp \rangle$ shows dramatic dependence on s and R. Here, particle motions are slowest for $s \lesssim 2 \ \mu$m, and grow larger as the center of the droplet is approached. As R decreases, mobility curves flatten significantly, though even for the smallest R, a gradient in dynamics can be seen. Indeed, the same trend is found for the droplets in higher viscosity external phase, shown in panel (b), though the magnitude of the mobility is everywhere smaller. The tangential mobilities shown in Fig. 3.16(c,d) are again quite distinct, but demonstrate similar trends as with droplets with lower ϕ. Motions are again the fastest for $s \lesssim 2 \ \mu$m and seem to plateau for larger values of s. For the smaller η_x, $\langle \Delta r_{||} \rangle$ shifts strongly to smaller values as R decreases. The same trend is apparent for the larger η_x, though as with the radial component, the mobility is everywhere smaller.

3.4   Ansatz for Radial Mobility

Because the radial components of mobility in Fig. 3.16(a,b) display the most interesting behavior as a function of s and R, we now focus our attention on better understanding the behavior of the radial mobilities for both ϕ studied. To do so, we apply an ansatz to describe the s-dependence of $\langle \Delta r_\perp \rangle$,

$$\langle \Delta r_\perp(s) \rangle = A \left[1 - \beta \exp \left(-s/\lambda \right) \right]. \tag{3.11}$$

The above equation is a simple exponential decay, modified from a form introduced by Scheidler *et al.* for describing the dependence of relaxation times in simulations of supercooled liquids confined in 1D [136]. As can be seen in Fig. 3.17, a fit of the type given in Eqn. (3.11) roughly captures of the behavior of $\langle \Delta r_\perp \rangle$, though it is clearly imperfect. Mobilities are only well-fit at the smallest values of s. Oscillations in the data are not accounted for with Eqn. (3.11) and are very likely contributing error to the fit. We are

unaware of a more appropriate fitting form. Furthermore, if one were available, the signal-to-noise ratio apparent in Fig. 3.16 is likely too large for this type of analysis to be much improved. We thus proceed with analysis of $\langle \Delta r_\perp \rangle$ in terms of Eqn. (3.11) with the goal of only approximately capturing the behavior of radial mobility.
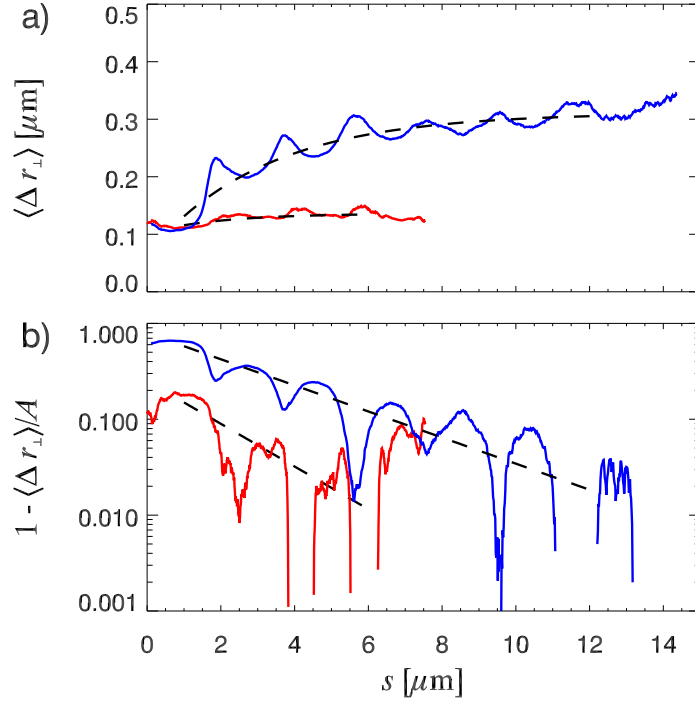
Figure 3.17: Example fits of radial mobility to Eqn. (3.11) for two droplets. The blue line is for $R = 14.40$ μm, and the red for $R = 8.18$ μm. In these examples, $\eta_x = 5.7$ mPa·s and $\phi = 0.460 \pm 0.015$. a) Double linear plot of $\langle \Delta r_\perp \rangle$ with fits. b) Log-linear plots with fits.

The results of fitting $\langle \Delta r_\perp \rangle$ for both ϕ are given in Fig. 3.18. Here, we plot the obtained parameters for each data set as a function of droplet radius. Inspection of Eqn. (3.11) shows that the parameter A is the value of $\langle \Delta r_\perp \rangle$ extrapolated to $s \to \infty$, i.e. for particles very far from the boundary. In Fig. 3.18(a,b), we find that A behaves in the same qualitative way as $\langle \Delta r^2 \rangle$ shown in Fig. 3.10. For $R \gtrsim 9$ μm in panel (a), values of A approximately collapse and show no variation with R. For $R \lesssim 9$ μm, however, A acquires a dependence on η_x. Thus at this ϕ, for confinement length scales of $R \lesssim 9$ μm, the sample

is aware of a variation in the boundary conditions. At the larger ϕ in panel (b), we again find a dependence on η_x and R, which implies that droplet radii are already below the confinement length scale relevant for this ϕ.
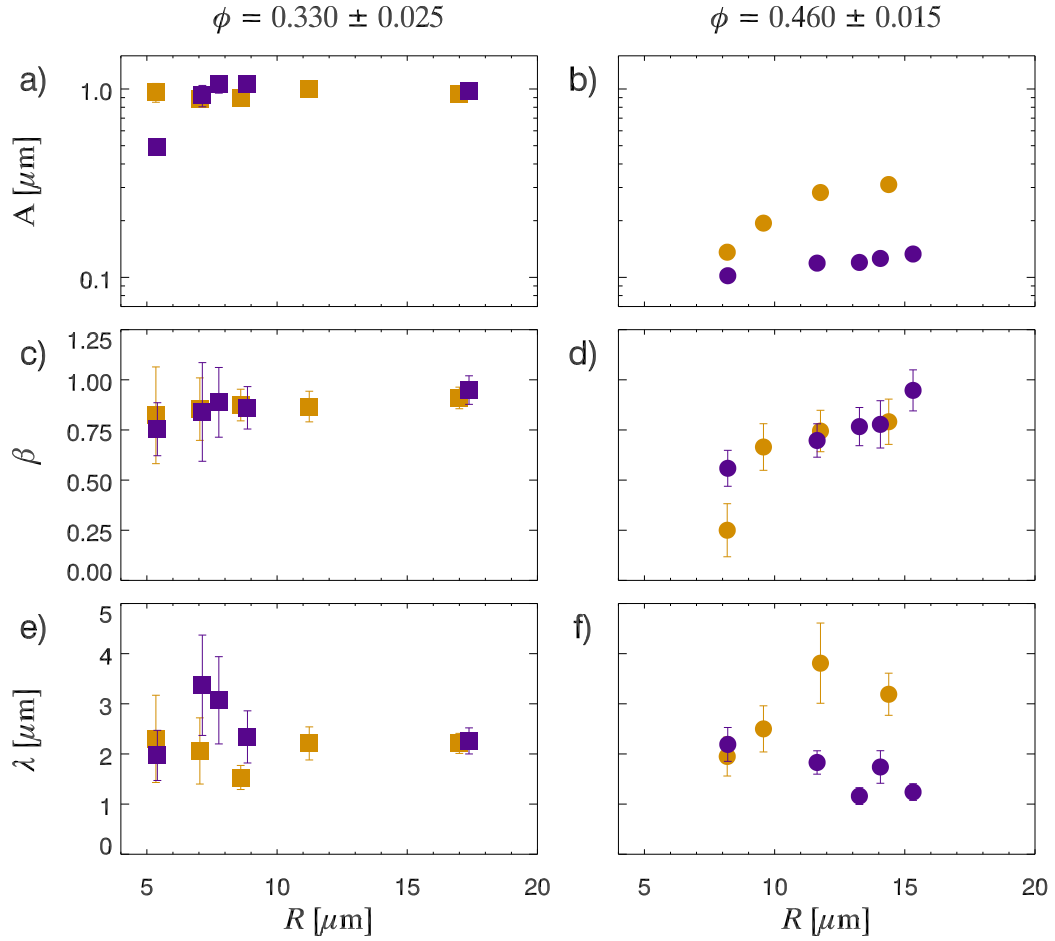
Figure 3.18: Parameters resulting from fits of radial mobility to Eqn. (3.11) for $\eta_x = 5.7$mPa·s (gold symbols) and $\eta_x = 15.2$mPa·s (navy symbols). Left panels: $\phi = 0.330 \pm 0.025$. Right panels: $\phi = 0.460 \pm 0.015$.

Perhaps the most interesting of the fitting parameters is β, which from Eqn. (3.11) can be considered the amplitude of the exponential decay. Shown in Fig. 3.18(c,d) are β for data sets at both ϕ. Intriguingly, β does not appear to depend on η_x as data from both external phases appear to collapse onto the same curve for a given ϕ (except perhaps at

the smallest R in panel (d)). Along with ϕ, there is also a clear dependence on R. In panel (c) for the lower ϕ, β is roughly constant, with perhaps a slight downturn near $R \approx 9$ μm. For the larger ϕ, there is a clear decrease in β as R decreases. Thus, β seems to capture only the effect of finite system size. It is possible that if larger droplets could be studied, one could observe a plateau in the value of β for $\phi = 0.460 \pm 0.015$, in the same way as β plateaus for $\phi = 0.330 \pm 0.025$.

The parameter λ in Eqn. (3.11) characterizes the length scale over which interactions with the confining boundary decay and are shown in Fig. 3.18(e,f). Here we note there is significant scatter and uncertainty in our measurements of λ for both η_x and for both ϕ studied. Given this degree of uncertainty, the interpretation of how such a length scale is affected either by confinement or by the external phase is somewhat inconclusive. There is perhaps a decrease in λ with growing R for higher η_x relative to lower η_x, but this conclusion is tenuous. Overall, however, λ falls within a range $0.5a_L \lesssim \lambda \lesssim 2a_L$, which is on par with length scales typically measured in dense colloidal suspensions [137, 138].

3.5   Discussion and Conclusions

We have confined colloidal suspensions within emulsion droplets to probe how particle dynamics are affected by the material properties of the external medium. Our experiments have shown that, as in systems of glassy polymers and supercooled molecular liquids, the response of a dense colloidal suspension to confinement depends in a sensitive way on properties of the medium to which it is confined. For liquid-like suspensions, we find that above a droplet radius of $R \approx 9$ μm, internal particle dynamics are indistinguishable between systems with external phases of $\eta_x = 5.7$ mPa·s and $\eta_x = 15.2$ mPa·s. For droplets with smaller R, this is not the case. There is a clear distinction in dynamics between the

two external phases, with more rapid dynamics occurring in systems with smaller η_x. In both η_x, a decrease in system size corresponds to a decrease in dynamics, though the rate of the decrease with R depends on η_x.

For suspensions in the supercooled regime, we find a significant difference in dynamics for droplets with $R \lesssim 15.3$ μm, which is the largest droplet size that could be successfully studied. The larger η_x is associated with strongly decreased particle motions relative to lower η_x. As with suspensions at lower ϕ, a decrease in the system size corresponds to a decrease in overall particle dynamics, again with a rate that depends on η_x.

The differences in dynamics for the samples studied does not appear to be due to structural changes or variations in electrical interactions between samples: for droplets with similar R and ϕ, the internal particle structure, as measured by $g(r)$, are indistinguishable as shown in Figs. 3.11 and 3.12.

We have directly observed that the magnitude of a particle's motions depends on its distance from the confining boundary. Indeed, the contrast in average dynamics described above arises due to differences in these gradients. We find that decreasing the system size generally results in smaller particle displacements, however the rate at which dynamics decrease is a function of η_x. We applied the ansatz in Eqn. (3.11) to the radial components of particle mobility, as these showed the most intriguing trends. While Eqn. (3.11) captures some of the qualitative aspects of $\langle \Delta r_\perp(s) \rangle$, it is likely not the most appropriate functional form with which to interpret our data. This could be true for two reasons. First, when used previously in [136], the ansatz was applied to simulations of supercooled systems confined in 1D, whereas our data is 3D. It's entirely likely that the boundary effects combine in some nontrivial way for systems confined in 3D. Second, Scheidler *et al.* measured relaxation times instead of mobility. Relaxation times in colloids are often associated with time scales
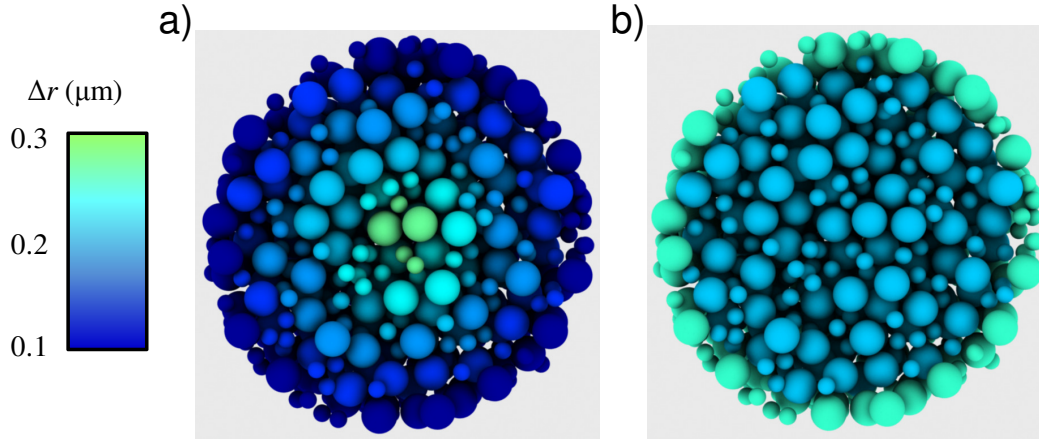
Figure 3.19: Rendering of particles in a colloid-filled emulsion droplet color-coded by a) radial mobility and b) tangential mobility. For this data, $R = 11.76$ μm, $\phi = 0.460 \pm 0.015$, and $\eta_x = 5.7$ mPa·s.

needed for dynamics to recover diffusive behavior [137]. For lower ϕ data, the ansatz may fail because the system is in a liquid-like state, whereas for higher ϕ data, the recovery of diffusivity could not be observed over the experimental time window (see Fig. 3.9). However, whether or not the mobility gradient is of exponential or some other form, the existence and behavior of dynamical gradients is quite clear in Figs. 3.13 and 3.14.

Shown in Fig. 3.19 are computer renderings from real particle coordinates in one of our data sets. Here, small and large particles are visible and are color-coded based on their mobility over a duration of 30 s. Panel (a) shows the radial mobility of particles, while panel (b) shows the tangential mobility. While a complete quantitative picture of the observed mobility gradients could not be found, Fig. 3.19 shows qualitatively the behavior of all samples studied. Radially, particles are slowest near the boundary, but the magnitude of their motions increase toward the center of the droplet. Tangentially, particles are fastest near the boundary, with a sharp decrease in mobility after approximately one large particle radius. The direct observation of a dynamical gradient in our systems, we believe, provides strong evidence for the existence of such gradients in confined polymeric and molecular

glassformers.

Chapter 4

A Free Energy Landscape for Cage Breaking of Three Hard Disks

4.1 Introduction

The concepts of potential and free energy landscapes for condensed matter systems are appealing ones [23, 139, 140], and their use to understand the glass transitions in various materials has received considerable attention [141–150]. Each spatial configuration of a system can be assigned a potential energy based on how individual elements interact. By incorporating other thermodynamic variables, such as entropy, one can associate free energies with all points in phase space, which then constitute a free energy surface or "landscape". The temporal evolution of a system can be thought of as an exploration of various topographical features on the energy surface, with relaxation events understood as motions between adjacent energy minima [140, 151–153]. As the glass transition is approached, the system finds itself in progressively deeper local minima on the landscape until thermal energy is unable to excite the system over a barrier and into a lower energy

state.

A complete energy landscape accounts for all degrees of freedom within a system, each of which contributes two dimensions to the phase space (position, momentum). For many body systems then, the complete energy landscape can be extraordinarily complex. A central problem in using the energy landscape approach is minimizing the number of "reaction coordinates" (likewise "order parameters") while still adequately describing the surface [153–161]. Studies often choose one or two coordinates of interest and examine how the system evolves on representative 1D or 2D landscapes, though in some cases such low dimensional projections may introduce artifacts or occlude important features of the landscape [158–160].

These complexities aside, the typical picture of an energy landscape is one of a surface containing hills and valleys. However, for the case of a purely hard core potential, such as that of hard disks or hard spheres, this picture is incorrect. In a hard disk or hard sphere system, the Helmholtz free energy is governed entirely by entropy,

$$F = -TS, \tag{4.1}$$

to within an additive constant [18, 19]. All allowable configurations have identically zero potential energy and are therefore equiprobable. Thus, in terms of the total configuration space, the energy landscape is completely flat. Upon projection into a lower dimensional space, however, hills and valleys related to entropic minima and maxima can arise [142, 143, 149, 162–164]. In this chapter, we will introduce a simple model system in order to better understand how dynamics in glassy systems with hard core potentials relate to an underlying free energy landscape.
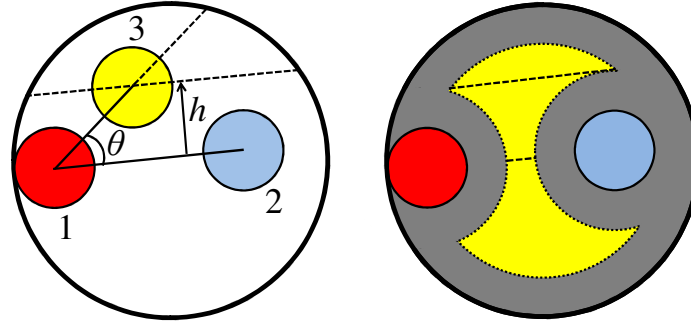
Figure 4.1: (a). Three distinguishable hard disks are confined within a circular corral of fixed size. The variables h and θ are macrostate variables, to be defined later. Dashed lines are lines of constant h and θ. (b). A 2D slice through the 6D configuration space with constant $(\vec{r}_1, \vec{r}_2)$. The yellow region is accessible to the center of disk 3, whereas the dark gray region is energetically forbidden. Upper and lower dashed lines represent possible system macrostates at fixed h, where the length of the line determines the entropy of the state.

4.2 Model System

Consider a system of $N = 3$ distinguishable hard disks confined within a hard-walled circular corral, as illustrated in Fig. 4.1(a). The configuration space of this system is six-dimensional (6D) and is completely described by all allowable combinations of $(\vec{r}_1, \vec{r}_2, \vec{r}_3)$. However, as stated previously, the energy landscape is flat because each configuration is as probable as any other. Now, we consider a 2D slice though the landscape examining all configurations of $\vec{r}_3$ while $(\vec{r}_1, \vec{r}_2)$ are held at constant values, such as shown in Fig. 4.1(b). All allowed configurations are again equiprobable and are indicated by the yellow region. The landscape in this scenario remains flat. However, there are more configurations where disk 3 exists along the upper dashed line than on the line between disks 1 and 2. If we interpret these two lines as macrostates of the system, the entropy of the upper line is larger and therefore the free energy in Eqn. (4.1) is lower. By considering all macrostates, that is all lines parallel to those in Fig. 4.1(b), we obtain a 1D representative landscape with variations in free energy.

We can immediately relate these ideas to a dynamic version of the system in Fig. 4.1(a), where all disks wander around the corral by means of Brownian motion. Here, we may ignore degrees of freedom associated with momentum and focus only on the six spatial components. As the system explores its 6D configuration space, disk 3 spends more time in configurations with high entropy on the 1D landscape, such as along the upper dashed line in Fig. 4.1(b). To transition into the lower cusped region, it must pass through an entropic bottleneck. Of course, this behavior is not unique to disk 3 but applies to all disks in our system. Hence, the transition of any single disk corresponds to the entire system crossing a free energy barrier.

Prior to a barrier crossing event, the motion of each disk is localized by the presence of other disks and the wall. As with individual molecules in dense liquids or particles in a dense colloidal suspension, the disks can then be described as "caged" [102, 112–114, 149, 165–171]. Deviations from strongly localized behavior, such as those during a crossing event, are considered "cage breaking" [136, 168, 169, 172–176]. One can consider both caging and cage breaking from the point of view of an energy landscape, where caging is the motion of the system around some local minimum and cage breaking is the relaxation over an energy barrier [164, 177–182].

In the spirit of [162, 163, 171, 172, 183], we introduce the minimal model system illustrated in Fig. 4.1(a) in order to explore the relationship between caging and the free energy landscape of a system with hard core potentials. Here, the free energy landscape can be calculated by a direct enumeration of states, while a cage breaking event can be simply described as one disk passing between the other two. One can imagine for a very large corral, the motions of any disk would only rarely be influenced by the other disks or the boundary, and so dynamics would be similar to those in a dilute colloidal suspension. However, this picture changes for smaller corral sizes, or similarly higher packing fractions,

where interactions between the disks or with the wall are more frequent and dynamically restrictive. Though somewhat contrived, these purely geometric constraints are of similar character to those encountered by real particles in a densely packed system, such as colloidal supercooled liquids or glasses [184–187].

4.3 Simulation Details

Three hard-disks of radius $r = d/2 = 1$ are confined to a hard-walled, circular corral of radius $R_C = 3 + \epsilon$. Choosing $r = 1$, we note that all lengths are by definition in units of a particle radius. The minimum system size that permits cage breaking occurs at $\epsilon = 0$, where the three particles exactly fit across the diameter of the corral. During each simulational run, we fix the value of ϵ and allow particles to execute Brownian motion, described below. Each run consists of 10^8 Monte Carlo steps (mcs) for a particular value of ϵ, during which each particle has the opportunity to make a displacement. Values of ϵ are chosen within a range of $\epsilon \in [0.037, 10.0]$.

To simulate Brownian dynamics, displacements for each particle at every time step in the $x-$ and $y-$directions are sampled from a Gaussian distribution with variance $\sigma^2 = 2D = 1 \times 10^{-3}$. A displacement is accepted if it does not result in particle-particle or particle-wall overlap, otherwise the offending particle remains fixed for that time step. This results in an RMS displacement of approximately $\approx 2\%$ of a particle diameter at each time step. The value of D, and therefore the temperature, is constant across all simulations. The order in which particles are sampled is randomized at each time step and satisfies detailed balance [188]. For the stated value of D, the fraction of accepted displacements range from 0.954 at $\epsilon = 0.037$ to 0.997 at $\epsilon = 10.0$.
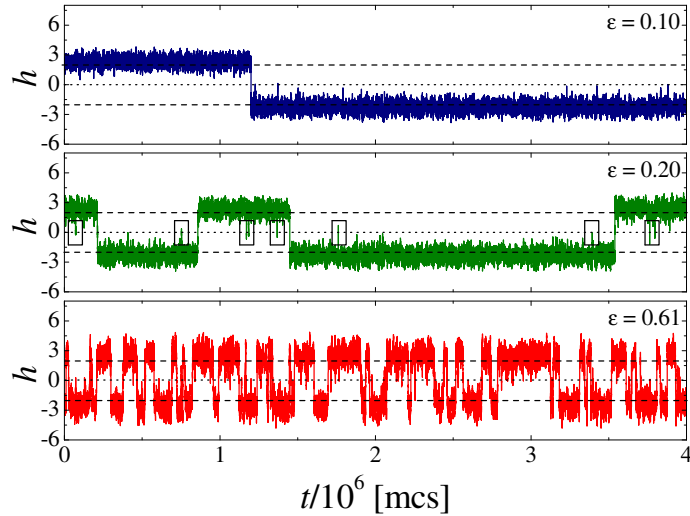
Figure 4.2: Trajectories through h-space for (top-bottom): $\epsilon = 0.10$, 0.20, and 0.61. Dotted lines pass through $h = 0$ and dashed lines pass through $h = \pm 2$. The length of time between crossing events is clearly a sensitive function of ϵ. Small fluctuations about $h = 0$ (such as those in the boxed regions for $\epsilon = 0.20$) are not considered as true cage breaking events.

4.4 Dynamics in 1D

To study the dynamics of this system, we first simplify the 6D configuration space by projecting down to one dimension. We define a macrostate variable h, shown in Fig. 4.1(a), as the distance of the center of disk 3 normal to a line segment drawn from the center of disk 1 to that of disk 2. Put another way, if a line drawn from the center of disk 1 to that of disk 2 defines the positive x-axis of a coordinate system, h is given by the y-coordinate of disk 3. Therefore, h can take positive or negative values, which from geometry are limited to the range $[-h_{\max}, h_{\max}]$, where $h_{\max} = 2 + \epsilon + \sqrt{3 + 4\epsilon + \epsilon^2}$. This definition allows for a cage rearrangement to be described as the system passing through $h = 0$, regardless of which particle passes between the others. Finally, we note that this definition maps all rotationally symmetric states to the same value of h.

Shown in Fig. 4.2 are trajectories in h-space for three values of ϵ. As ϵ increases from top to bottom, the length of time between cage breaking events decreases, as one
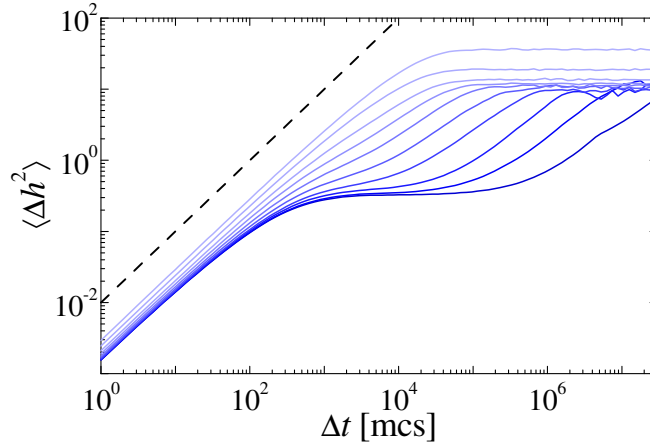
Figure 4.3: Mean-square displacement in h-space for systems with (bottom to top, dark blue to light blue) $\epsilon = 0.045$, 0.06, 0.10, 0.15, 0.25, 0.40, 0.61, 1.0, 2.0, and 4.0. Dashed line has a slope of one.

would expect. For these and all other trajectories, we find systems spend the majority of time localized around $h = \pm 2$, commensurate with a particle diameter. The strength of the localization can be inferred from the fluctuations about $h = \pm 2$, which increase with increasing ϵ. Hence, as the system size increases, the strength of the localization decreases and cage breaking events become more frequent.

To quantify motions in h-space, we define a one-dimensional mean-square displacement (MSD), $\langle \Delta h^2(\Delta t) \rangle = \langle [h(t + \Delta t) - h(t)]^2 \rangle$, where the average extends over all initial times t. Shown in Fig. 4.3 are $\langle \Delta h^2(\Delta t) \rangle$ for various ϵ. For all system sizes, we observe diffusive behavior on short time scales such that $\langle \Delta h^2(\Delta t) \rangle \propto \Delta t$, however effects of finite system size are apparent from differences in the intercept at $\Delta t = 1$, as will be discussed shortly.

For the largest ϵ, $\langle \Delta h^2(\Delta t) \rangle$ retains diffusive behavior until finally plateauing due to the finite size of the system. However, the onset of distinctly subdiffusive behavior and development of increasingly long plateaus are apparent as ϵ is decreased. For the smallest values of ϵ in Fig. 4.3, $\langle \Delta h^2(\Delta t) \rangle$ is qualitatively similar to the MSDs of supercooled liquids

and glass formers, where the plateau indicates timescales over which caging occurs. The upturn of $\langle \Delta h^2(\Delta t) \rangle$ indicates that cage breaking eventually occurs for all systems.
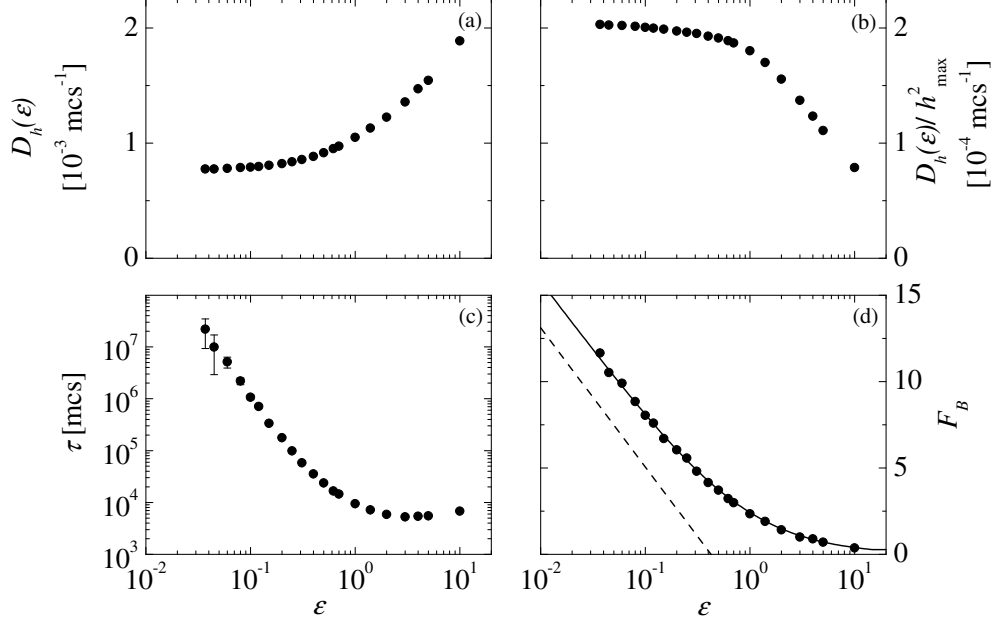
Figure 4.4: (a) Short time diffusion coefficient. (b) Short time diffusion coefficient scaled by squared system size. (c) Average time between cage breaking events. Error bars are calculated from the statistical uncertainty based on the number of events. Where not visible, error bars are smaller than the symbol. (d) Height of the free energy barrier as a function of ϵ. Circles are the results from simulations and the solid line is from the calculations described in Sec. 4.5. Dashed line grows as $\ln[\epsilon^{-7/2}]$ and shows scaling behavior as $\epsilon \to 0$.

Shown in Fig. 4.4(a) are the short time diffusion coefficients in h-space, defined as,

$$D_h = \frac{\langle \Delta h^2(\Delta t = 1) \rangle}{2}. \tag{4.2}$$

In Cartesian space, the short time diffusion coefficient is a constant with no spatial or system size dependence. In our 1D coordinate system, however, the diffusion coefficient becomes a function of space (discussed in Sec. 4.5) and system size. For small systems, D_h is relatively constant, though we do find a weak linear dependence on $h_{\max}$ (not shown).

As ϵ increases, however, D_h increases without bound as a consequence of our definition of h. To illustrate why D_h increases with ϵ, consider a large system where two particles are near to each other, while the other is an appreciable distance away. In this case, a small displacement of one of the proximal particles in Cartesian space can translate into a very large change in h. Hence, the unbounded increase of D_h with ϵ is not surprising. If the diffusion coefficient is normalized by the squared system size, however, as in Fig. 4.4(b), we find a trend opposite to that seen in (a). These values at small ϵ are again relatively constant, but decrease significantly as the system size increases. Thus, as ϵ increases, the system explores h-space more quickly, but relative to the size of the system, the exploration of space occurs slower.

To quantify a relaxation time scale, or the time the system spends caged, we define a transition time scale τ as the average time needed to cross $h = 0$ from positive h to negative h, or vice versa. As highlighted in Fig. 4.2, there can be small fluctuations about $h = 0$ that are not true cage breaking events. To minimize biasing τ toward lower timescales due to this sort of rattling, we stipulate that once $h = 0$ is crossed, the system must move a further distance l^* before returning. Otherwise, no crossing event is registered. If $F(h)$ defines the free energy landscape (see Sec. 4.5 for more details), the distance l^* is calculated as

$$l^* = \left(\frac{\int\limits_{-2}^{2} h^2 \, F(h) \, dh}{\int\limits_{-2}^{2} F(h) \, dh} \right)^{1/2}. \tag{4.3}$$

As will be discussed in Sec. 4.5, the height of the energy barrier decreases with system size but extends over a domain of $[-2, 2]$ for all systems. Hence, Eqn. (4.3) provides a consistent length scale for where the energy barrier drops to $\approx 3/5$ of its peak value (further details of calculating F_B are given in Sec. 4.5). Shown in Fig. 4.4(c), as ϵ decreases from 1 toward

0.1, the relaxation time increases, by approximately two orders of magnitude, and continues

to grow dramatically as the system becomes smaller. The smallest relaxation time occurs

when $\epsilon \approx 3.0$. For $\epsilon > 3.0$, relaxation times increase with increasing system size. Here,

the motion through the landscape is limited only by diffusion, which shown in Fig. 4.4(b),

decreases with increasing ϵ.

4.5   Energy Landscape

From Eqn. (4.1), determining the energy landscape is only a matter of calculating

the entropy for each macrostate h. For simplicity, we set $k_B T \equiv 1$ and write the free energy

of a state relative to the ground state as,

$$
\begin{aligned}
F(h) &= -T\left[S(h) - S_0\right] \\
&= -\ln\left[n(h)/n_0\right],
\end{aligned}
\tag{4.4}
$$

where 0 subscripts refer to the ground state at a given ϵ, and $n(h)$ is the number of states that

map to the same h. We calculate the number of states or multiplicity $n(h)$ by integrating

over the space of allowed configurations Ω of the three disks while maintaining a fixed h.

In general, this can be written

$$
n(h) = \int_\Omega d\vec{r}_1 \, d\vec{r}_2 \, d\vec{r}_3 \, \delta[h - H(\vec{r}_1, \vec{r}_2, \vec{r}_3)].
\tag{4.5}
$$

where the function $H(\vec{r}_1, \vec{r}_2, \vec{r}_3)$ calculates the value of h given the coordinates of the three

disks, and $\delta(h)$ is the Dirac delta function. The expression in Eqn. (4.5) can be reduced

to a 1D integral which we integrate numerically. We then calculate $F(h)$ using Eqn. (4.4).

Further details of calculating $n(h)$ are given in Sec. 7.1.

To determine the distribution $n(h)$ from simulations, we directly count the number
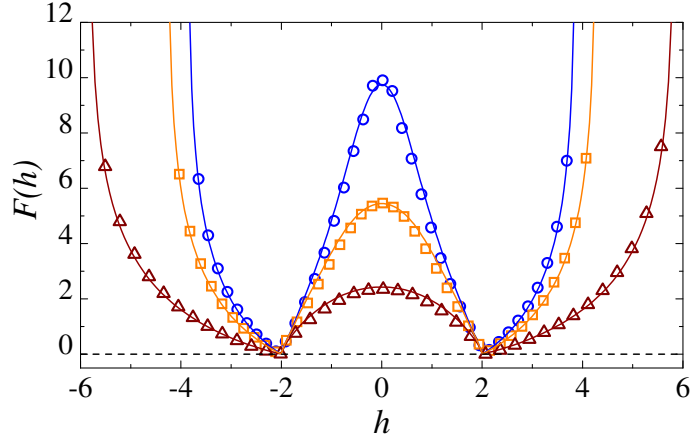
Figure 4.5: Comparison between theoretical energy landscapes (solid lines) and results from simulations (symbols). Circles: $\epsilon = 0.06$, squares: $\epsilon = 0.25$, triangles: $\epsilon = 1.00$.

of states by constructing histograms of h with small bins [189]. At this point, $F(h)$ can be computed directly using Eqn (4.4).

In Fig. 4.5, we compare analytical calculations of energy landscapes (solid lines) to those resulting from simulations (symbols). In all cases, the agreement between theory and simulation is excellent and so we are confident that the number of simulation steps adequately samples the configuration space. Energy landscapes for all values of ϵ are symmetric about $h = 0$ and are double-welled, with infinitely high barriers at $h = h_{\max}$, corresponding to particles being unable to escape the corral. The height of the energy barrier F_B, shown in Fig. 4.4(d), increases as ϵ decreases and diverges as $\epsilon \to 0$. As $\epsilon \to 0$, the height of the barrier grows as $\ln\left[\epsilon^{-7/2}\right]$, which can be predicted analytically and is described in Sec. 7.1.

The most probable h for *any* corral size occurs at $h = \pm 2$, as indicated by locations of the minima in Fig. 4.5. Inspecting Fig. 4.1(b), we see that there are more ways to place disk 3 at a value of h corresponding the cusp of the allowed region than anywhere else. For $|h| < 2$, the number of states is limited by configurations where particles overlap, whereas this constraint disappears for $|h| \geq 2$.

Given the energy landscape, we can now ascribe the localization about $h = \pm 2$ seen
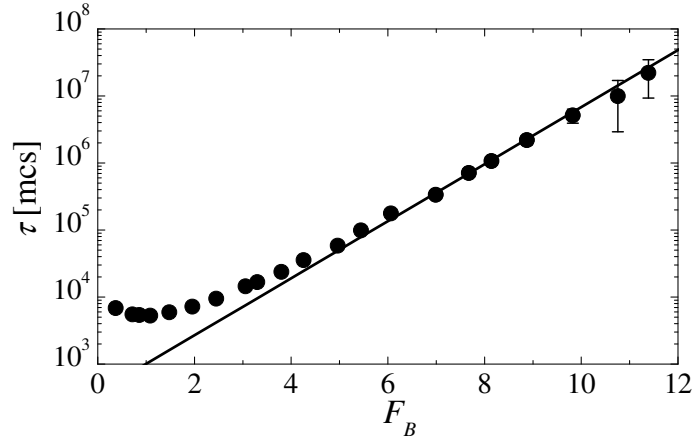
Figure 4.6: Symbols: Measured relaxation time as a function of theoretical free energy barrier height. Solid line is $378 \exp{(\beta F_B)}$, with $\beta = 0.98 \pm .04$, and comes from a weighted fit to data where $F_B \gtrsim 7.0$. To within statistical error, transition times grow Arrheniusly at these larger F_B.

in Fig. 4.2 to the system being trapped in one of two local energy minima. Furthermore, we see in Fig. 4.5 that the landscape broadens outward as ϵ increases, which explains the increase in fluctuations shown in Fig. 4.2. Inspecting Fig. 4.3, we see that a longer plateau in $\langle \Delta h^2 \rangle$ equates to a larger free energy barrier, and thus corresponds to the system being constrained at low ϵ and short times to explore only those regions near a minimum in the energy landscape. Given enough time, a large thermal fluctuation allows the system to cross the energy barrier, producing the upturn in $\langle \Delta h^2(\Delta t) \rangle$.

We are also now in a position to relate the energy landscape to the previously measured relaxation times. Shown in Fig. 4.6, we find that these relaxation times scale Arrheniusly with barrier height, to within statistical error, when $F_B \gtrsim 7.0$ ($\epsilon \lesssim 0.15$). Large F_B correspond to small ϵ, and as shown in Fig. 4.2, fluctuations about $|h| = 2$ decrease with decreasing ϵ. Hence, for large values of F_B, the system finds it difficult to explore large values of $|h|$ and the dominating factor in relaxation is the height of the energy barrier.
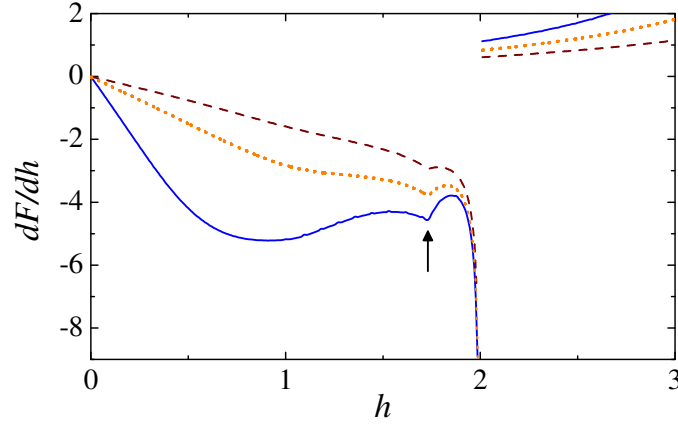
Figure 4.7: First derivatives of $F(h)$ for $\epsilon = 0.10$ (solid line), 0.31 (dotted line), and 0.62 (dashed line). Discontinuities exist at $h = \pm 2$. Additionally, a discontinuity exists in the second derivative at $h = \pm\sqrt{3}$, as indicated by the arrow.

When F_B is smaller, ϵ is larger and fluctuations about $|h| = 2$ are much more significant. In these cases, the system finds it easier to wander to larger values of $|h|$ and must first diffuse toward the barrier before crossing. This accounts for the deviation from Arrhenius behavior toward longer relaxation times at smaller F_B. When $F_B \lesssim 1.0$, relaxation becomes essentially independent of the barrier height and instead depends only on diffusion and system size.

In the overdamped limit of Brownian motion, Kramers rate theory [190] states that the time scale for crossing an energy barrier behaves as [191, 192]

$$\tau \propto (D\omega_m\omega_b)^{-1} \exp(\Delta E/k_B T), \tag{4.6}$$

where D is the diffusion constant, ω_m and ω_b are the curvature at the minimum and barrier, respectively, and $\Delta E \gg k_B T$ is the height of the energy barrier. In our case, ω_m is not defined. The energy landscapes shown in Fig. 4.5 are everywhere continuous, however they are *not* everywhere differentiable. In Fig. 4.7, we show the first derivative of $F(h)$ for $\epsilon = 0.10$, 0.31, and 0.62. As a consequence of confinement and the projection in h-space,
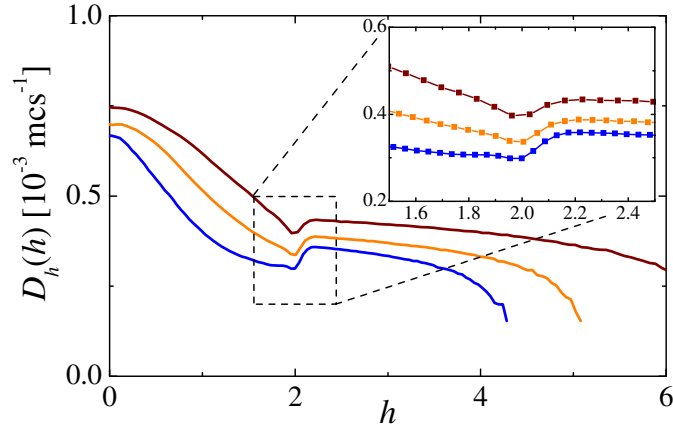
Figure 4.8: Spatially dependent diffusion coefficients for (bottom to top) $\epsilon = 0.31$, 0.70, and 1.40 for $h > 0$. Inset: a closer view of region near the kink in $F(h)$.

a kink in the free energy curve arises for all systems at $h = \pm 2$, and thus the first spatial derivative of free energy is discontinuous. The origins of the discontinuities are discussed in the appendix. Though the curves are steep, we point out that all values of dF/dh in Fig. 4.7 are finite. The discontinuity in dF/dh shows that ω_m is not defined and so the minimum cannot be approximated as harmonic. Thus, simple expressions from Kramers rate theory are not able to predict the transition times shown in Fig. 4.6. Additionally for all systems, we observe a kink in dF/dh at $h = \pm\sqrt{3}$, and therefore the second derivative of the free energy d^2F/dh^2 is discontinuous at these points.

Shown in Fig. 4.8 for $\epsilon = 0.31$, 0.70, and 1.40, the diffusion coefficient in h-space is spatially dependent. We calculate a spatial diffusion coefficient, $D_h(h)$ as in Eqn. (4.2), over a range $[h - \delta h, h + \delta h]$, where δh is $h_{\max}/100$. Near $h = \pm 2$, we measure the limiting value of the variance up to but not including these points. The spatially dependent diffusion coefficients appear to be continuous over all permitted values of h. To within our resolution, however, we cannot discern whether or not $D_h(h)$ is everywhere differentiable.

Our focus thus far has used h as a means of capturing the relevant cage breaking dynamics, but of course, one can imagine many options when reducing the configuration

space from six dimensions down to one. For consistency, it is worth checking that the results

shown above are not dependent on the choice of variable. We thus define a second variable

θ, shown in Fig. 4.1, that describes the angle between vectors $\vec{r}_{21} = \vec{r}_2 - \vec{r}_1$ and $\vec{r}_{31} = \vec{r}_3 - \vec{r}_1$.

A cage breaking event can then be defined when the system crosses $\theta = 0$ or $\theta = \pm\pi$. Free

energy landscapes in θ-space are shown in Fig. 4.9(a) for $\epsilon = 0.10$, 0.31, and 0.62 [193]. We

find the energy landscape is again double-welled, reflecting the two possible caged states,

and has even symmetry about $\theta = 0$ between $[-\pi, \pi]$. Here, unlike $F(h)$, we find that the

locations of the minima in the energy landscape are not constant but move to smaller values

of θ as ϵ increases. For example in Fig. 4.9(a), minima shift from $\theta = \pm.245\pi$ at $\epsilon = 0.10$

to $\theta = \pm 0.225\pi$ at $\epsilon = 0.62$.

As shown in Fig. 4.9(a), there are two energy barriers in θ-space as opposed to

the single barrier in h-space. While the representation has changed from variable h to θ,

the fundamental problem of caging has not, i.e. cage breaking is equally difficult or equally

easy independent of the representation. Hence, for these measurements of energy to be

consistent, there must be a relationship between the energy barriers measured in the two

different coordinate systems.

In Fig. 4.9(b), we show the height of the free energy barriers θ-space ϵ as a function

of the previously measured barrier heights in h-space. The heights of the barriers are

determined from the same simulation data that was used to calculate $F(h)$. To calculate

$F_B(\theta)$, we consider the probability that the system is poised to cage break, either at $\theta = 0$

or $\theta = \pi$. This yields an average barrier height

$$F_B(\theta) = -\log\{[n(0) + n(\pi)]/[2n_0]\}. \tag{4.7}$$

As shown in Sec. 7.1, $n(0) = 4n(\pi)$. Using this fact, we only measure $n(0)$ and n_0 to compute

$F_B(\theta)$ in Eqn. (4.7). The heights of the energy barriers in θ-space shown in Fig. 4.9(b) are
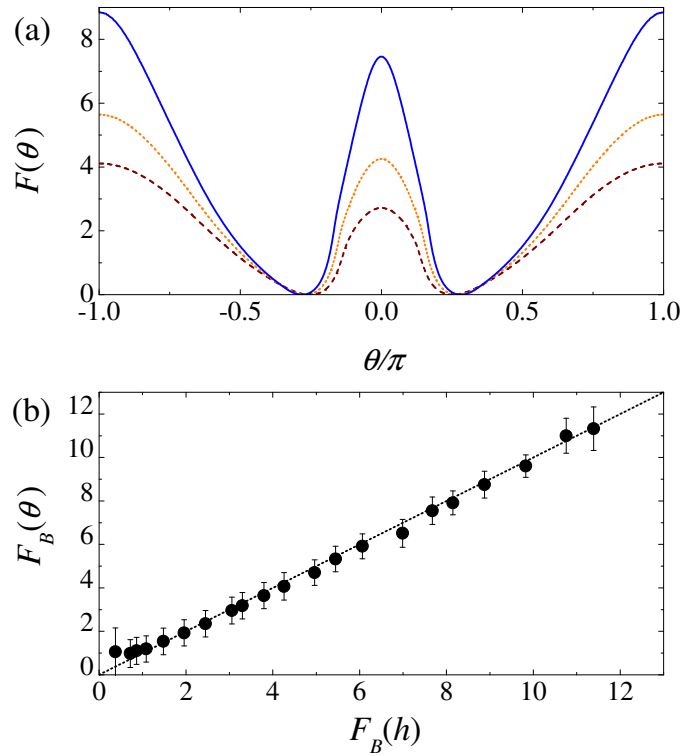
Figure 4.9: (a) Free energy landscape in terms of θ for $\epsilon = 0.10$ (solid line), 0.31 (dotted line), and 0.62 (dashed line). (b) Heights of energy barriers for all ϵ in θ-space versus the barrier height in h-space, calculated as described in the text. Error bars indicate the uncertainty in local quadratic fits of $n(0)$ and n_0. Dotted line is $F_B(\theta) = F_B(h)$.
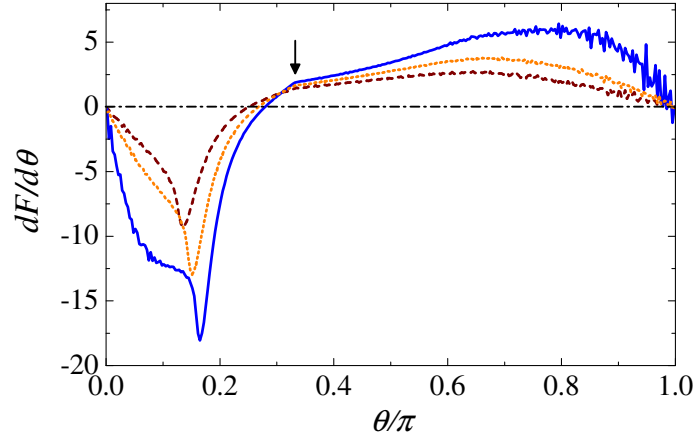
Figure 4.10: First derivative of $F(\theta)$ for $\epsilon = 0.10$ (solid line), 0.31 (dotted line), and 0.62 (dashed line). All first derivatives exhibit a subtle kink at $\theta = \pm\pi/3$ indicated by the arrow. Horizontal dashed-dotted line is at $dF/d\theta = 0$, and helps illustrate the gradual movement of the minimum to smaller values of θ for increasing ϵ.

in excellent agreement with those using h as a coordinate. The consistency between these two measurements demonstrate that both coordinates adequately describe caging and that the measured free energies are indeed those relevant to cage breaking in our system.

As in the case of $F(h)$, $F(\theta)$ is everywhere continuous. We show in Fig. 4.10 the first derivative of $F(\theta)$. Here, curves are obtained by numerically differentiating those in Fig. 4.9(a). In contrast to $F(h)$, $dF/d\theta$ is everywhere continuous, and so $F(\theta)$ is also everywhere differentiable. Without an analytical calculation of $F(\theta)$ we cannot draw definitive conclusions about the continuity of $d^2F/d\theta^2$. However, we do find for each ϵ the hint of a subtle kink in $dF/d\theta$ located at $\theta = \pm\pi/3$, as well as a second ϵ-dependent region where the slope of $dF/d\theta$ changes sharply, e.g. at approximately $\theta = 0.16\pi$ for $\epsilon = 0.10$ in Fig. 4.10. As in h-space, diffusion in θ-space also exhibits a complicated spatial dependence (not shown). One assumption underlying Eqn. (4.6) is that D is spatially independent. Predictions for τ which incorporate spatially dependent diffusion are highly non-trivial [192].

4.6　Discussion and Conclusions

We have introduced a model system composed of three hard disks confined to a circular corral. Though simple, this system exhibits caging and cage breaking behaviors, reminiscent of dense liquids, and allows us to exactly calculate a free energy landscape in terms of a single system coordinate. Respectively, caging and cage breaking can then be understood as the system becoming trapped in local energy minima and eventually being thermally excited over an energy barrier.

As the size of the system decreases, exploration of the configuration space is increasingly hindered by disk-wall and disk-disk interactions, though cage rearrangements do eventually occur for all $\epsilon > 0$. Arrhenius scaling describes the transition time τ between wells when the energy barrier is large and the system is small. However, this scaling fails for smaller energy barriers, when diffusion becomes the limiting factor in relaxation.

The coordinate(s) one uses to express the energy landscape must capture the behavior one is studying [153–161]. Those used in the text successfully describe motion from one cage to the other, however, there are any number of coordinates one could use that bear no relevance to caging. For example, the collective radius of gyration of the disks for configurations near and far from cage breaking may be equal. In the same respect, a particular value of h tells one very little about the actual configuration or spatial location of the disks. Furthermore, that caging can be described successfully in h-space or θ-space demonstrates that such projections of the landscape to a lower dimension are not necessarily unique.

Depending on the choice of coordinates, the energy landscape of hard disk and hard sphere systems may be locally non-differentiable. This observation highlights the notion that projection of a many dimensional landscape down to a lower dimensional representation may

introduce artifacts [158–160]. For systems with $N > 3$, it is probable that discontinuities in spatial derivatives of free energy disappear completely, or perhaps are only present for higher order derivatives.

For *any* purely soft core potential, the observed discontinuities will disappear. For a potential more representative of colloidal suspensions, such as a hard core potential with short ranged repulsion [35, 194], we expect the essence of our results to be valid, but in need of some modification. For example, a short range repulsion characterized by a length λ will not significantly affect the free energy when cage breaking occurs at particle separations larger than λ. In these cases, the free energy will be governed essentially by entropy and our results should apply. For more confined systems, i.e. when particle separations are $\lesssim \lambda$ during a cage break, whether or not the free energy is dominated by entropy or the potential will depend entirely on the details of the potential. We are currently investigating these scenarios.

It is conceivable that one could construct macrostate variables analogous to h to describe 3D systems. In a system of $N = 4$ hard spheres confined to a spherical corral, the 12D configuration space again leads to a tortuous but flat energy landscape. One possibility in this case is to calculate h_{3D} as the height of one particle above the plane formed by the remaining three, thus reducing the 12D configuration space to 1D. A cage break could then be identified as h_{3D} crossing 0, similar to our present study.

For systems where $N \gg 4$, one can imagine a projection to a lower dimensional space where the free energy landscape becomes nontrivial and meaningful, in the same manner as the projection from 6D to 1D in our model. Such a projection would reduce the dimensionality of the space to some fraction of $3N$, however, we suspect that any useful projection would remain $\mathcal{O}(N)$. Given that cage rearrangements in real systems near the glass transition can involve many more than 3 or 4 particles [102, 137, 174, 176, 182, 195],

the variables describing these systems are likely to be complex functions of many particle coordinates, and we do not foresee that such an approach would be tractable in practice. Our present work with a model system is meant to demonstrate that such projections are conceptually possible and in fact necessary for a simple picture of free energy landscapes to be applicable to systems with hard core potentials.

Chapter 5

Tracking Rotational Diffusion of Colloidal Clusters

The following chapter describes a computational method that can be used to compute and/or remove 2D and 3D rotational motions of groups of tracked particles. The technique was developed initially to remove rotational drift/diffusion of colloidal particles confined within emulsion droplets, as described in Chap. 3. During the same time I began work on confinement, Kazem Edmond began research on rotational diffusion of colloidal clusters in glassy systems and, at the time, the Weeks Lab did not have tracking algorithms for that purpose. However, at its core, the method I'd used to remove rotational motion for my project was precisely what Kazem required to study rotational diffusion. This collaboration led to thorough study and publication of the technique I'd developed [130] and two subsequent publications where the technique was used [196, 197]. All figures shown in this chapter appeared originally in [130] and are reproduced here with permission.

5.1 Introduction

Suspensions of spherical colloidal particles have proven a valuable model system for understanding many complex phenomena. Perhaps most notably, the model has provided insight into dynamical processes within different phases of matter [34, 39, 41, 43, 44, 137, 198, 199], as well as various mechanisms involved during phase transitions [42, 45, 200–203]. A combination of digital video microscopy and computerized particle tracking algorithms [204, 205] has allowed for the direct visualization of such colloidal systems and measurement of static and dynamical properties under many experimental conditions [131, 206–209]. Given the spherical symmetry of the particles, most previous studies have understandably focused only on understanding translational dynamics, though there have been a few studies on rotational dynamics in dilute systems of spheres [210, 211], and on the translational and rotational dynamics of anisotropic colloidal particles [212–215].

Within the past decade, researchers have developed a variety of techniques for synthesizing clusters of colloidal particles with a wide range of reproducible morphologies [216, 217], several of which are shown in Fig. 5.1. Colloidal clusters have the potential to extend the colloidal model past one of simple spherical particles and into a realm where the collective dynamics of particles with complex shapes, more representative of molecules, can be studied [218–220].

Conventional particle tracking methods [204, 205] are designed to follow the translational motions of individual particles, and so are immediately applicable to colloidal clusters, provided the particles can be reliably distinguished. However, a description of dynamics within systems composed of or including clusters is incomplete without knowledge of how rotational degrees of freedom are explored. Such an understanding could provide further insight into fundamental behaviors of systems with orientational order, such as liquid crys-
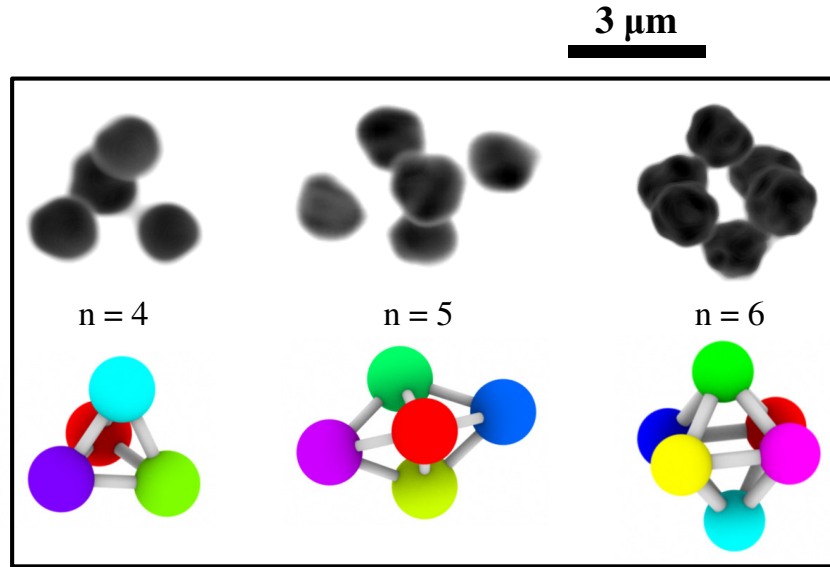
Figure 5.1: Top: Volumetric images of colloidal clusters with $n = 4$, 5, and 6 from 3D confocal micrographs. Images have been filtered and enhanced to allow easy visualization of the 3-dimensional structures. Individual particles are approximately 2 μm in diameter. Bottom: Ball-and-stick models of the clusters above. The cases $n = 4$ and $n = 5$ are accurate representations of the simulated tetrahedra and pentahedra discussed in the text.

tals, or systems subjected to external fields and anisotropic flows [215]. To our knowledge, there has been only one study that combined video microscopy with particle tracking to measure the rotational motion of colloidal clusters [221], using different methods than those described in this work. That study focused on dilute systems of planar clusters undergoing two-dimensional diffusion near a boundary, and revealed a decoupling of translational and rotational diffusion due to hydrodynamic effects.

We present here a simple and generalized method to track and calculate the two- or three-dimensional rotational motions of clusters of colloidal particles. Our method uses existing particle tracking routines and rigid body transformations to measure the changes in orientation of a cluster over time. To demonstrate the effectiveness and accuracy of the method, we simulate the motion of colloidal clusters under conditions that are relevant

to microscopy experiments. We then use our method to measure the rotational diffusion coefficient of a real colloidal cluster.

5.2 Calculating rotations

Our procedure for calculating rotational displacements of clusters is based on a method by Challis for determining rigid body transformations between reference frames [222]. Challis' procedure was originally intended for comparing osteometric measurements in biomechanical analyses. As we will show, the method can be intuitively adapted to measure rotational dynamics. First, we give a brief reprise of Challis' method, and then describe how it is used to study the systems mentioned here.

5.2.1 Challis' procedure for coordinate transformations

Given a set of points which have coordinates $\{\mathbf{x}_i\}$ measured in one reference frame and coordinates $\{\mathbf{y}_i\}$ measured in a second frame, there exists a transformation

$$\mathbf{y}_i = s\mathbf{R}\mathbf{x}_i + \mathbf{v}, \tag{5.1}$$

where subscript i refers to the i-th point in the set, s is a scale factor, $\mathbf{R}$ is a 3×3 rotation matrix, and $\mathbf{v}$ is the vector separation of the two reference frames. For our purposes, we may set the scale factor to unity and assume that both coordinate frames share a common origin, thereby setting all elements of $\mathbf{v}$ to zero.

We are therefore left with

$$\mathbf{y}_i = \mathbf{R}\mathbf{x}_i, \tag{5.2}$$

and only the rotation matrix to describe the transformation between coordinate frames.

The rotation matrix is an orthonormal matrix with the properties

$$\mathbf{R}\mathbf{R}^{-1} = \mathbf{R}\mathbf{R}^{\mathrm{T}} = \mathbf{R}^{\mathrm{T}}\mathbf{R} = \mathbf{E}, \tag{5.3}$$

$$\det(\mathbf{R}) = +1, \tag{5.4}$$

where $\mathbf{E}$ is the identity matrix and $\det()$ denotes the determinant.

For a set of n points, $\mathbf{R}$ can be calculated using a least squares approach. This method minimizes the quantity

$$\frac{1}{n}\sum_{i=1}^{n}[\mathbf{y}_i - \mathbf{R}\mathbf{x}_i]^{\mathrm{T}}[\mathbf{y}_i - \mathbf{R}\mathbf{x}_i]. \tag{5.5}$$

Ignoring the factor of $1/n$, expansion of Eq. (5.5) yields

$$\sum_{i=1}^{n}(\mathbf{y}_i)^{\mathrm{T}}\mathbf{y}_i + (\mathbf{x}_i)^{\mathrm{T}}\mathbf{x}_i - 2(\mathbf{y}_i)^{\mathrm{T}}\mathbf{R}\mathbf{x}_i. \tag{5.6}$$

Given that all $\mathbf{x}_i$ and $\mathbf{y}_i$ are fixed, minimizing Eq. (5.6) is therefore equivalent to maximizing

$$\sum_{i=1}^{n}(\mathbf{y}_i)^{\mathrm{T}}\mathbf{R}\mathbf{x}_i = \mathrm{Tr}\left(\mathbf{R}^{\mathrm{T}}\sum_{i=1}^{n}\mathbf{y}_i(\mathbf{x}_i)^{\mathrm{T}}\right) = \mathrm{Tr}(\mathbf{R}^{\mathrm{T}}\mathbf{C}), \tag{5.7}$$

where $\mathbf{C}$ is the cross-dispersion matrix calculated from the sum of the outer products of $\mathbf{y}_i$ and $\mathbf{x}_i^{\mathrm{T}}$

$$\mathbf{C} = \sum_{i=1}^{n}\mathbf{y}_i(\mathbf{x}_i)^{\mathrm{T}}. \tag{5.8}$$

At this point, a singular value decomposition (SVD) is performed on $\mathbf{C}$ such that

$$\mathbf{C} = \mathbf{U}\mathbf{W}\mathbf{V}^{\mathrm{T}}, \tag{5.9}$$

where $\mathbf{W}$ is a diagonal matrix containing the singular values of $\mathbf{C}$, and $\mathbf{U}$ and $\mathbf{V}$ are

orthogonal matrices. As was shown in [222], upon maximizing Eq. (5.7), $\mathbf{R}$ is given by

$$\mathbf{R} = \mathbf{U} \begin{bmatrix} 1 & 0 & 0 \\ 0 & 1 & 0 \\ 0 & 0 & \det(\mathbf{U}\mathbf{V}^{\mathrm{T}}) \end{bmatrix} \mathbf{V}^{\mathrm{T}}. \tag{5.10}$$

This procedure is applicable to all non-colinear sets of points with $n \geq 3$.

5.2.2   Application to colloidal clusters

Particle tracking [204, 205] yields vector coordinates $\mathbf{x}_i'$ for every particle i over a distinct set of times. Hence, the first step in tracking rotational motion of a cluster is to track the translational motion of each particle within the cluster. For each cluster, we first determine the center of mass $\mathbf{x}_{CM}$ at a given time and subtract this quantity from the coordinates of particles belonging to the cluster, thereby removing any translational motion. We are left with new coordinates $\mathbf{x}_i$ in the center of mass frame,

$$\mathbf{x}_i = \mathbf{x}_i' - \mathbf{x}_{CM}. \tag{5.11}$$

This step is equivalent to setting the elements of $\mathbf{v}$ to zero in Eq. (5.1). With translational motion removed, we may apply Eq. (5.2) with a slightly different interpretation. Rather than representing a transformation between coordinate frames, we may understand $\mathbf{R}$ as describing the rotational trajectory of a particle with inital position $\mathbf{x}_i^0$ to a final position $\mathbf{x}_i$ such that

$$\mathbf{x}_i = \mathbf{R}\mathbf{x}_i^0. \tag{5.12}$$

Therefore, given the coordinates from a particle tracking experiment, we may use Challis' procedure, starting from Eq. (5.8), to calculate a cross dispersion matrix $\mathbf{C}$ and subsequently perform a singular value decomposition to calculate a rotation matrix for each pair of successive times $[t, t + \Delta t]$. With the complete set of rotation matrices, $\{\mathbf{R}^k\}$, we

may reconstruct the entire trajectory of a particle about the cluster center of mass by computing the product of successive rotations. Given $\mathbf{x}_i^0$, the position of a particle at some later time t can be calculated as

$$\mathbf{x}_i(t) = \mathbf{R}^{t-\Delta t}\mathbf{R}^{t-2\Delta t}...\,\mathbf{R}^0\mathbf{x}_i^0 = \prod_k \mathbf{R}^k\mathbf{x}_i^0, \tag{5.13}$$

where the index k enumerates the rotation between successive times.

The advantage of calculating $\{\mathbf{R^k}\}$ is that it describes the collective behaviors of particles within a cluster, rather than a property of any individual particle. For example, knowledge of $\{\mathbf{R^k}\}$ for a cluster allows for immediate calculation of the motions of any particular particle about the center of mass, or the motion of the cluster about any arbitrary axis of rotation. Diffusive anisotropic clusters with large aspect ratios rotate more freely about a long axis than about a short axis. Given $\{\mathbf{R^k}\}$, however, one needs only the initial orientation of these axes to compute and compare the motions around them. An additional advantage of this procedure is that it is computationally fast, and the necessary linear algebra routines are standardly included in most mathematical software suites.

5.3 Tests of the prescribed method

For simplicity and to better reproduce the data collection process in typical microscopy experiments, we adopt a length scale of microns and a time scale measured in timesteps (ts), which is equivalent in microscopy to video frames or image stacks.

In conventional particle tracking experiments, it is important to minimize and understand the uncertainty, i.e. the noise, inherent in locating a particle. Typical microscopy experiments combine high magnification optics with CCD cameras to record raw digital images. In the absence of other sources of noise, the uncertainty in particle position, i.e. the minimum noise level, depends on the optical resolution [pixels/distance] of the instru-

mentation and the size [pixels] of the object being tracked. Standard image processing and particle tracking techniques can locate the centers of particles to within $\approx 1/N$ of a pixel, where N is the width of the object in pixels. Camera resolution varies between experimental set-ups but is typically in the range of 0.2 μm/pixel. The minimum uncertainty in particle position is the product of these factors. For example, observing a 10 pixel wide object with a resolution of 0.2 μm/pixel leads to a lower limit of $\approx$ 20 nm uncertainty in particle position. Other sources of noise, such as stray light entering the microscope, noise within the CCD camera itself, etc., slightly increase the uncertainty in particle position and further limit particle tracking resolution.

To test our method, we simulate the rotational Brownian motion of tetra- and pentahedral clusters with different rotational diffusion coefficients, D_R, and different levels of noise, σ_x. We first generate noise-free cluster trajectories. For tetrehedra, we place particles at initial coordinates

$$
\begin{aligned}
(R/\sqrt{3}) \cdot (1, \pm1, \pm1), \\
(R/\sqrt{3}) \cdot (-1, \pm1, \mp1),
\end{aligned}
\tag{5.14}
$$

where R is the distance from a particle center to the cluster center of mass. In this work, we study a range of $R \in [\sqrt{2}, \sqrt{10}]$ μm. For pentahedra, we use initial coordinates

$$
\begin{aligned}
R \cdot (1, 0, 0), \\
(R/2) \cdot (-1, \pm\sqrt{3}, 0), \\
R \cdot (0, 0, \pm1).
\end{aligned}
\tag{5.15}
$$

Once initialized, we evolve each simulation for 10^4 time steps.

At each time step, we select three random angles, α, β, γ, from a Gaussian distribution with a standard deviation of $\sqrt{2D_R}$. This distribution ensures that the simulated dynamics will be in agreement with the Stokes-Einstein-Debye relation discussed later [Eq.

(5.20)]. Each particle in a tetrahedron is rotated by an angle γ about the z-axis, then by an angle β about the y-axis, and finally by angle α about the x-axis to produce the tetrahedron at the subsequent time. The rotation matrices used are

$$\mathbf{R}_x(\alpha) = \begin{pmatrix} 1 & 0 & 0 \\ 0 & \cos\alpha & -\sin\alpha \\ 0 & \sin\alpha & \cos\alpha \end{pmatrix}, \quad \mathbf{R}_y(\beta) = \begin{pmatrix} \cos\beta & 0 & \sin\beta \\ 0 & 1 & 0 \\ -\sin\beta & 0 & \cos\beta \end{pmatrix},$$

$$\mathbf{R}_z(\gamma) = \begin{pmatrix} \cos\gamma & -\sin\gamma & 0 \\ \sin\gamma & \cos\gamma & 0 \\ 0 & 0 & 1 \end{pmatrix}. \tag{5.16}$$

Thus, given an initial position vector $\mathbf{x}^0$, the subsequent position vector is $\mathbf{x} = \mathbf{R}_x\mathbf{R}_y\mathbf{R}_z\mathbf{x}^0$.

This method of generating rotational Brownian motion is not strictly correct for the given pentahedral geometry as its motions cannot be generally characterized by a single D_R. However, using the publicly available package HYDRO++, we calculate the difference in D_R between long and short axes to be $\approx 2\%$. Given this small variation, the use of a single D_R to describe a pentahedron is a more than sufficient approximation for the purpose of testing our algorithm, which after all does not require that the motions agree with the laws of diffusion.

Trajectories generated in this way are noise-free in the sense that they are absent of uncertainty in particle position to within machine precision. To mimic the type of experimental noise previously mentioned, we post-process the trajectories by adding Gaussian random numbers, with standard deviation σ_x, to the particle coordinates. The levels of noise presented here correspond to uncertainties of $\sigma_x \in \{10,\ 30,\ 50,\ 70,\ 100\}$ nm in the x-, y-, and z-directions. Experimental uncertainties are typically within the range of 20-60

nm, and so the levels studied here are relevant to microscopy experiments. After the noise is added, we apply our method of measuring rotational motion in order to gauge the effect of experimental noise on results.

5.4   Analysis of rotational motion

In this section, we calculate the rotational motions of simulated colloidal clusters using the matrix methods described above. We focus on a method that uses the rotation matrices to determine the motion of a fictional orientation vector attached to the cluster. The rotational displacements of one or more such vectors about the center of mass can be used to compare and contrast motions about different axes, which is especially useful when the objects studied are anisotropic and motions about axes are expected to differ [223, 224].

We note that a second method exists to calculate rotational displacements using solely the rotation matrix. This method determines the rotational axis from $\mathbf{R}$ and can then be used to calculate the magnitude of an angular displacement. While a mathematically direct and general approach, it describes only the average cluster dynamics and can provide no insight into how motions about different axes vary. Given these limitations, we relegate a description of this method to the appendix.

To analyze the rotations of a cluster, we consider the motions of an initial orientational unit vector $\hat{\mathbf{p}}^0$ fixed to the cluster. We determine its orientation at a later time t by applying the set of rotations such that

$$\hat{\mathbf{p}}(t) = \prod_k \mathbf{R}^k \hat{\mathbf{p}}^0, \tag{5.17}$$

in a similar way as in Eq. (5.13). Although there are no constraints on what one may select $\hat{\mathbf{p}}^0$ to be, some choices may be more enlightening than others. For example, the cluster $n = 5$ shown in Fig. 5.1 has distinct long and short axes, and so one expects slower

diffusion about the short axis. To quantify how rotational dynamics about these axes differ, one could choose two $\hat{\mathbf{p}}^0$ to study separately: one choice of $\hat{\mathbf{p}}^0$ perpendicular to the long axis; a second perpendicular to the short. Such a procedure would yield information relating to motions about the long and short axes, respectively.

In line with [223–225], we define a vector rotational displacement

$$\vec{\varphi}(t) = \int_0^t \vec{\omega}(t')dt' \tag{5.18}$$

in the time interval $[0, t]$. The vector $\vec{\omega}(t')dt'$ has a direction given by $\hat{\mathbf{p}}(t') \times \hat{\mathbf{p}}(t' + dt')$ and magnitude $|\vec{\omega}(t')dt'| = \cos^{-1}[\hat{\mathbf{p}}(t') \cdot \hat{\mathbf{p}}(t' + dt')]$, which is the angle subtended by $\hat{\mathbf{p}}$ during this time interval.

To illustrate the meaning of $\vec{\varphi}(t)$, consider an object with constant angular velocity $\vec{\omega} = \omega\hat{\mathbf{z}}$. Over a time Δt, the rotational vector displacement is given by $\vec{\varphi}(\Delta t) = \vec{\omega}\Delta t = (0, 0, \omega\Delta t)$. Therefore in general, $\vec{\varphi}(t)$ has components in each of the Cartesian axes, $(\varphi_x, \varphi_y, \varphi_z)$, corresponding to cumulative rotations about those axes.

In Fig. 5.2(a), we show the orientational trajectories of particles within a simulated tetrahedron projected onto the surface of a unit sphere. Fig. 5.2(b) shows 2D projections of trajectories for two $\hat{\mathbf{p}}^0$ through the rotation space described above. As shown in Fig. 5.2, even though the cluster is a solid body, trajectories of individual particles differ due to rotations of the cluster about random axes.

Given the definition of $\vec{\varphi}(t)$ in Eq. (5.18), we may define an unbounded mean square angular displacement (MSAD), akin to a translational mean square displacement, as

$$\langle\Delta\vec{\varphi}^2(\Delta t)\rangle = \langle[\vec{\varphi}(t + \Delta t) - \vec{\varphi}(t)]^2\rangle, \tag{5.19}$$

where the angle brackets indicate an average over all equivalent lag times Δt. In three
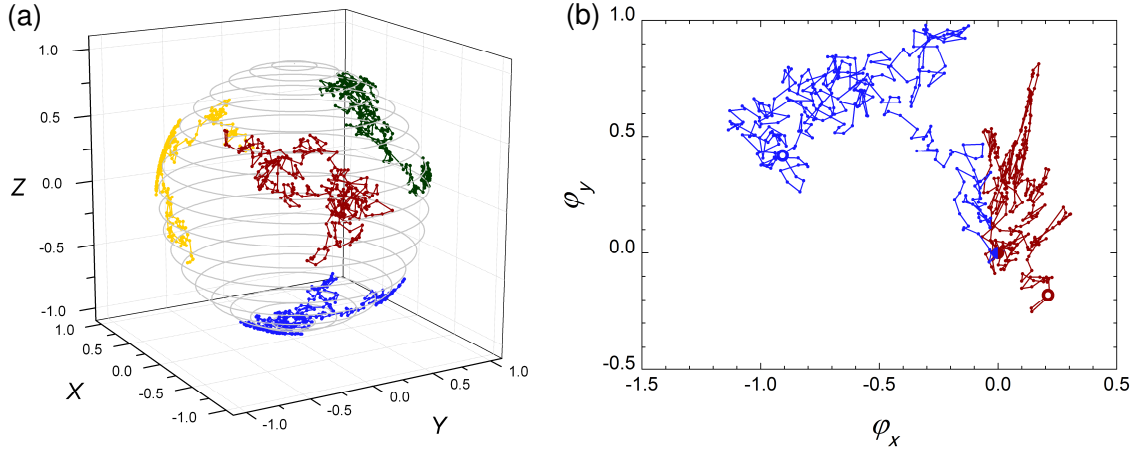
Figure 5.2: (a) Trajectories of particles within a simulated Brownian tetrahedral cluster projected onto the surface of a unit sphere. Colors represent different particles, i.e. different choices for $\hat{\mathbf{p}}^0$. (b) 2d projection of two trajectories through rotation space (φ_x, φ_y). Colors correspond to the same particles in (a). Both trajectories in (b) begin at $(0,0)$ and end at open circles.

dimensions the Stokes-Einstein-Debye relation states that the MSAD grows as

$$\langle \Delta \vec{\varphi}^2(\Delta t) \rangle = 4 D_R \Delta t, \tag{5.20}$$

where D_R is the rotational diffusion coefficient. In this paper, we focus on measuring the MSADs of clusters, but we point out that other techniques exist to quantify rotational dynamics. For example, by observing the decay of an orientational correlation function $\langle \hat{\mathbf{p}}(t + \Delta t) \cdot \hat{\mathbf{p}}(t) \rangle$ one can measure D_R [226, 227]. Our method can be applied, in this case, to compute $\hat{\mathbf{p}}(t)$ as in Eq. (5.17).

In Fig. 5.3(a) & (b), we show the MSAD of two simulated tetrahedral clusters with diffusion constants 10^{-4} rad^2/ts and 10^{-3} rad^2/ts respectively and different levels of noise. The influence of noise is apparent in Fig. 5.3 as deviations from linearity at small Δt. Eventually, the MSAD recovers the true diffusive behavior because the cluster has made rotations large enough to distinguish from the noise.
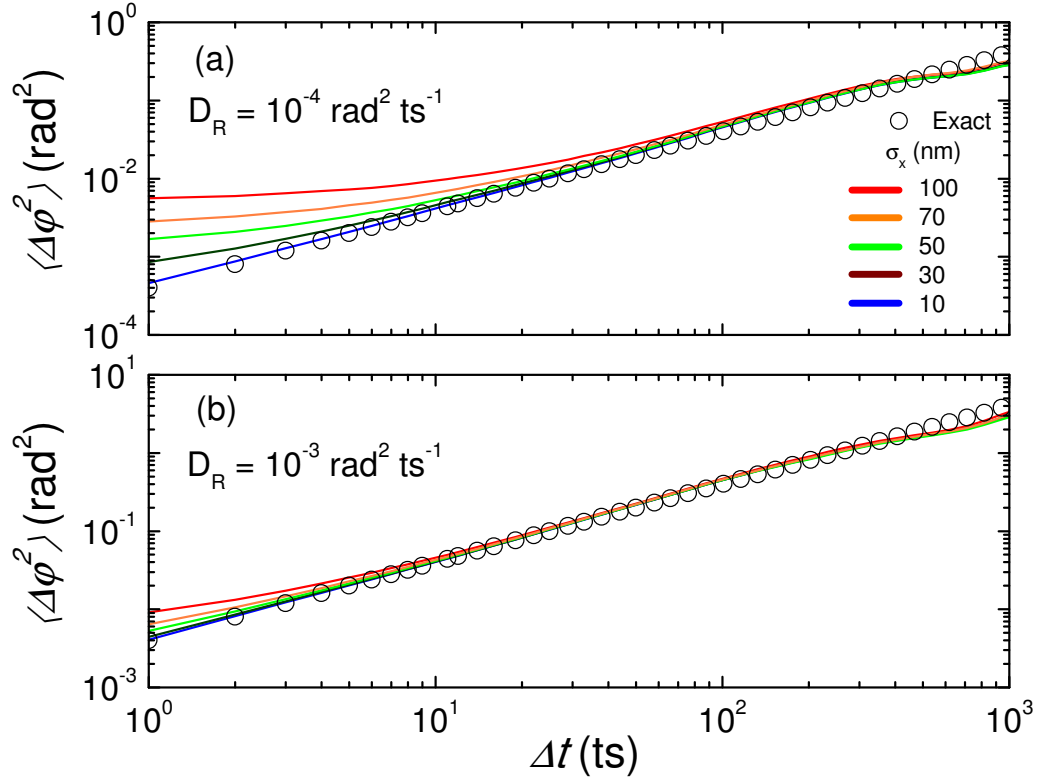
Figure 5.3: Mean square angular displacements of simulated tetrahedral clusters ($R = \sqrt{3}$ μm) for different noise levels σ_x and diffusion coefficients of (a) 10^{-4} rad^2/ts and (b) 10^{-3} rad^2/ts. Open circles are the theoretical MSAD based on Eq. (5.20). Deviations from linearity at small Δt demonstrate the effect of noise when resolving small rotations. Deviations at large Δt, however, are the result of low statistics at these lag times.

With no experimental noise, a log-log plot of MSAD as a function of Δt will be a straight line with a slope of unity, as indicated by the open circles in Figs. 5.3(a) & (b). However, in the presence of noise in particle positions, rotations cannot be accurately resolved below a certain threshold, Φ. For example, a stationary cluster will appear to make small, but fictional, rotations as a result of this noise, and measurements of the MSAD will yield

$$\langle \Delta \vec{\varphi}^2(\Delta t) \rangle = \Phi^2, \tag{5.21}$$

where Φ^2 is independent of Δt due of the lack of correlations in noise.

In the case of translational diffusion, one expects that the noise in each direction will contribute an error of $2\sigma_x^2$ to the mean-square displacement [204]. In terms of an angular uncertainty, this contribution is diminished by a factor of R^2, where R is the average distance from a particle to the cluster center of mass. Our matrix method reduces this uncertainty further by a factor of n. Thus, when only static noise is present, one expects for a diffusing cluster

$$\langle \Delta \vec{\varphi}^2(\Delta t) \rangle = 4D_R \Delta t + \Phi^2, \tag{5.22}$$

where

$$\Phi^2 = 6\sigma_x^2/nR^2. \tag{5.23}$$

To test this assertion, we add noise to simulations of stationary ($D_R = 0$) tetrahedral clusters and calculate the MSADs. As in Eq. (5.21), the MSADs are constant over time. We take Φ^2 to be the value of the MSAD as $\Delta t \to 0$. Shown in Fig. 5.4(a), Eq. (5.23) accurately describes the static angular uncertainty for a wide range of tetra- and pentahedral cluster sizes, R, and noise levels. Fig. 5.4(b) shows all of the previously measured MSADs in Fig. 5.3 plotted with the noise subtracted. This precisely collapses the MSADs to the true values in each case.
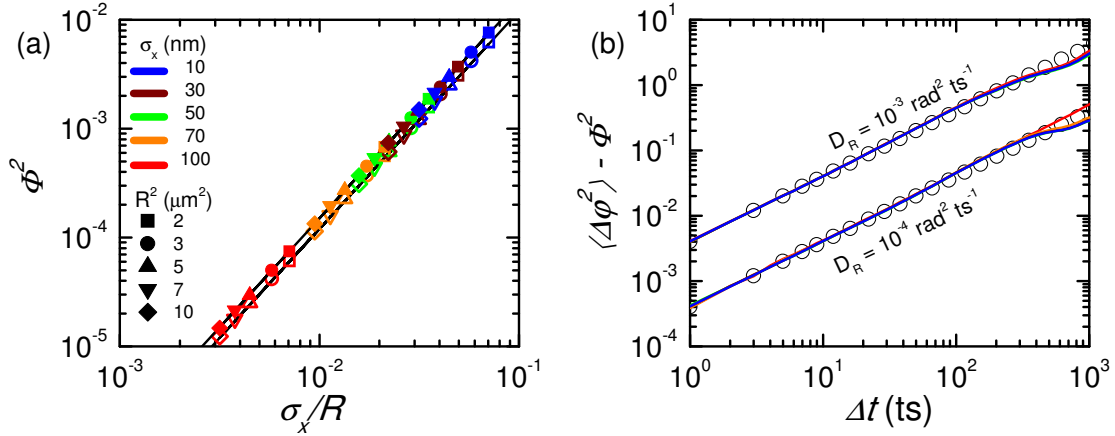
Figure 5.4: (a) Measured values of Φ^2 for non-diffusing tetrahedral (solid symbols) and pentahedral (open symbols) clusters. Colors indicate noise levels and symbols indicate cluster size. Solid lines are the prediction $\Phi^2 = 6\sigma_x^2/nR^2$. (b) Same data in Fig. 5.3 with the appropriate Φ^2 for each noise level subtracted.

Knowing how uncertainty in particle positions affects measurements of dynamics quantities, such as the MSAD, is clearly important. However, one is typically unable to define the noise level so precisely in experiments. As stated earlier, particle tracking resolution depends on various experimental factors including particle size, optics, and the type of camera used to record images. As shown in Fig. 5.3(a), for slowly diffusing clusters and moderate-to-high noise levels, the measurements of the MSAD may not be representative of the true dynamics until fairly large lag times.

In microscopy experiments, one can effectively increase the rotational signal-to-noise ratio between each time step by imaging less frequently. Determining the appropriate sampling rates in experiments can be done by estimating the noise level σ_x, the diffusion constant D_R and calculating an approximate Φ^2. Diffusive motion will begin exceeding noise when $\Phi^2 \approx 4D_R\Delta t$. Solving for Δt then yields a reasonable sampling lag time. It is also important to avoid undersampling, that is, too long a lag time. Doing so will make diffusive

motion between images appear erroneously slow. We find that a good rule of thumb for the upper limit on sampling time should be the time when the cluster has diffused ≈ 1 radian^2. Thus, an estimate for the upper limit is $\approx 1/4D_R$. However, as in all particle tracking experiments, the time between images must be small enough that individual particles can be confidently identified. This typically means that particles must be imaged before moving a distance of one interparticle spacing [204].

5.5 Experimental application

Measurements of rotational motion of diffusive tetrahedral clusters have been performed using the described method [217]. Real fluorescent tetrahedral clusters are synthesized as in [217]. A cluster is composed of individual poly(methyl methacrylate) (PMMA) spheres, each with a diameter 2.45 μm as measured by static light scattering (SLS). The particles within a cluster are irreversibly bound together, but are sterically stabilized to prevent the possibility of aggregation to other clusters. Dilute suspensions of clusters are prepared in a mixture of cyclohexyl bromide (CXB) and *cis*-decalin (DCL) at a ratio of 85/15 (w/w) that closely matches both the density and index of refraction of the particles. Clusters are imaged in 3D over time with a Leica TCS SP5 confocal microscope. We track locations of the individual particles within a tetrahedron using standard particle tracking routines [204, 205]. The uncertainties in particle position for these experiments are ≈ 30 nm in the x- and y-directions, and ≈ 40 nm in the z-direction. Given these tracking resolutions and assuming a maximally packed tetrahedron, from Eq. (5.23) we estimate the angular resolution in this experiment as $\Phi \approx 0.028$ radians (1.6°).

Once tracked, we calculate the translational MSD and the MSAD and determine the translational and rotational diffusion coefficients, D_T and D_R, respectively. In three

dimensions, the translational MSD is described by the Stokes-Einstein-Sutherland equation

$$\langle \Delta r^2 \rangle = 6D_T \Delta t, \tag{5.24}$$

while the MSAD is described by Eq. (5.20).

Hydrodynamically, tetrahedral clusters can be accurately modeled as spheres [228] given the relation

$$d_{\text{tetra}} = 1.844 \times d_{\text{sphere}}, \tag{5.25}$$

where d_{tetra} is the effective hydrodynamic diameter of the cluster, and d_{sphere} is the diameter of the particles within the cluster. Theoretical translational and rotational diffusion coefficients, D_T and D_R respectively, can be calculated using

$$D_T = \frac{k_B T}{3\pi \eta d_{\text{tetra}}} \tag{5.26}$$

$$D_R = \frac{k_B T}{\pi \eta d_{\text{tetra}}^3}, \tag{5.27}$$

where k_B is Boltzmann's constant, T is the temperature, and η is the viscosity of the suspending solvent. The viscosity of the CXB/DCL mixture was measured at $\eta = 2.18$ mPas and experiments were performed at $T = 295$ K.

In Fig. 5.5, we show the MSD and MSAD of a diffusing tetradedral cluster. The MSD corresponds to motions of the center of mass of the cluster, and the MSAD is an average over the individual particle MSADs (i.e., using the initial orientations of the particles as four separate $\hat{\mathbf{p}}^0$). Solid lines are fits to the data over the indicated range $3\,\text{s} \leq \Delta t \leq 22\,\text{s}$. As can be seen, both the MSD and MSAD are approximately linear only at small lag times. This is because the data set used to make these measurements consists of only a
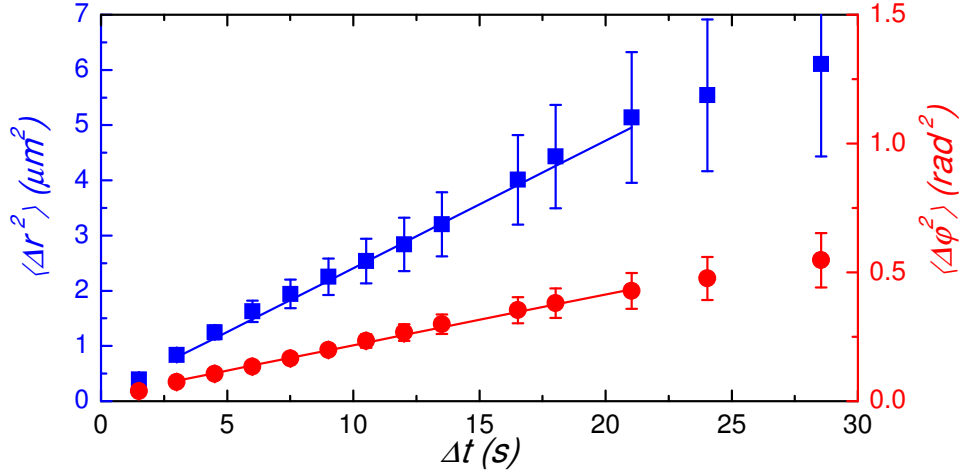
Figure 5.5: Calculated MSD (blue squares) and MSAD (red circles) of a diffusing experimental tetrahedral cluster. Solid lines are best fit lines over range of data used to determine the respective diffusion coefficients.

single cluster for less than 300 timesteps (≈ 220 s). Diffusion coefficients are measured by performing linear fits to the MSD and MSAD shown in Fig. 5.5 over the indicated range and extracting the slopes of the lines.

Table 5.1: Measurements from Tracking a Tetrahedral Cluster

Diffusion	Coefficient	d_{tetra} (μm)	d_{sphere} (μm)
Trans.	$(3.85 \pm 0.49) \times 10^{-2}$ μm^2/s	5.12 ± 0.67	2.78 ± 0.36
Rot.	$(4.93 \pm 0.49) \times 10^{-3}$ rad^2/s	4.94 ± 0.16	2.68 ± 0.09

Shown in Table 5.1 are the measured translational and rotational diffusion coefficients. Values of d_{tetra} are calculated from Eqs. (5.26) & (5.27) using known experimental conditions, and values for d_{sphere} then follow trivially using Eq. (5.25). Ideally, the sizes calculated from translational motions would be identical to those calculated from rotational motions. As shown, these values agree to within 4%. Such good agreement between these two measurements demonstrates our ability to track translational and rotational motions

of clusters simultaneously.

Previous work using standard particle tracking and our matrix method reported particle diameters $\approx 14\%$ larger than the 2.45 μm measured by SLS [217] . A reanalysis of the data with improved particle tracking, presented above, increases the accuracy of the particle diameter measured using our matrix method to within $\approx 9\%$. The remaining disagreement is likely due to multiple factors, including the fitting routines used in SLS and swelling of particles when in a solvent of CXB/DCL. SLS measurements were performed with suspensions in pure DCL, which is not known to swell particles.

5.6   Discussion and Conclusions

We have presented a simple method of tracking the rotational motions of colloidal clusters. Our method implements conventional particle tracking routines to determine the locations of individual particles within a cluster and uses this information to compute rigid body transformations that describe changes in a cluster's orientation over time. The set of matrix transformations constitutes a global description of a cluster's motion during the course of an experiment or simulation and allows one to calculate rotational dynamics about any arbitrary axis. The least squares minimization used in this method considers the motions of each individual particle in calculating the rotation matrix, and therefore measurements of rotational displacements are less sensitive to tracking noise. Additionally, precision in determining angular displacements increases with cluster size R. When combined, the resolution of measuring angular displacements scales with $1/nR^2$.

Though constructed specifically for tracking colloidal clusters, we emphasize that our method is not limited to these systems, but is applicable to following the rotational motion of any body over time, providing that at least three distinct noncolinear points

in the body can be reliably distinguished. Because the accuracy of tracking a rotation depends on the number of particles and the size of the body, the possibility exists that this method can be adapted to many-body systems where each particle diffuses independently of the rest while the system itself also undergoes bulk rotations. In this scenario, diffusive motions are random and can therefore be treated as noise while calculating $\{\mathbf{R}^k\}$ for the system. The rotation matrices can be inverted and, in a manner similar to Eq. (5.13), the bulk rotations can be removed, leaving only uncorrelated diffusive motion. Thus, this method is also applicable to determining particle motions in rotating coordinate frames.

Chapter 6

Summary and Outlook

In this dissertation, I have presented work that explores the dynamical behavior of Brownian systems comprised of particles with hard core potentials. While each project is fairly distinct from another, each focuses on understanding a fundamental aspect of the glass transition. While my research relates most immediately to colloidal suspensions, I have discussed how this work is relevant to other glass forming materials and have (hopefully) demonstrated that the glass transition is more "universal" than previously known.

6.1 Confinement

In the experimental portion (Chap. 3), hard sphere colloidal particles were used as a model glass forming material and were confined within emulsion droplets. In doing so, I was able to study how particle dynamics in the droplets varied with the viscosity of the external medium. As in molecular liquids and polymers, it was found that these samples respond to confinement differently depending on the material to which they are confined. Dynamics were slowed more when the viscosity of the external phase was higher. I also observed directly a gradient in particle mobility as a function of distance to the boundary.

Features of this gradient change depending on both system size and the viscosity of the external phase, and these variations were determined to be the origin of the differences in dynamics between samples. For polymers and molecular glass formers, strong evidence exists in support of dynamical gradients near interfaces [77, 78, 82, 83, 121, 122]. Furthermore, it is believed that interactions between a sample and the confining material can modify these gradients [69, 79, 82, 83]. These effects are precisely what has been observed in my experiments and are, I believe, provide further strong evidence for the presence of such effects in other confined glass formers.

I was limited by several experimental factors from studying these systems in further detail. Perhaps the largest obstacle is that of difference in index of refraction between the suspension and the external phase. Refractive indices need to be closely matched to see deep within a sample using confocal microscopy. For my materials and samples, I was limited to studying droplets with radii ≈ 16 μm, hence I could not determine whether or not the high ϕ data given in Fig. 3.10 converge at larger R.

Future experiments of this type would benefit from finding an external phase with a refractive index that more closely matches that of the suspension, allowing one to study larger droplets with confocal microscopy. Additionally, external phases with both smaller and larger viscosities would allow one to explore the viscosity dependence more fully. It would also be beneficial to improve upon the method of making colloid-filled emulsion droplets. As discussed, droplets were made by mixing the suspension with the external phase in a vial and shaking by hand. Microfluidic techniques could perhaps be used to produce droplets of uniform size and more uniform volume fraction. If the viscosity of the external phase could be increased by say an order of magnitude, such microfluidic techniques would likely be necessary to make droplets at all.

6.2 Free Energy Landscapes

Chapter 4 discusses the results of simulations and theory to describe how dynamics in a model system of three confined hard disks relate to an underlying energy landscape. For systems of hard disks and hard spheres, the free energy landscape is flat. My approach in this work was to project the complete 6D configuration space down to 1D, and in doing so one obtains a representative free energy landscape with energy maxima and minima. I found that when the disks are highly confined, the average time the system spends in a caged state scales Arrheniusly with the height of the free energy barrier. I also showed that as a consequence of projecting to a lower dimensional phase space, features like diffusion become non-trivial to describe in terms of the space.
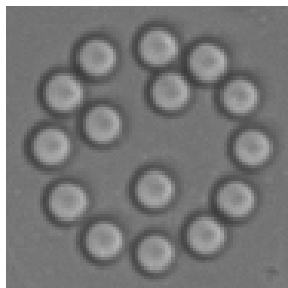
Figure 6.1: Experimental system similar to the one used in simulations in Chap. 4. Here, 3 μm diameter silica particles are sedimented to a glass coverslip. Laser tweezers are used to approximately fix particles at the edge into a circular corral. The three particles inside are allowed to diffuse freely. Data courtesy of Ian Williams.

In collaboration with Ian Williams and Paddy Royall at the University of Bristol, we have recently begun work studying an experimental system similar to the one in Chap. 4. Shown in Fig. 6.1, 3 μm silica spheres are sedimented to a glass coverslip, and outer particles are held in place using laser tweezers while the inner three particles can diffuse freely. The spheres in this experiment approximate the disks used in simulations, and it will be interesting to learn how accurate our simulations and theory are compared to a real phys-

ical system. This system is clearly similar in many respects, but also contains important differences. First, there is some degree of polydispersity in the size of the spheres. Second, depending on the solvent, silica spheres may be able to diffuse very slightly out of plane. We do not believe that either of these factors will contribute significant differences to the results from simulations. Polydispersity is likely to be very small, and the solvent can be tuned so that diffusion out of plane is slight. The most important differences are likely to arise from electrostatic interactions between the particles, which effectively changes hard spheres into soft ones. In that case, whether or not our results adequately describe cage breaking in this experimental system will depend entirely upon the details of these interactions. We are also planning to begin soon simulations with potentials more representative of colloidal particles, which are discussed in Sec. 4.6.

6.3 Cluster Tracking

The cluster tracking algorithm presented in Chap. 5 has since been used by Kazem Edmond to track tetrahedral colloidal clusters in a glassy sea of colloidal spheres. The goal of that project was to observe whether or not translational and rotational diffusion constants decouple near the glass transition. This was indeed found to be the case, as has been observed before in simulations and experiments of molecular liquids, and is currently under review for publication in PNAS [197]. In addition to Kazem's experiments, Nabiha Saklayen has begun experiments to also investigate decoupling of rotational and translational diffusion in a 2D granular system of vibrated clusters, and is using the same algorithms to track these clusters. The goal of this project is to understand what role (if any) cluster shape has on the observed decoupling. One can imagine that a cluster of many disks can be formed into a variety of shapes representative of molecules, and how decoupling depends

on purely geometrical properties of particles is unknown. Preliminary results indicate that, for triangular trimers at least, decoupling in the granular system is similar to that seen in colloids (and molecular liquids).

Chapter 7

Appendices

7.1   A Free Energy Landscape for Cage Breaking of Three Hard Disks

Here we present a derivation of $n(h)$ based on geometric arguments. Because the distribution $n(h)$ has even symmetry about $h = 0$, we directly treat only the cases where $h \geq 0$. All three disks are distinguishable and have the same diameter d. In simulations, we used $d = 2$, but for clarity of presentation here we assume no specific disk size. The true radius of the corral is $R_C = 3r + \epsilon$, but for simplicity, we define $R = d + \epsilon$ as the radius of the corral accessible to the centers of the disks, as illustrated in Fig. 7.1.

While Eqn. (4.5) is general and exact, it can be further simplified for our system. Recalling that $H(\vec{r}_1, \vec{r}_2, \vec{r}_3)$ in Eqn. (4.5) maps all rotationally equivalent states to the same h, we may consider only a single orientation of the system, such as the one in Fig. 7.1. We constrain disks 1 and 2 to always lie along the same horizontal line of length L_{12}, at a distance y above the bottom of the corral. For a given h, disk 3 may lie anywhere along a second horizontal line, L_3, at a distance $y + h$ above the bottom of the corral. Thus, the
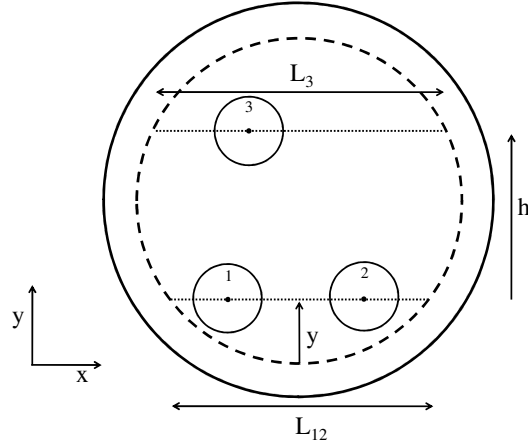
Figure 7.1: The radius of the solid outer circle is $R_C = R + r$ and is the physical boundary, but the centers of the confined disks can only exist a distance $\leq R$ from the center, indicated by the dashed inner circle.

number of states $n(h)$ can be written as the product of integrals

$$n(h) \propto \int dy \int dx_1 \int dx_2 \int dx_3, \tag{7.1}$$

and the problem becomes determining the appropriate limits of integration. For a circle centered at $(0, R)$, we determine the lengths of chords L_{12} and L_3 to be

$$L_{12} = 2\sqrt{2yR - y^2} \tag{7.2}$$

$$L_3 = 2\sqrt{2(y + h)R - (y + h)^2}. \tag{7.3}$$

There are four cases that must be considered to calculate $n(h)$ correctly, each of which is geometrically distinct.

7.1.1   Case A $(h \geq d)$

The first of four cases that must be considered is shown in Fig. 7.1. This is the simplest case in that disk 3 never comes into contact with disks 1 or 2. Taking that the

chord L_{12} begins at $x = 0$, the lower and upper bounds of x_2 are, respectively $x_1 + d$ and L_{12}. The lower and upper bounds of x_1 are 0 and $L_{12} - d$. Disk 3 may exist anywhere along the chord L_3 independently of x_1 and x_2, so the lower and upper bounds for x_3 are 0 and L_3. Therefore,

$$
\begin{aligned}
n_A &\propto \int_{y_{\min}}^{y_{\max}} dy \int_0^{L_3} dx_3 \int_0^{L_{12}-d} dx_1 \int_{x_1+d}^{L_{12}} dx_2 \\
&= \int_{y_{\min}}^{y_{\max}} dy \, L_3 \left[\frac{(L_{12}-d)^2}{2} \right].
\end{aligned}
\tag{7.4}
$$

The lower limit $y_{\min}$ corresponds to when disks 1 and 2 are in contact at the bottom of the corral. Geometry yields that this occurs at

$$
y_{\min} = R - \sqrt{R^2 - \frac{d^2}{4}}
\tag{7.5}
$$

In this case, the upper limit $y_{\max}$ can correspond to $L_{12} = d$ or $L_3 = 0$. The correct value is the one that minimizes $y_{\max}$ and therefore keeps all particle centers within the allowed region. Solving Eqns. (7.2) and (7.3) with these conditions yields, respectively,

$$
y_{\max} = \min\{2R - h, R + \sqrt{R^2 - \frac{d^2}{4}}\}
\tag{7.6}
$$

7.1.2   Case B $(h < d, x_3 < x_1 < x_2)$

When $h < d$, disk 3 may come into contact with either disk 1 or disk 2. In these cases, $n(h)$ must be split into parts and computed in a slightly different manner.

Three scenarios contribute to $n(h)$: $(x_3 < x_1 < x_2)$; $(x_1 < x_3 < x_2)$; $(x_1 < x_2 < x_3)$. The first and last of these scenarios are symmetric and contribute equally to $n(h)$. The second scenario is presented in sections 7.1.3 and 7.1.4.
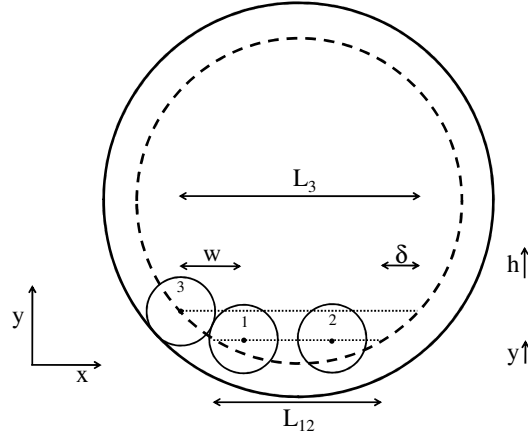
Figure 7.2: Case B.

For now, we consider only cases where the x-coordinate of disk 3 is not between those of disks 1 and 2. Such a case is shown in Fig. 7.2. As stated, there are equally as many states where $x_3 < x_1 < x_2$ as there are for $x_1 < x_2 < x_3$. Therefore, we will calculate the multiplicity for only the states where $x_3 < x_1 < x_2$, and finally multiply by two to obtain the contribution to $n(h)$. We define w as the minimum horizontal separation between disks 1 and 3, given by

$$w = \sqrt{d^2 - h^2} \tag{7.7}$$

The minimum horizontal separation between disks 1 and 2 remains d.

We also define a quantity $\delta = (L_3 - L_{12})/2$, as shown in Fig. 7.2. If we take the starting point of chord L_{12} to be 0, then the lower and upper bounds on x_3 are, respectively, $[-\delta, L_{12} - d - w]$. From Fig. 7.2, the limits of integration for x_2 are found to be $[x_1 + d, L_{12}]$ and those of x_1 are $[x_3 + w, L_{12} - d]$. Including the factor of 2 from the symmetric states, Eqn. (7.1) becomes

$$n_B \quad \propto \quad 2 \int\limits_{y_{\min}}^{y_{\max}} dy \int\limits_{(L_{12}-L_3)/2}^{L_{12}-d-w} dx_3 \int\limits_{x_3+w}^{L_{12}-d} dx_1 \int\limits_{x_1+d}^{L_{12}} dx_2$$

$$= \quad 2 \int\limits_{y_{\min}}^{y_{\max}} dy \ \left(\frac{1}{6}\right) \left(\frac{L_{12}+L_3}{2} - d - w\right)^3 \tag{7.8}$$

The limits of integration for y in this case are found from solving the equation

$$L_3 = w + d + \delta \tag{7.9}$$

which after substitution of the various terms yields a quadratic equation in y. The limits of integration for y are the roots of this equation, such that the minimum root is $y_{\min}$ and the maximum root is $y_{\max}$.

7.1.3 Case C $\left(\dfrac{\sqrt{3}d}{2} < h < d, x_1 < x_3 < x_2\right)$
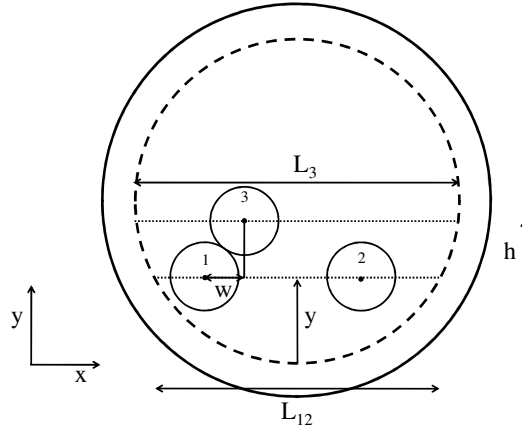
Figure 7.3: Case C.

Complementary to Case B, we now consider the case where $(x_1 < x_3 < x_2)$ and $\sqrt{3}d/2 < h < d$. As shown in Fig. 7.3, the minimum horizontal separation between disk 3 and one of the others is again w. Also, h is large enough that disks 1 and 2 may still contact, hence the minimum separation between disks 1 and 2 is d.

Proceeding as before, the limits of integration for x_1, x_2 and x_3 respectively are $[0, L_{12} - d]$, $[x_1 + d, L_{12}]$, and $[x_1 + w, x_2 - w]$. Eqn. (7.1) becomes

$$
\begin{aligned}
n_C \quad &\propto \quad \int\limits_{y_{\min}}^{y_{\max}} dy \int\limits_{0}^{L_{12}-d} dx_1 \int\limits_{x_1+d}^{L_{12}} dx_2 \int\limits_{x_1+w}^{x_2-w} dx_3 \\
&= \quad \int\limits_{y_{\min}}^{y_{\max}} dy \ (L_{12} - d)^2 \left[\frac{(L_{12} - d)}{6} - \left(w - \frac{d}{2} \right) \right]
\end{aligned}
$$

$$(7.10)$$

The lower and upper limits of y are found in the same way as in case A.

7.1.4   Case D $\left(0 \leq h \leq \sqrt{3}d/2, x_1 < x_3 < x_2 \right)$
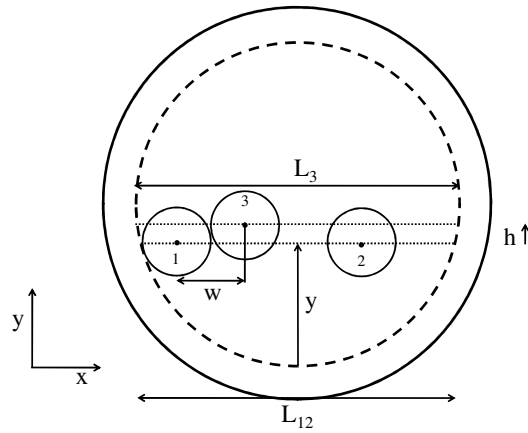
Figure 7.4: Case D.

The final case to be considered is also complementary to case B. In Fig. 7.4, disk 3 is again kept between 1 and 2, only now h is such that disks 1 and 2 never come into contact. The horizontal separation between 1 and 2 is always $\geq 2w$. Inspection again yields the limits for x_1, x_2, and x_3 which are $[0, L_{12} - 2w]$, $[x_3 + w, L_{12}]$, and $[x_1 + w, L_{12} - w]$. Therefore, Eqn. (7.1) becomes

$$n_D \quad \propto \quad \int_{y_{min}}^{y_{max}} dy \int_{0}^{L_{12}-2w} dx_1 \int_{x_1+w}^{L_{12}-w} dx_3 \int_{x_3+w}^{L_{12}} dx_2$$

$$= \int_{y_{min}}^{y_{max}} dy \left(\frac{1}{6}\right)(L_{12} - 2w)^3 \tag{7.11}$$

The lower limit y_{min} comes from geometry,

$$y_{min} = R - \sqrt{R^2 - w^2}, \tag{7.12}$$

while, similar to case A, the upper limit y_{max} is the minimum value corresponding to either $L_3 = 0$ or the maximum root of $L_{12} = 2w$,

$$y_{max} = \min\{2R - h, R + \sqrt{R^2 - w^2}\}. \tag{7.13}$$

Given the results of all four cases, the generalized method to compute $n(h)$ is given by

$$n(h) = \begin{cases} n_A, & h \geq d \\ n_B + n_C, & \sqrt{3}d/2 < h < d \\ n_B + n_D, & 0 \leq h \leq \sqrt{3}d/2 \end{cases} \tag{7.14}$$

In general, the integrand for each case above is a cumbersome function of h, thus we calculate $n(h)$ using numerical integration. From Eqn. (7.14), the origin of the kinks in $F(h)$ become more apparent as transitions from one solution regime to another. For $d = 2$, transition points occur at $h = \pm\sqrt{3}$ and $h = \pm 2$, as described in the text.

7.1.5 Behavior of $F_B(h)$ as $\epsilon \to 0$

To understand the growth of the energy barrier as $\epsilon \to 0$, we only need the result of Case D. Setting $h = 0$ gives $w = d$, and in the limit of small ϵ, transitions occur along

the diameter of the corral, which implies $L_{12} \approx 2d + 2\epsilon$. Eqn. (7.11) then becomes

$$n(h) \propto \int_{y_{\text{min}}}^{y_{\text{max}}} dy \ \left(\frac{4}{3}\right) \epsilon^3 \propto \epsilon^3 \Delta y \tag{7.15}$$

where

$$\Delta y = 2\sqrt{R^2 - d^2} = 2\sqrt{2d\epsilon + \epsilon^2}. \tag{7.16}$$

In the limit $\epsilon \to 0$, Δy grows as $\sqrt{\epsilon}$ and so $n(h) \propto \epsilon^{7/2}$. Therefore, the barrier height grows as

$$F_B \propto -\log n(h) \propto -\frac{7}{2} \ln \epsilon \tag{7.17}$$

as confirmed by the data shown in Fig. 4.4(d).

7.1.6   Barrier heights in θ

Here we give an explanation as to why $n(0) = 4n(\pi)$. Shown in Fig. 7.5 are configurations where $\theta \approx 0$ (top and middle) and $\theta \approx \pi$ (bottom). At first glance, it might appear that $n(0) = 2n(\pi)$, given that there are two configurations for $\theta \approx 0$ and only one for $\theta \approx \pi$. However, one must consider how the number of states changes in the vicinity of 0 and π. Thus we are interested in

$$\lim_{\delta\theta \to 0} \frac{n(\delta\theta)}{n(\pi - \delta\theta)} \tag{7.18}$$

In the top of Fig. 7.5, disks 1 and 2 are separated by an average distance s and disks 1 and 3 are separated by $2s$. The number of states where $\theta \approx 0$ is proportional to the product of the arc lengths subtended by $\delta\theta$ for disks 2 and 3. Therefore, for the top configuration, $n_{\text{top}} \propto (s\delta\theta)(2s\delta\theta) = 2s^2\delta\theta^2$. In the same way for the middle configuration, $n_{\text{mid}} = n_{\text{top}}$. Therefore, $n(\delta\theta) = 2n_{\text{top}} \propto 4s^2\delta\theta^2$. For the bottom configuration where $\theta \approx \pi$, the number

of states is again proportional to the product of the arc lengths, but in this case the distance between disks 1 and 3 and disks 1 and 2 is s. Therefore, $n(\pi - \delta\theta) = n_{\text{bot}} \propto s^2 \delta\theta^2$. Thus, the ratio in Eqn. (7.18) is equal to 4.
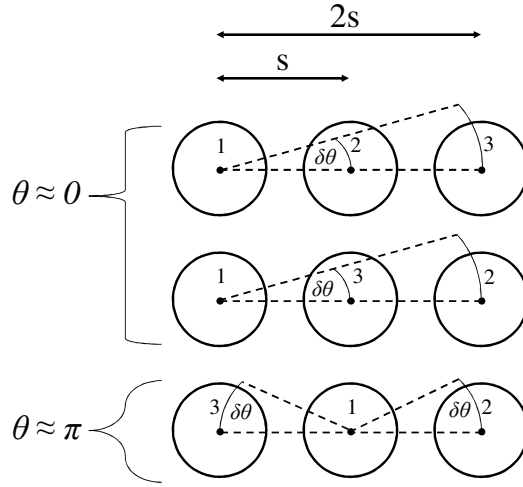
Figure 7.5: Configurations where $\theta \approx 0$ (top and middle) and $\theta \approx \pi$ (bottom). Arc lengths are proportional to the number of states $n(\delta\theta)$ and $n(\pi - \delta\theta)$.

7.2 Tracking Rotational Diffusion of Colloidal Clusters

Given a rotation matrix $\mathbf{R}$, one can calculate at each time the axis of rotation $\hat{\mathbf{u}}$ and angular displacement $\Delta\varphi$. In this notation, a rotational displacement can be described by a vector $\Delta\vec{\varphi} = \Delta\varphi\hat{\mathbf{u}}$, where $\hat{\mathbf{u}}$ has components in each of the Cartesian axes.

A single rotation will, by definition, have no effect on the direction of $\hat{\mathbf{u}}$, therefore,

$$\mathbf{R}\hat{\mathbf{u}} = \hat{\mathbf{u}}. \tag{7.19}$$

From Eq. (7.19), we see that the axis of rotation is an eigenvector of the matrix $\mathbf{R}$ with an eigenvalue of 1. For a set of rotational displacements $\{\mathbf{R}^k\}$, one may determine the axes of rotation by calculating the eigenvectors and eigenvalues of the rotation matrices, searching

for the eigenvalues equal to 1, and taking the corresponding eigenvectors.

To determine the size of the displacement about the axis of rotation, one defines an arbitrary vector $\hat{\mathbf{w}}$ perpendicular to $\hat{\mathbf{u}}$. For simplicity, we choose $\hat{\mathbf{w}}$ to be perpendicular to the x-axis (denoted by $\hat{\mathbf{i}}$),

$$\hat{\mathbf{w}} = \frac{\hat{\mathbf{u}} \times \hat{\mathbf{i}}}{|\hat{\mathbf{u}} \times \hat{\mathbf{i}}|}. \tag{7.20}$$

and apply the rotation matrix,

$$\mathbf{R}\hat{\mathbf{w}} = \hat{\mathbf{w}}'. \tag{7.21}$$

The magnitude of the displacement is the angle between $\hat{\mathbf{w}}$ and $\hat{\mathbf{w}}'$, and can be computed using the cross product relation

$$\sin(\Delta\varphi)\hat{\mathbf{u}} = \hat{\mathbf{w}} \times \hat{\mathbf{w}}'. \tag{7.22}$$

Calculating displacements relative to the axis of rotation always results in displacements greater than or equal to those measured relative to an arbitrary $\hat{\mathbf{p}}^0$. For example, measuring a diffusion coefficient of a spherically symmetric body with this method will yield a value that is a factor of $3/2$ of the actual diffusion coefficient in Eq. (5.20).

To understand the origin of this difference, consider the rotational axis $\hat{\mathbf{u}} = \hat{\mathbf{z}}$, a perpendicular vector $\hat{\mathbf{w}} = \hat{\mathbf{x}}$, and an arbitrary vector $\hat{\mathbf{p}}^0$ located at Cartesian coordinates $(\sin\theta, 0, \cos\theta)$, where θ is the spherical polar angle. If $\hat{\mathbf{w}}$ is rotated by an amount $\delta\varphi_u$, the angle between $\hat{\mathbf{w}}$ and $\hat{\mathbf{w}}'$ is identically $\delta\varphi_u$. However, the angle $\delta\varphi$ between $\hat{\mathbf{p}}$ and $\hat{\mathbf{p}}'$ can be shown to be

$$\delta\varphi = \cos^{-1}\left(\sin^2\theta\cos\delta\varphi_u + \cos^2\theta\right) \tag{7.23}$$

For small $\delta\varphi_u$, we can approximate $\delta\varphi$ as
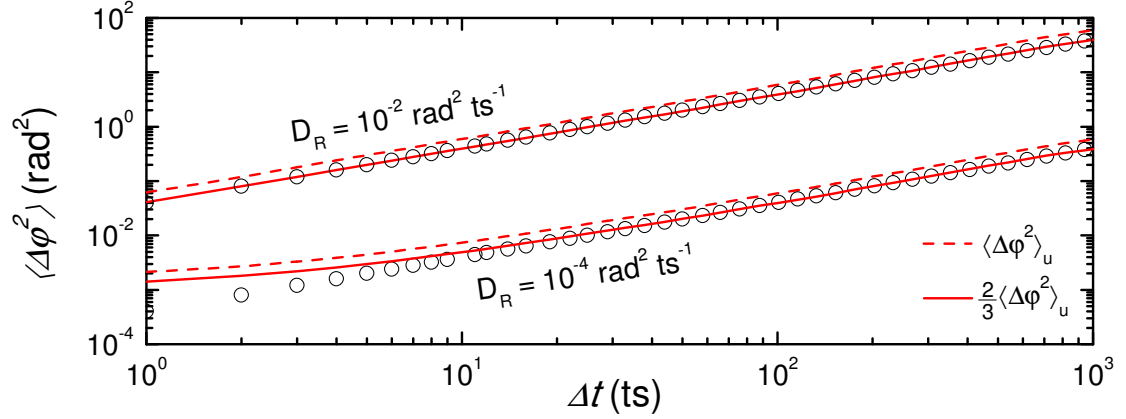
Figure 7.6: The MSADs of simulated pentahedra ($R = \sqrt{3}$ μm) with diffusion coefficients $D_R = 10^{-4}$ rad^2/ts and $D_R = 10^{-2}$ rad^2/ts and $\sigma_x = 50$ nm. Dashed lines show the uncorrected MSAD described below and solid lines are corrected data, obtained by multiplying the dashed lines by 2/3. Open circles are the theoretical MSAD from Eq. (5.20). We note that we have approximated diffusive motion by a single D_R for each pentahedron, as described in section 5.3.

$$1 - \delta\varphi^2 \approx \sin^2\theta \left(1 - \delta\varphi_u^2\right) + \left(1 - \sin^2\theta\right) \tag{7.24}$$

$$\delta\varphi^2 \approx \sin^2\theta\,\delta\varphi_u^2. \tag{7.25}$$

If an average of Eq. (7.25) is taken over spherical coordinates, we are left with an expression similar to an MSAD,

$$\langle\delta\varphi^2\rangle = \langle\sin^2\theta\rangle\langle\delta\varphi_u^2\rangle = \frac{2}{3}\langle\delta\varphi_u^2\rangle, \tag{7.26}$$

The factor of 2/3 arises for the same reasons in Perrin's original derivation of rotational diffusion [229]. Fig. 7.6 shows the MSADs measured in this way for two simulated pentahedral clusters, using a single diffusion constant for each. As stated, one can correct for the overestimation of motion by simply multiplying the MSAD by 2/3. The average

MSAD for any body can be corrected in the same manner, however we stress that this method returns only the average dynamics. While more direct than using an orientation vector, characterizing anisotropic bodies in this way will convolute motions about separate axes, and so will require some care when interpreting results.

Bibliography

[1] L. Marshall and C. F. Zukoski, "Experimental studies on the rheology of hard-sphere suspensions near the glass transition," *J. Phys. Chem.*, vol. 94, no. 3, pp. 1164–1171, 1990.

[2] Z. Cheng, J. Zhu, P. M. Chaikin, S.-E. Phan, and W. B. Russel, "Nature of the divergence in low shear viscosity of colloidal hard-sphere dispersions," *Phys. Rev. E*, vol. 65, no. 4, p. 041405, 2002.

[3] W. Gotze and L. Sjögren, "Relaxation processes in supercooled liquids," *Rep. Prog. Phys.*, vol. 55, no. 3, pp. 241–376, 1992.

[4] C. A. Angell, "Formation of glasses from liquids and biopolymers," *Science*, vol. 267, no. 5206, pp. 1924–1935, 1995.

[5] F. H. Stillinger, "A topographic view of supercooled liquids and glass formation," *Science*, vol. 267, no. 5206, pp. 1935–1939, 1995.

[6] M. D. Ediger, C. A. Angell, and S. R. Nagel, "Supercooled liquids and glasses," *J. Phys. Chem.*, vol. 100, no. 31, pp. 13200–13212, 1996.

[7] C. A. Angell, "Ten questions on glassformers, and a real space 'excitations' model

with some answers on fragility and phase transitions," *J. Phys.: Cond. Matt.*, vol. 12, no. 29, pp. 6463–6475, 2000.

[8] P. G. Debenedetti and F. H. Stillinger, "Supercooled liquids and the glass transition.," *Nature*, vol. 410, no. 6825, pp. 259–267, 2001.

[9] H. C. Andersen, "Molecular dynamics studies of heterogeneous dynamics and dynamic crossover in supercooled atomic liquids," *Proc. Nat. Acad. Sci.*, vol. 102, no. 19, pp. 6686–6691, 2005.

[10] H. M. Lindsay and P. M. Chaikin, "Elastic properties of colloidal crystals and glasses," *J. Chem. Phys.*, vol. 76, no. 7, pp. 3774–3781, 1982.

[11] E. D. Zanotto, "Do cathedral glasses flow?," *Am. J. Phys.*, vol. 66, no. 5, pp. 392–395, 1998.

[12] E. D. Zanotto and P. K. Gupta, "Do cathedral glasses flow?—Additional remarks," *Am. J. Phys.*, vol. 67, no. 3, pp. 260–262, 1999.

[13] R. Edgeworth, B. J. Dalton, and T. Parnell, "The pitch drop experiment," *Euro. J. Phys.*, vol. 5, no. 4, pp. 198–200, 1984.

[14] G. L. Hunter and E. R. Weeks, "The physics of the colloidal glass transition," *arXiv:1106.3581*, 2011.

[15] M. D. Ediger, C. A. Angell, and S. R. Nagel, "Supercooled liquids and glasses," *J. Phys. Chem.*, vol. 100, no. 31, pp. 13200–13212, 1996.

[16] C. A. Angell, K. L. Ngai, G. B. McKenna, P. F. McMillan, and S. W. Martin, "Relaxation in glass forming liquids and amorphous solids," *J. App. Phys.*, vol. 88, no. 6, pp. 3113–3157, 2000.

[17] J. D. Bernal, "The Bakerian lecture, 1962. The structure of liquids," *Proc. Roy. Soc. London. Series A*, vol. 280, no. 1382, pp. 299–322, 1964.

[18] H. Löwen, *Fun with Hard Spheres*, vol. 554, pp. 295–331. Berlin: Springer, 2000.

[19] A. Donev, F. H. Stillinger, and S. Torquato, "Configurational entropy of binary hard-disk glasses: Nonexistence of an ideal glass transition," *J. Chem. Phys.*, vol. 127, no. 12, p. 124509, 2007.

[20] W. W. Wood and J. D. Jacobson, "Preliminary results from a recalculation of the monte carlo equation of state of hard spheres," *J. Chem. Phys.*, vol. 27, no. 5, pp. 1207–1208, 1957.

[21] B. J. Alder and T. E. Wainwright, "Phase transition for a hard sphere system," *J. Chem. Phys.*, vol. 27, no. 5, pp. 1208–1209, 1957.

[22] W. G. Hoover and F. H. Ree, "Use of computer experiments to locate the melting transition and calculate the entropy in the solid phase," *J. Chem. Phys.*, vol. 47, no. 12, pp. 4873–4878, 1967.

[23] F. Sciortino, "Potential energy landscape description of supercooled liquids and glasses," *J. Stat. Mech.*, vol. 2005, no. 05, p. P05015, 2005.

[24] P. G. Bolhuis and D. A. Kofke, "Monte carlo study of freezing of polydisperse hard spheres," *Phys. Rev. E*, vol. 54, no. 1, pp. 634–643, 1996.

[25] S. Auer and D. Frenkel, "Suppression of crystal nucleation in polydisperse colloids due to increase of the surface free energy," *Nature*, vol. 413, no. 6857, pp. 711–713, 2001.

[26] H. J. Schope, G. Bryant, and W. van Megen, "Effect of polydispersity on the crystallization kinetics of suspensions of colloidal hard spheres when approaching the glass transition," *J. Chem. Phys.*, vol. 127, no. 8, p. 084505, 2007.

[27] E. Zaccarelli, C. Valeriani, E. Sanz, W. C. K. Poon, M. E. Cates, and P. N. Pusey, "Crystallization of Hard-Sphere glasses," *Phys. Rev. Lett.*, vol. 103, no. 13, p. 135704, 2009.

[28] P. N. Pusey, E. Zaccarelli, C. Valeriani, E. Sanz, W. C. K. Poon, and M. E. Cates, "Hard spheres: crystallization and glass formation," *Phil. Trans. Roy. Soc. A*, vol. 367, no. 1909, pp. 4993–5011, 2009.

[29] J. D. Bernal and J. Mason, "Packing of spheres: Co-ordination of randomly packed spheres," *Nature*, vol. 188, no. 4754, pp. 910–911, 1960.

[30] S. Torquato, T. M. Truskett, and P. G. Debenedetti, "Is random close packing of spheres well defined?," *Phys. Rev. Lett.*, vol. 84, no. 10, pp. 2064–2067, 2000.

[31] C. Radin, "Random close packing of granular matter," *J. Stat. Phys.*, vol. 131, no. 4, pp. 567–573, 2008.

[32] M. Hermes and M. Dijkstra, "Jamming of polydisperse hard spheres: The effect of kinetic arrest," *Europhys. Lett.*, vol. 89, no. 3, p. 38005, 2010.

[33] P. N. Pusey and W. van Megen, "Phase behaviour of concentrated suspensions of nearly hard colloidal spheres," *Nature*, vol. 320, no. 6060, pp. 340–342, 1986.

[34] P. N. Pusey and W. van Megen, "Observation of a glass transition in suspensions of spherical colloidal particles," *Phys. Rev. Lett.*, vol. 59, no. 18, pp. 2083–2086, 1987.

[35] G. Bryant, S. R. Williams, L. Qian, I. K. Snook, E. Perez, and F. Pincet, "How hard is a colloidal "hard-sphere" interaction?," *Phys. Rev. E*, vol. 66, no. 6, p. 060501, 2002.

[36] S. M. Underwood, J. R. Taylor, and W. van Megen, "Sterically stabilized colloidal particles as model hard spheres," *Langmuir*, vol. 10, no. 10, pp. 3550–3554, 1994.

[37] P. A. Hiltner and I. M. Krieger, "Diffraction of light by ordered suspensions," *J. Phys. Chem.*, vol. 73, no. 7, pp. 2386–2389, 1969.

[38] P. A. Hiltner, Y. S. Papir, and I. M. Krieger, "Diffraction of light by nonaqueous ordered suspensions," *J. Phys. Chem.*, vol. 75, no. 12, pp. 1881–1886, 1971.

[39] A. Kose, M. Ozaki, K. Takano, Y. Kobayashi, and S. Hachisu, "Direct observation of ordered latex suspension by metallurgical microscope," *J. Colloid Interf. Sci.*, vol. 44, no. 2, pp. 330–338, 1973.

[40] R. Hastings, "On the crystallization of macroionic solutions," *J. Chem. Phys.*, vol. 68, pp. 675–678, 1978.

[41] D. J. W. Aastuen, N. A. Clark, L. K. Cotter, and B. J. Ackerson, "Nucleation and growth of colloidal crystals," *Phys. Rev. Lett.*, vol. 57, no. 14, pp. 1733–1736, 1986.

[42] D. H. Van Winkle and C. A. Murray, "Layering transitions in colloidal crystals as observed by diffraction and direct-lattice imaging," *Phys. Rev. A*, vol. 34, no. 1, pp. 562–573, 1986.

[43] C. A. Murray and D. H. Van Winkle, "Experimental observation of two-stage melting in a classical two-dimensional screened coulomb system," *Phys. Rev. Lett.*, vol. 58, no. 12, pp. 1200–1203, 1987.

[44] E. B. Sirota, H. D. O. Yang, S. K. Sinha, P. M. Chaikin, J. D. Axe, and Y. Fujii, "Complete phase diagram of a charged colloidal system: A synchrotron x-ray scattering study," *Phys. Rev. Lett.*, vol. 62, no. 13, pp. 1524–1527, 1989.

[45] C. A. Murray, W. O. Sprenger, and R. A. Wenk, "Comparison of melting in three and two dimensions: Microscopy of colloidal spheres," *Phys. Rev. B*, vol. 42, no. 1, pp. 688–703, 1990.

[46] C. A. Murray and D. G. Grier, "Video microscopy of monodisperse colloidal systems," *Ann. Rev. Phys. Chem.*, vol. 47, pp. 421–462, 1996.

[47] R. O. Rosenberg, D. Thirumalai, and R. D. Mountain, "Liquid, crystalline and glassy states of binary charged colloidal suspensions," *J. Phys.: Cond. Matt.*, vol. 1, no. 11, p. 2109, 1989.

[48] P. N. Pusey, "The effect of polydispersity on the crystallization of hard spherical colloids," *J. Physique*, vol. 48, pp. 706–712, 1987.

[49] E. Bartsch, "Diffusion in concentrated colloidal suspensions and glasses," *Curr. Op. Coll. Int. Sci.*, vol. 3, no. 6, pp. 577–585, 1998.

[50] K. S. Schweizer and G. Yatsenko, "Collisions, caging, thermodynamics, and jamming in the barrier hopping theory of glassy hard sphere fluids," *J. Chem. Phys.*, vol. 127, no. 16, p. 164505, 2007.

[51] E. Di Cola, A. Moussaïd, M. Sztucki, T. Narayanan, and E. Zaccarelli, "Correlation between structure and rheology of a model colloidal glass," *J. Chem. Phys.*, vol. 131, no. 14, p. 144903, 2009.

[52] T. Gleim, W. Kob, and K. Binder, "How does the relaxation of a supercooled liquid

depend on its microscopic dynamics?," *Phys. Rev. Lett.*, vol. 81, no. 20, pp. 4404–4407, 1998.

[53] G. Szamel and E. Flenner, "Independence of the relaxation of a supercooled fluid from its microscopic dynamics: Need for yet another extension of the mode-coupling theory," *Europhys. Lett.*, vol. 67, no. 5, pp. 779–785, 2004.

[54] M. Tokuyama, H. Yamazaki, and Y. Terada, "Test of mean-field equations for two types of hard-sphere systems by a Brownian-dynamics simulation and a molecular-dynamics simulation," *Phys. Rev. E*, vol. 67, no. 6, p. 062403, 2003.

[55] M. Tokuyama, "Similarities in diversely different glass-forming systems," *Physica A*, vol. 378, no. 2, pp. 157–166, 2007.

[56] L. Berthier, G. Biroli, J. P. Bouchaud, W. Kob, K. Miyazaki, and D. R. Reichman, "Spontaneous and induced dynamic fluctuations in glass formers. I. general results and dependence on ensemble and dynamics," *J. Chem. Phys.*, vol. 126, no. 18, p. 184503, 2007.

[57] F. Höfling, T. Munk, E. Frey, and T. Franosch, "Critical dynamics of ballistic and Brownian particles in a heterogeneous environment," *J. Chem. Phys.*, vol. 128, no. 16, p. 164517, 2008.

[58] M. Fasolo and P. Sollich, "Equilibrium phase behavior of polydisperse hard spheres," *Phys. Rev. Lett.*, vol. 91, no. 6, p. 068301, 2003.

[59] P. Sollich and N. B. Wilding, "Crystalline phases of polydisperse spheres," *Phys. Rev. Lett.*, vol. 104, no. 11, p. 118302, 2010.

[60] S. I. Henderson, T. C. Mortensen, S. M. Underwood, and W. van Megen, "Effect

of particle size distribution on crystallisation and the glass transition of hard sphere colloids," *Physica A*, vol. 233, no. 1-2, pp. 102–116, 1996.

[61] S. I. Henderson and W. van Megen, "Metastability and crystallization in suspensions of mixtures of hard spheres," *Phys. Rev. Lett.*, vol. 80, no. 4, pp. 877–880, 1998.

[62] W. Kob and H. C. Andersen, "Testing mode-coupling theory for a supercooled binary Lennard-Jones mixture: The van hove correlation function," *Phys. Rev. E*, vol. 51, no. 5, pp. 4626–4641, 1995.

[63] W. Kob and H. C. Andersen, "Testing mode-coupling theory for a supercooled binary Lennard-Jones mixture. II. intermediate scattering function and dynamic susceptibility," *Phys. Rev. E*, vol. 52, no. 4, pp. 4134–4153, 1995.

[64] C. Alba-Simionesco, B. Coasne, G. Dosseh, G. Dudziak, K. E. Gubbins, R. Radhakrishnan, and M. Sliwinska-Bartkowiak, "Effects of confinement on freezing and melting," *J. Phys.: Cond. Matt.*, vol. 18, no. 6, pp. R15–R68, 2006.

[65] Y. Zhu and S. Granick, "Superlubricity: A paradox about confined fluids resolved," *Phys. Rev. Lett.*, vol. 93, no. 9, p. 096101, 2004.

[66] J. N. Israelachvili and P. M. McGuiggan, "Forces between surfaces in liquids," *Science*, vol. 241, no. 4867, pp. 795–800, 1988.

[67] T. R. Böhme and J. J. de Pablo, "Evidence for size-dependent mechanical properties from simulations of nanoscopic polymeric structures," *J. Chem. Phys.*, vol. 116, no. 22, pp. 9939–9951, 2002.

[68] M. P. Stoykovich, H. B. Cao, K. Yoshimoto, L. E. Ocola, and P. F. Nealey, "Deformation of nanoscopic polymer structures in response to well-defined capillary forces," *Adv. Mater.*, vol. 15, no. 14, pp. 1180–1184, 2003.

[69] M. Alcoutlabi and G. B. McKenna, "Effects of confinement on material behaviour at the nanometre size scale," *J. Phys.: Cond. Matt.*, vol. 17, no. 15, pp. R461–R524, 2005.

[70] D. Sappelt and J. Jackle, "The cooperativity length in models for the glass transition," *J. Phys. A: Mathematical and General*, vol. 26, no. 24, pp. 7325–7341, 1993.

[71] C. B. Roth and J. R. Dutcher, "Glass transition and chain mobility in thin polymer films," *J. Electroanalytical Chem.*, vol. 584, no. 1, pp. 13–22, 2005.

[72] C. L. Jackson and G. B. McKenna, "The glass transition of organic liquids confined to small pores," *J. Non-Cryst. Solids*, vol. 131-133, no. Part 1, pp. 221–224, 1991.

[73] G. Barut, P. Pissis, R. Pelster, and G. Nimtz, "Glass transition in liquids: Two versus Three-Dimensional confinement," *Phys. Rev. Lett.*, vol. 80, no. 16, pp. 3543–3546, 1998.

[74] J. Schüller, Y. Mel'nichenko, R. Richert, and E. W. Fischer, "Dielectric studies of the glass transition in porous media," *Phys. Rev. Lett.*, vol. 73, no. 16, pp. 2224–2227, 1994.

[75] D. Morineau, Y. Xia, and C. A. Simionesco, "Finite-size and surface effects on the glass transition of liquid toluene confined in cylindrical mesopores," *J. Chem. Phys.*, vol. 117, no. 19, pp. 8966–8972, 2002.

[76] K. L. Ngai, "Relaxation in nanometre-size polymers and glass formers: application of the coupling model to some current problems," *Phil. Mag. B*, vol. 82, pp. 291–303, 2002.

[77] C. J. Ellison and J. M. Torkelson, "The distribution of glass-transition temperatures in

nanoscopically confined glass formers," *Nature Materials*, vol. 2, no. 10, pp. 695–700, 2003.

[78] R. D. Priestley, C. J. Ellison, L. J. Broadbelt, and J. M. Torkelson, "Structural relaxation of polymer glasses at surfaces, interfaces, and in between," *Science*, vol. 309, no. 5733, pp. 456–459, 2005.

[79] C. B. Roth, K. L. McNerny, W. F. Jager, and J. M. Torkelson, "Eliminating the enhanced mobility at the free surface of polystyrene: fluorescence studies of the glass transition temperature in thin bilayer films of immiscible polymers," *Macromolecules*, vol. 40, no. 7, pp. 2568–2574, 2007.

[80] Z. T. Németh and H. Lowen, "Freezing and glass transition of hard spheres in cavities," *Phys. Rev. E*, vol. 59, no. 6, pp. 6824–6829, 1999.

[81] W. Kob, P. Scheidler, and K. Binder, "The relaxation dynamics of a simple glass former confined in a pore," *Europhys. Lett. (EPL)*, vol. 52, no. 3, pp. 277–283, 2000.

[82] F. He, L. M. Wang, and R. Richert, "Confined viscous liquids: Interfacial versus finite size effects," *Euro. Phys. J. - Special Topics*, vol. 141, no. 1, pp. 3–9, 2007.

[83] R. Richert, "Dynamics of nanoconfined supercooled liquids," *Ann. Rev. Phys. Chem.*, vol. 62, no. 1, pp. 65–84, 2011.

[84] J. E. Pye and C. B. Roth, "Two simultaneous mechanisms causing glass transition temperature reductions in high molecular weight freestanding polymer films as measured by transmission ellipsometry," *Phys. Rev. Lett.*, vol. 107, p. 235701, 2011.

[85] R. Richert, "Geometrical confinement and cooperativity in supercooled liquids studied by solvation dynamics," *Phys. Rev. B*, vol. 54, no. 22, pp. 15762–15766, 1996.

[86] K. Kim and R. Yamamoto, "Apparent finite-size effects in the dynamics of supercooled liquids," *Phys. Rev. E*, vol. 61, no. 1, pp. R41–R44, 2000.

[87] P. A. Thompson, G. S. Grest, and M. O. Robbins, "Phase transitions and universal dynamics in confined films," *Phys. Rev. Lett.*, vol. 68, no. 23, pp. 3448–3451, 1992.

[88] C. R. Nugent, K. V. Edmond, H. N. Patel, and E. R. Weeks, "Colloidal glass transition observed in confinement," *Phys. Rev. Lett.*, vol. 99, no. 2, p. 025702, 2007.

[89] P. S. Sarangapani and Y. Zhu, "Impeded structural relaxation of a hard-sphere colloidal suspension under confinement," *Phys. Rev. E*, vol. 77, no. 1, p. 010501, 2008.

[90] K. V. Edmond, C. R. Nugent, and E. R. Weeks, "Local influence of boundary conditions on a confined supercooled colloidal liquid," *Euro. Phys. J. - Special Topics*, vol. 189, no. 1, pp. 83–93, 2010.

[91] G. Goel, W. P. Krekelberg, J. R. Errington, and T. M. Truskett, "Tuning density profiles and mobility of inhomogeneous fluids," *Phys. Rev. Lett.*, vol. 100, no. 10, p. 106001, 2008.

[92] J. Mittal, T. M. Truskett, J. R. Errington, and G. Hummer, "Layering and Position-Dependent diffusive dynamics of confined fluids," *Phys. Rev. Lett.*, vol. 100, no. 14, p. 145901, 2008.

[93] W. C. K. Poon, E. R. Weeks, and C. P. Royall, "On measuring colloidal volume fractions," *Soft Matter*, vol. 8, no. 1, pp. 21–30, 2012.

[94] V. Prasad, D. Semwogerere, and E. R. Weeks, "Confocal microscopy of colloids," *J. Phys.: Cond. Matt.*, vol. 19, no. 11, p. 113102, 2007.

[95] P. Habdas and E. R. Weeks, "Video microscopy of colloidal suspensions and colloidal crystals," *Curr. Op. Coll. Int. Sci.*, vol. 7, no. 3-4, pp. 196–203, 2002.

[96] A. Draaijer and P. M. Houpt, "Standard video-rate confocal laser-scanning reflection and fluorescence microscope," *Scanning*, vol. 10, no. 4, pp. 139–145, 1988.

[97] D. Awamura, T. Ode, and M. Yonezawa, "A real time confocal microscope," in *3D Dynamic Morphometry for Bridge between Structure and Function Proceedings of the Second International Symposium for Science on Form* (S. Ishizaka, ed.), Science on Form, pp. 81–95, KTK Scientific Publishers, Tokyo, 1990.

[98] J. C. Crocker and D. G. Grier, "When like charges attract: The effects of geometrical confinement on Long-Range colloidal interactions," *Phys. Rev. Lett.*, vol. 77, no. 9, pp. 1897–1900, 1996.

[99] E. R. Weeks and J. C. Crocker, "Particle tracking using IDL: website." http://www.physics.emory.edu/∼weeks/idl/.

[100] J. C. Crocker, J. A. Matteo, A. D. Dinsmore, and A. G. Yodh, "Entropic attraction and repulsion in binary colloids probed with a line optical tweezer," *Phys. Rev. Lett.*, vol. 82, no. 21, pp. 4352–4355, 1999.

[101] J. Baumgartl and C. Bechinger, "On the limits of digital video microscopy," *Europhys. Lett.*, vol. 71, pp. 487–493, 2005.

[102] E. R. Weeks and D. A. Weitz, "Properties of cage rearrangements observed near the colloidal glass transition," *Phys. Rev. Lett.*, vol. 89, no. 9, p. 095704, 2002.

[103] S. Inoué and K. R. Spring, *Video Microscopy : The Fundamentals (The Language of Science)*. Springer, 2nd ed., 1997.

[104] M. C. Jenkins and S. U. Egelhaaf, "Confocal microscopy of colloidal particles: Towards reliable, optimum coordinates," *Adv. Coll. Int. Sci.*, vol. 136, no. 1-2, pp. 65–92, 2008.

[105] W. Sutherland, "A dynamical theory of diffusion for non-electrolytes and the molecular mass of albumin," *Phil. Mag.*, vol. 9, pp. 781–785, 1905.

[106] A. Einstein, "On the movement of small particles suspended in a stationary liquid demanded by the molecular-kinetic theory of heat," *Annalen der Physik (Leipzig)*, vol. 17, pp. 549–560, 1905.

[107] P. N. Pusey and R. J. A. Tough, "Hydrodynamic interactions and diffusion in concentrated particle suspensions," *Faraday Discuss. Chem. Soc.*, vol. 76, pp. 123–136, 1983.

[108] I. Snook, W. van Megen, and R. J. A. Tough, "Diffusion in concentrated hard sphere dispersions: Effective two particle mobility tensors," *J. Chem. Phys.*, vol. 78, no. 9, pp. 5825–5836, 1983.

[109] C. W. J. Beenakker and P. Mazur, "Diffusion of spheres in a concentrated suspension: Resummation of many-body hydrodynamic interactions," *Physics Letters A*, vol. 98, no. 1-2, pp. 22–24, 1983.

[110] C. W. J. Beenakker and P. Mazur, "Diffusion of spheres in a concentrated suspension II," *Physica A*, vol. 126, no. 3, pp. 349–370, 1984.

[111] W. van Megen, R. H. Ottewill, S. M. Owens, and P. N. Pusey, "Measurement of the wave-vector dependent diffusion coefficient in concentrated particle dispersions," *J. Chem. Phys.*, vol. 82, no. 1, pp. 508–515, 1985.

[112] B. J. Berne, J. P. Boon, and S. A. Rice, "On the calculation of autocorrelation functions of dynamical variables," *J. Chem. Phys.*, vol. 45, no. 4, pp. 1086–1096, 1966.

[113] L. Sjögren, "Numerical results on the density fluctuations in liquid rubidium," *Phys. Rev. A*, vol. 22, pp. 2883–2890, 1980.

[114] G. Wahnstrom and L. Sjögren, "Incoherent scattering function in simple classical liquids," *J. Phys. C*, vol. 15, no. 3, p. 401, 1982.

[115] E. Rabani, J. D. Gezelter, and B. J. Berne, "Calculating the hopping rate for self-diffusion on rough potential energy surfaces: Cage correlations," *J. Chem. Phys.*, vol. 107, no. 17, pp. 6867–6876, 1997.

[116] R. Verberg, I. M. D. Schepper, and E. G. D. Cohen, "Theory of long-time wave number dependent diffusion coefficients in concentrated neutral colloidal suspensions," *Europhys. Lett.*, pp. 397–402, 1999.

[117] K. S. Schweizer and E. J. Saltzman, "Entropic barriers, activated hopping, and the glass transition in colloidal suspensions," *J. Chem. Phys.*, vol. 119, no. 2, pp. 1181–1196, 2003.

[118] J. S. Sharp and J. A. Forrest, "Free surfaces cause reductions in the glass transition temperature of thin polystyrene films," *Phys. Rev. Lett.*, vol. 91, no. 23, p. 235701, 2003.

[119] P. G. de Gennes, "Glass transitions in thin polymer films," *Euro. Phys. J. E: Soft Matter and Biological Physics*, vol. 2, no. 3, pp. 201–205, 2000.

[120] S. Kim, S. A. Hewlett, C. B. Roth, and J. M. Torkelson, "Confinement effects on glass transition temperature, transition breadth, and expansivity: Comparison of ellipsometry and fluorescence measurements on polystyrene films," *Euro. Phys. J. E: Soft Matter and Biological Physics*, vol. 30, no. 1, pp. 83–92, 2009.

[121] J. E. Pye, K. A. Rohald, E. A. Baker, and C. B. Roth, "Physical aging in ultrathin polystyrene films: Evidence of a gradient in dynamics at the free surface and its connection to the glass transition temperature reductions," *Macromolecules*, vol. 43, no. 19, pp. 8296–8303, 2010.

[122] K. Paeng, R. Richert, and M. D. Ediger, "Molecular mobility in supported thin films of polystyrene, poly(methyl methacrylate), and poly(2-vinyl pyridine) probed by dye reorientation," *Soft Matter*, vol. 8, no. 3, pp. 819–826, 2012.

[123] C. B. Roth and J. R. Dutcher, "Glass transition temperature of freely-standing films of atactic poly(methyl methacrylate)," *Euro. Phys. J. E: Soft Matter and Biological Physics*, vol. 12, no. 0, pp. 103–107, 2003.

[124] C. B. Roth, A. Pound, S. W. Kamp, C. A. Murray, and J. R. Dutcher, "Molecular-weight dependence of the glass transition temperature of freely-standing poly(methyl methacrylate) films," *Euro. Phys. J. E: Soft Matter and Biological Physics*, vol. 20, no. 4, pp. 441–448, 2006.

[125] C. Zhang, Y. Guo, and R. D. Priestley, "Glass transition temperature of polymer nanoparticles under soft and hard confinement," *Macromolecules*, vol. 44, no. 10, pp. 4001–4006, 2011.

[126] Y. Guo, C. Zhang, C. Lai, R. D. Priestley, M. D'Acunzi, and G. Fytas, "Structural relaxation of polymer nanospheres under soft and hard confinement: Isobaric versus isochoric conditions," *ACS Nano*, vol. 5, no. 7, pp. 5365–5373, 2011.

[127] A. Yethiraj and A. van Blaaderen, "A colloidal model system with an interaction tunable from hard sphere to soft and dipolar," *Nature*, vol. 421, no. 6922, pp. 513–517, 2003.

[128] M. E. Leunissen, A. van Blaaderen, A. D. Hollingsworth, M. T. Sullivan, and P. M. Chaikin, "Electrostatics at the oil-water interface, stability, and order in emulsions and colloids," *Proc. Nat. Acad. Sci.*, vol. 104, no. 8, pp. 2585–2590, 2007.

[129] B. J. Park, J. P. Pantina, E. M. Furst, M. Oettel, S. Reynaert, and J. Vermant, "Direct measurements of the effects of salt and surfactant on interaction forces between colloidal particles at WaterOil interfaces," *Langmuir*, vol. 24, no. 5, pp. 1686–1694, 2008.

[130] G. L. Hunter, K. V. Edmond, M. T. Elsesser, and E. R. Weeks, "Tracking rotational diffusion of colloidal clusters," *Opt. Express*, vol. 19, no. 18, pp. 17189–17202, 2011.

[131] C. R. Nugent, K. V. Edmond, H. N. Patel, and E. R. Weeks, "Colloidal glass transition observed in confinement," *Phys. Rev. Lett.*, vol. 99, no. 2, p. 025702, 2007.

[132] K. V. Edmond, C. R. Nugent, and E. R. Weeks, "Influence of confinement on dynamical heterogeneities in dense colloidal samples," *arXiv:1003.0856*, 2010.

[133] J. Mittal, V. K. Shen, J. R. Errington, and T. M. Truskett, "Confinement, entropy, and single-particle dynamics of equilibrium hard-sphere mixtures," *J. Chem. Phys.*, vol. 127, no. 15, p. 154513, 2007.

[134] J. Mittal, J. R. Errington, and T. M. Truskett, "Does confining the hard-sphere fluid between hard walls change its average properties?," *J. Chem. Phys.*, vol. 126, no. 24, pp. 244708–244715, 2007.

[135] K. W. Desmond and E. R. Weeks, "Random close packing of disks and spheres in confined geometries," *Phys. Rev. E*, vol. 80, no. 5, p. 051305, 2009.

[136] P. Scheidler, W. Kob, and K. Binder, "Cooperative motion and growing length scales in supercooled confined liquids," *Europhys. Lett.*, vol. 59, no. 5, pp. 701–707, 2002.

[137] E. R. Weeks, J. C. Crocker, A. C. Levitt, A. Schofield, and D. A. Weitz, "Three-Dimensional direct imaging of structural relaxation near the colloidal glass transition," *Science*, vol. 287, no. 5453, pp. 627–631, 2000.

[138] E. R. Weeks, J. C. Crocker, and D. A. Weitz, "Short- and long-range correlated motion observed in colloidal glasses and liquids," *J. Phys.: Cond. Matt.*, vol. 19, no. 20, p. 205131, 2007.

[139] M. Goldstein, "Viscous liquids and the glass transition: A potential energy barrier picture," *J. Chem. Phys.*, vol. 51, no. 9, pp. 3728–3739, 1969.

[140] F. H. Stillinger, "A topographic view of supercooled liquids and glass formation," *Science*, vol. 267, no. 5206, pp. 1935–1939, 1995.

[141] S. Sastry, P. G. Debenedetti, and F. H. Stillinger, "Signatures of distinct dynamical regimes in the energy landscape of a glass-forming liquid," *Nature*, vol. 393, no. 6685, pp. 554–557, 1998.

[142] C. Dasgupta and O. T. Valls, "Free energy landscape of a dense hard-sphere system," *Phys. Rev. E*, vol. 59, no. 3, pp. 3123–3134, 1999.

[143] C. Dasgupta and O. T. Valls, "Free-energy landscape of simple liquids near the glass transition," *J. Phys.: Cond. Matt.*, vol. 12, no. 29, p. 6553, 2000.

[144] T. B. Schrøder, S. Sastry, J. C. Dyre, and S. C. Glotzer, "Crossover to potential energy landscape dominated dynamics in a model glass-forming liquid," *J. Chem. Phys.*, vol. 112, no. 22, pp. 9834–9840, 2000.

[145] S. Sastry, "The relationship between fragility, configurational entropy and the potential energy landscape of glass-forming liquids," *Nature*, vol. 409, no. 6817, pp. 164–167, 2001.

[146] T. S. Grigera, A. Cavagna, I. Giardina, and G. Parisi, "Geometric approach to the dynamic glass transition," *Phys. Rev. Lett.*, vol. 88, no. 5, p. 055502, 2002.

[147] K. Kim and T. Munakata, "Glass transition of hard sphere systems: Molecular dynamics and density functional theory," *Phys. Rev. E*, vol. 68, no. 2, p. 021502, 2003.

[148] M. Vogel, B. Doliwa, A. Heuer, and S. C. Glotzer, "Particle rearrangements during transitions between local minima of the potential energy landscape of a binary Lennard-Jones liquid," *J. Chem. Phys.*, vol. 120, no. 9, pp. 4404–4414, 2004.

[149] K. S. Schweizer and E. J. Saltzman, "Entropic barriers, activated hopping, and the glass transition in colloidal suspensions," *J. Chem. Phys.*, vol. 119, no. 2, pp. 1181–1196, 2003.

[150] S. Jabbari-Farouji, G. H. Wegdam, and D. Bonn, "Gels and glasses in a single system: Evidence for an intricate Free-Energy landscape of glassy materials," *Phys. Rev. Lett.*, vol. 99, no. 6, p. 065701, 2007.

[151] W. Kauzmann, "The nature of the glassy state and the behavior of liquids at low temperatures," *Chem. Rev.*, vol. 43, no. 2, pp. 219–256, 1948.

[152] P. G. Debenedetti and F. H. Stillinger, "Supercooled liquids and the glass transition.," *Nature*, vol. 410, no. 6825, pp. 259–267, 2001.

[153] D. J. Wales, *Energy Landscapes: Applications to Clusters, Biomolecules and Glasses (Cambridge Molecular Science)*. Cambridge University Press, 1 ed., 2004.

[154] J. S. van Duijneveldt and D. Frenkel, "Computer simulation study of free energy barriers in crystal nucleation," *J. Chem. Phys.*, vol. 96, no. 6, pp. 4655–4668, 1992.

[155] P. R. ten Wolde, M. J. Ruiz Montero, and D. Frenkel, "Numerical calculation of the rate of crystal nucleation in a Lennard-Jones system at moderate undercooling," *J. Chem. Phys.*, vol. 104, no. 24, pp. 9932–9947, 1996.

[156] P. R. ten Wolde and D. Frenkel, "Enhancement of protein crystal nucleation by critical density fluctuations," *Science*, vol. 277, pp. 1975–1978, 1997.

[157] A. Heuer, "Properties of a Glass-Forming system as derived from its potential energy landscape," *Phys. Rev. Lett.*, vol. 78, pp. 4051–4054, 1997.

[158] S. V. Krivov and M. Karplus, "Hidden complexity of free energy surfaces for peptide (protein) folding," *Proc. Nat. Acad. Sci.*, vol. 101, no. 41, pp. 14766–14770, 2004.

[159] A. Altis, M. Otten, P. H. Nguyen, R. Hegger, and G. Stock, "Construction of the free energy landscape of biomolecules via dihedral angle principal component analysis," *J. Chem. Phys.*, vol. 128, no. 24, p. 245102, 2008.

[160] G. G. Maisuradze, A. Liwo, and H. A. Scheraga, "How adequate are one- and Two-Dimensional free energy landscapes for protein folding dynamics?," *Phys. Rev. Lett.*, vol. 102, no. 23, p. 238102, 2009.

[161] M. A. Bevan, "Free energy landscapes for colloidal crystal assembly," *Soft Matter*, vol. 7, no. 7, pp. 3280–3285, 2011.

[162] R. J. Speedy, "Two disks in a box," *Physica A*, vol. 210, pp. 341–351, 1994.

[163] R. K. Bowles and R. J. Speedy, "Five discs in a box," *Physica A*, vol. 262, no. 1-2, pp. 76–87, 1999.

[164] K. S. Schweizer and E. J. Saltzman, "Activated hopping, barrier fluctuations, and

heterogeneity in glassy suspensions and liquids†," *J. Phys. Chem. B*, vol. 108, no. 51, pp. 19729–19741, 2004.

[165] W. Gotze and L. Sjögren, "Relaxation processes in supercooled liquids," *Rep. Prog. Phys.*, vol. 55, no. 3, pp. 241–376, 1992.

[166] B. Doliwa and A. Heuer, "Cage effect, local anisotropies, and dynamic heterogeneities at the glass transition: A computer study of hard spheres," *Phys. Rev. Lett.*, vol. 80, no. 22, pp. 4915–4918, 1998.

[167] E. R. Weeks and D. A. Weitz, "Subdiffusion and the cage effect studied near the colloidal glass transition," *Chem. Phys.*, vol. 284, no. 1-2, pp. 361–367, 2002.

[168] K. Vollmayr-Lee, "Single particle jumps in a binary Lennard-Jones system below the glass transition," *J. Chem. Phys.*, vol. 121, no. 10, pp. 4781–4794, 2004.

[169] S. I. Sirono, "Binary mixture of hard disks as a model glass former: Caging and uncaging," *Phys. Rev. B*, vol. 84, p. 104201, 2011.

[170] V. K. de Souza and D. J. Wales, "Energy landscapes for diffusion: Analysis of cage-breaking processes," *J. Chem. Phys.*, vol. 129, no. 16, p. 164507, 2008.

[171] P. Pal, C. S. O'Hern, J. Blawzdziewicz, E. R. Dufresne, and R. Stinchcombe, "Minimal model for kinetic arrest," *Phys. Rev. E*, vol. 78, no. 1, p. 011111, 2008.

[172] B. J. Alder, W. G. Hoover, and T. E. Wainwright, "Cooperative motion of hard disks leading to melting," *Phys. Rev. Lett.*, vol. 11, no. 6, pp. 241–243, 1963.

[173] G. Adam and J. H. Gibbs, "On the temperature dependence of cooperative relaxation properties in Glass-Forming liquids," *J. Chem. Phys.*, vol. 43, no. 1, pp. 139–146, 1965.

[174] C. Donati, J. F. Douglas, W. Kob, S. J. Plimpton, P. H. Poole, and S. C. Glotzer, "Stringlike cooperative motion in a supercooled liquid," *Phys. Rev. Lett.*, vol. 80, no. 11, pp. 2338–2341, 1998.

[175] A. H. Marcus, J. Schofield, and S. A. Rice, "Experimental observations of non-Gaussian behavior and stringlike cooperative dynamics in concentrated quasi-two-dimensional colloidal liquids," *Phys. Rev. E*, vol. 60, no. 5, pp. 5725–5736, 1999.

[176] B. Doliwa and A. Heuer, "Cooperativity and spatial correlations near the glass transition: Computer simulation results for hard spheres and disks," *Phys. Rev. E*, vol. 61, no. 6, pp. 6898–6908, 2000.

[177] M. D. Ediger, "Spatially heterogeneous dynamics in supercooled liquids," *Ann. Rev. Phys. Chem.*, vol. 51, no. 1, pp. 99–128, 2000.

[178] R. Richert, "Heterogeneous dynamics in liquids: fluctuations in space and time," *J. Phys.: Cond. Matt.*, vol. 14, no. 23, pp. R703–R738, 2002.

[179] H. Sillescu, "Heterogeneity at the glass transition: a review," *J. Non-Cryst. Solids*, vol. 243, no. 2-3, pp. 81–108, 1999.

[180] T. Odagaki, T. Yoshidome, A. Koyama, and A. Yoshimori, "Free energy landscape approach to glass transition," *J. Non-Cryst. Solids*, vol. 352, no. 42-49, pp. 4843–4846, 2006.

[181] T. Yoshidome, A. Yoshimori, and T. Odagaki, "Free energy landscape and cooperatively rearranging region in a hard sphere glass," *Phys. Rev. E*, vol. 76, no. 2, p. 021506, 2007.

[182] T. Yoshidome, T. Odagaki, and A. Yoshimori, "Free-energy landscape for a tagged particle in a dense hard-sphere fluid," *Phys. Rev. E*, vol. 77, p. 061503, 2008.

[183] S. Büchner and A. Heuer, "Metastable states as a key to the dynamics of supercooled liquids," *Phys. Rev. Lett.*, vol. 84, no. 10, pp. 2168–2171, 2000.

[184] P. N. Pusey, P. N. Segrè, O. P. Behrend, S. Meeker, and W. C. K. Poon, "Dynamics of concentrated colloidal suspensions," *Physica A*, vol. 235, no. 1-2, pp. 1–8, 1997.

[185] P. N. Pusey, "Colloidal glasses," *J. Phys.: Cond. Matt.*, vol. 20, no. 49, p. 494202, 2008.

[186] G. C. Cianci, R. E. Courtland, and E. R. Weeks, "Correlations of structure and dynamics in an aging colloidal glass," *Solid State Comm.*, vol. 139, pp. 599–604, 2006.

[187] A. van Blaaderen and P. Wiltzius, "Real-Space structure of colloidal Hard-Sphere glasses," *Science*, vol. 270, no. 5239, pp. 1177–1179, 1995.

[188] D. Frenkel and B. Smit, *Understanding Molecular Simulation, Second Edition: From Algorithms to Applications (Computational Science)*. Academic Press, 2 ed., 2001.

[189] While $n(h)$ should have mirror symmetry about the line $h = 0$, an artifact of the finite number of Monte Carlo steps is that directly computed distributions may show slight unphysical biases toward either side of $h = 0$. Though small, we eliminate these biases by averaging one side of a histogram with the mirror image of the other.

[190] H. Kramers, "Brownian motion in a field of force and the diffusion model of chemical reactions," *Physica*, vol. 7, no. 4, pp. 284–304, 1940.

[191] P. Hänggi, P. Talkner, and M. Borkovec, "Reaction-rate theory: fifty years after kramers," *Reviews of Modern Physics*, vol. 62, no. 2, pp. 251–341, 1990.

[192] C. Gardiner, *Handbook of Stochastic Methods: for Physics, Chemistry and the Natural Sciences (Springer Series in Synergetics)*. Springer, 3rd ed., 2004.

[193] We currently do not have a method to analytically calculate $F(\theta)$. Each curve in Fig. 4.9(a) was generated by computing $F(\theta)$ from 10^{10} configurations of three disks placed randomly in the corral and then using Eqn. (4.4).

[194] P. Germain, J. G. Malherbe, and S. Amokrane, "When mixtures of hard-sphere-like colloids do not behave as mixtures of hard spheres," *Phys. Rev. E*, vol. 70, p. 041409, 2004.

[195] K. Vollmayr-Lee, W. Kob, K. Binder, and A. Zippelius, "Dynamical heterogeneities below the glass transition," *J. Chem. Phys.*, vol. 116, no. 12, pp. 5158–5166, 2002.

[196] K. V. Edmond, H. Park, M. T. Elsesser, G. L. Hunter, D. J. Pine, and E. R. Weeks, "Tracking the Brownian diffusion of a colloidal tetrahedral cluster," *Chaos: An Interdisciplinary Journal of Nonlinear Science*, vol. 21, no. 4, p. 041103, 2011.

[197] K. V. Edmond, M. T. Elsesser, G. L. Hunter, D. J. Pine, and E. R. Weeks, "Decoupling of rotational and translational diffusion in supercooled colloidal fluids," *submitted to Proc. Natl. Acad. Sci.*, 2012.

[198] P. N. Pusey and W. van Megen, "Phase behaviour of concentrated suspensions of nearly hard colloidal spheres," *Nature*, vol. 320, no. 6060, pp. 340–342, 1986.

[199] P. N. Pusey, W. C. K. Poon, S. M. Ilett, and P. Bartlett, "Phase behaviour and structure of colloidal suspensions," *J. Phys.: Cond. Matt.*, vol. 6, no. 23A, pp. A29–A36, 1994.

[200] J. R. Savage, D. W. Blair, A. J. Levine, R. A. Guyer, and A. D. Dinsmore, "Imag-

ing the sublimation dynamics of colloidal crystallites," *Science*, vol. 314, no. 5800, pp. 795–798, 2006.

[201] D. G. Grier and C. A. Murray, "The microscopic dynamics of freezing in supercooled colloidal fluids," *J. Chem. Phys.*, vol. 100, no. 12, pp. 9088–9095, 1994.

[202] U. Gasser, E. R. Weeks, A. Schofield, P. N. Pusey, and D. A. Weitz, "Real-Space imaging of nucleation and growth in colloidal crystallization," *Science*, vol. 292, no. 5515, pp. 258–262, 2001.

[203] J. Hernández-Guzmán and E. R. Weeks, "The equilibrium intrinsic crystal-liquid interface of colloids," *Proc. Nat. Acad. Sci.*, vol. 106, no. 36, pp. 15198–15202, 2009.

[204] J. C. Crocker and D. G. Grier, "Methods of digital video microscopy for colloidal studies," *J. Colloid Interf. Sci.*, vol. 179, no. 1, pp. 298–310, 1996.

[205] A. D. Dinsmore, E. R. Weeks, V. Prasad, A. C. Levitt, and D. A. Weitz, "Three-Dimensional confocal microscopy of colloids," *Appl. Opt.*, vol. 40, no. 24, pp. 4152–4159, 2001.

[206] E. R. Dufresne, T. M. Squires, M. P. Brenner, and D. G. Grier, "Hydrodynamic coupling of two Brownian spheres to a planar surface," *Phys. Rev. Lett.*, vol. 85, no. 15, pp. 3317–3320, 2000.

[207] R. Besseling, E. R. Weeks, A. B. Schofield, and W. C. K. Poon, "Three-Dimensional imaging of colloidal glasses under steady shear," *Phys. Rev. Lett.*, vol. 99, no. 2, p. 028301, 2007.

[208] P. Schall, D. A. Weitz, and F. Spaepen, "Structural rearrangements that govern flow in colloidal glasses," *Science*, vol. 318, no. 5858, pp. 1895–1899, 2007.

[209] D. Chen, D. Semwogerere, J. Sato, V. Breedveld, and E. R. Weeks, "Microscopic structural relaxation in a sheared supercooled colloidal liquid," *Phys. Rev. E*, vol. 81, no. 1, p. 011403, 2010.

[210] S. Martin, M. Reichert, H. Stark, and T. Gisler, "Direct observation of hydrodynamic Rotation-Translation coupling between two colloidal spheres," *Phys. Rev. Lett.*, vol. 97, no. 24, p. 248301, 2006.

[211] S. M. Anthony, L. Hong, M. Kim, and S. Granick, "Single-Particle colloid tracking in four dimensions," *Langmuir*, vol. 22, no. 24, pp. 9812–9815, 2006.

[212] P. J. Yunker, K. Chen, Z. Zhang, W. G. Ellenbroek, A. J. Liu, and A. G. Yodh, "Rotational and translational phonon modes in glasses composed of ellipsoidal particles," *Phys. Rev. E*, vol. 83, no. 1, p. 011403, 2011.

[213] L. Hong, S. M. Anthony, and S. Granick, "Rotation in suspension of a Rod-Shaped colloid," *Langmuir*, vol. 22, no. 17, pp. 7128–7131, 2006.

[214] Y. Han, A. M. Alsayed, M. Nobili, J. Zhang, T. C. Lubensky, and A. G. Yodh, "Brownian motion of an ellipsoid," *Science*, vol. 314, no. 5799, pp. 626–630, 2006.

[215] D. Mukhija and M. J. Solomon, "Translational and rotational dynamics of colloidal rods by direct visualization with confocal microscopy," *J. Colloid Interf. Sci.*, vol. 314, no. 1, pp. 98–106, 2007.

[216] V. N. Manoharan, M. T. Elsesser, and D. J. Pine, "Dense packing and symmetry in small clusters of microspheres," *Science*, vol. 301, no. 5632, pp. 483–487, 2003.

[217] M. T. Elsesser, A. D. Hollingsworth, K. V. Edmond, and D. J. Pine, "Large Core-Shell poly(methyl methacrylate) colloidal clusters: Synthesis, characterization, and tracking," *Langmuir*, vol. 27, no. 3, pp. 917–927, 2011.

[218] A. van Blaaderen, "Chemistry: Colloidal molecules and beyond," *Science*, vol. 301, no. 5632, pp. 470–471, 2003.

[219] A. van Blaaderen, "Materials science: Colloids get complex," *Nature*, vol. 439, no. 7076, pp. 545–546, 2006.

[220] S. C. Glotzer and M. J. Solomon, "Anisotropy of building blocks and their assembly into complex structures," *Nature Materials*, vol. 6, no. 8, pp. 557–562, 2007.

[221] S. M. Anthony, M. Kim, and S. Granick, "Translation-rotation decoupling of colloidal clusters of various symmetries," *J. Chem. Phys.*, vol. 129, no. 24, p. 244701, 2008.

[222] J. Challis, "A procedure for determining rigid body transformation parameters," *J. Biomech.*, vol. 28, no. 6, pp. 733–737, 1995.

[223] M. G. Mazza, N. Giovambattista, F. W. Starr, and H. E. Stanley, "Relation between rotational and translational dynamic heterogeneities in water," *Phys. Rev. Lett.*, vol. 96, no. 5, p. 057803, 2006.

[224] M. G. Mazza, N. Giovambattista, H. E. Stanley, and F. W. Starr, "Connection of translational and rotational dynamical heterogeneities with the breakdown of the Stokes-Einstein and Stokes-Einstein-Debye relations in water," *Phys. Rev. E*, vol. 76, no. 3, p. 031203, 2007.

[225] S. Kämmerer, W. Kob, and R. Schilling, "Dynamics of the rotational degrees of freedom in a supercooled liquid of diatomic molecules," *Phys. Rev. E*, vol. 56, no. 5, pp. 5450–5461, 1997.

[226] B. J. Berne, P. Pechukas, and G. D. Harp, "Molecular reorientation in liquids and gases," *J. Chem. Phys.*, vol. 49, pp. 3125–3129, 1968.

[227] G. Williams, "Time-correlation functions and molecular motions," *Chem. Soc. Rev.*, vol. 7, pp. 89–131, 1978.

[228] M. Hoffmann, C. S. Wagner, L. Harnau, and A. Wittemann, "3D Brownian diffusion of Submicron-Sized particle clusters," *ACS Nano*, vol. 3, no. 10, pp. 3326–3334, 2009.

[229] F. Perrin, "Étude mathématique du mouvement Brownien de rotation," *Annales scientifiques de l'É.N.S. 3e série*, vol. 45, pp. 1–51, 1928.